國立臺灣大學理學院大氣科學研究所

碩士論文

Department of Atmospheric Sciences
College of Science
National Taiwan University

Master Thesis

西北太平洋大氣長河及其受熱帶氣旋之影響

Atmospheric Rivers in Western North Pacific and Influenced by Tropical Cyclones

陳映如

Ying-Ju Chen

指導教授：郭鴻基 博士

Advisor: Hung-Chi Kuo, Ph.D.

中華民國 106 年 6 月

June, 2017

doi:10.6342/NTU201701272

誌謝

「We are in the learning business!」郭鴻基老師時常這樣勉勵著我們。

謝謝郭老師鼓勵多看、多聽、多學習，給予各式研究上的建議和各種參加國內外研討會的機會，而在緊湊繁忙的研究生活中，感謝動力模擬實驗室大家給我強力的支持！首先是美雲，謝謝兩年來對於我的研究室生活中大小事務的協助和照顧、謝謝虹叡幫助我釐清和收斂研究議題、謝謝王珩在我卡關時提供寶貴的意見讓我能順利繼續研究、謝謝天耀在討論時總能讓我覺得在研究的路上很豐富有趣、謝謝徐驊一起修課一起加油打氣一起討論研究、謝謝郁涵和佩媛針對研究細節提出很好的建議，還有謝謝建彰陪我一起趕論文一起解決畢業前的各項瑣事，謝謝你們在我碩二最忙碌疲憊的最後這三個月裡，一邊忙著實驗室的觀測計畫等，還一邊幫助我、陪伴我！一路過來，還要謝謝憶婷提供很多資源和協助，謝謝立中、政友、佳瑩一起討論和分享自己的研究，謝謝你們大家，讓我最後能順利完成論文！

碩士雖然只有兩年，但充實而多元的研究生活，回憶起來彷彿過了好久好久，非常謝謝郭老師和研究室的大家！也非常感謝口試委員們：吳建銘老師、黃彥婷老師和楊明仁老師，謝謝您們對我的研究提出很多很好的建議。最後謝謝陪伴我的家人、朋友和堃豪，這段時間裡遇到不少研究困境和迷惘的我能有你們的支持，彌足珍貴。

doi:10.6342/NTU201701272

中文摘要

過去對於大氣長河的研究主要集中在大洋東側，討論大氣長河的氣候特徵、斜壓系統如何增強大氣長河，以及大氣長河登陸造成的極端降水事件；然而，西北太平洋地區亦受大氣長河影響，且正壓系統如熱帶氣旋在此區域的水氣輸送上扮演著重要角色。因此拓展大氣長河的研究範圍至西北太平洋沿岸地區，討論其氣候特徵、熱帶氣旋之影響和伴隨台灣極端降水事件的關係為本文的研究重點。

為探討 36 年大氣長河在西北太平洋之氣候特徵，此研究延續並修改前人發展之大氣長河偵測演算法，以圖形辨識分析 1980 年到 2015 年間瞬時垂直積分水氣輸送值大於 450 kg m^{-1} s^{-1}或距平值大於 250 kg m^{-1} s^{-1}之區塊，氣象變數資料取自 NASA Modern-Era Retrospective Analysis for Research and Applications Version 2 (MERRA-2) 再分析資料，颱風中心是採用 Joint Typhoon Warning Center (JTWC) 最佳路徑資料。結果顯示在西北太平洋區域，夏季（六、七、八月）的大氣長河發生頻率高於冬季（十二、一、二月），此季節變化恰與東北太平洋區域相反，且西北太平洋區域的大氣長河受颱風影響大於東北部；而熱帶氣旋與環境之交互作用有助於帶狀位渦生成，使大氣長河得以發展；若以大氣長河之發生當作判斷大雨強度以上的極端降水事件之指標，討論台灣地區此指數的預報能力，則平均而言，五六月梅雨季有高前估率 71.0%和較低的後符率 45.9%，七八月颱風季則有較高的後符率 57.3%和較低的前估率 38.0%，顯示梅雨季之極端降水事件多與大氣長河有關，而颱風季當中的大氣長河有過半數會伴隨極端降水事件發生。

關鍵字：大氣長河、極端降水、大雨、熱帶氣旋

doi:10.6342/NTU201701272

ABSTRACT

Past research on atmospheric rivers (ARs) has explored their climatological features, baroclinic mechanisms of enhancement, and the relation to continual extreme precipitation events mainly on the eastern edges of ocean basins. However, ARs also threaten the Western North Pacific (WNP) region and tropical cyclones (TCs) seem to affect the ARs' intensity. Therefore, extending the previous studies to characterize the ARs in this region, investigating how these ARs are affected by TCs, and examining the relation between extreme rainfall events and ARs are the main objectives of this paper. A modified occurrence-based detection algorithm is applied to the anomalous or total integrated water vapor transport field to identify the ARs from 1980 to 2015 in WNP, using the NASA Modern-Era Retrospective Analysis for Research and Applications Version 2 (MERRA-2) reanalysis dataset and the Joint Typhoon Warning Center (JTWC) best track data. The results emphasize that ARs occur more frequently in the warm season than in the cold season in the WNP, which is the exact opposite of the situation in the Eastern North Pacific (ENP), and that the impact of TCs is more significant in the WNP than in the ENP. Some of the insights into the influences of TCs on ARs reveal the importance of potential vorticity strips forming between TCs and ARs. Using AR occurrence as a heavy rain forecast index, the forecast skill in Taiwan is discussed briefly: during the "Mei-Yu Season" in May and June, the mean prefigurance is as high as 71.0% and the mean postagreement is relative lower than the prefigurance at a ratio of 45.9%; on the contrary, during the "Typhoon Season" in July and August, the postagreement is relatively high with 57.3% and the prefigurance is 38.0 %. This shows that most of the extreme rainfall events are associated with ARs in the "Mei-Yu Season" while over half

doi:10.6342/NTU201701272

of the ARs in the “Typhoon Season” are accompanied by extreme rainfall in Taiwan.

Keywords: atmospheric rivers, extreme rainfall, heavy rainfall, tropical cyclones

doi:10.6342/NTU201701272

CONTENTS

口試委員會審定書 ..... #

誌謝 i

中文摘要 ii

ABSTRACT iii

CONTENTS v

LIST OF FIGURES vii

Chapter 1 Introduction 1

1.1 Overview of Atmospheric Rivers (ARs) 1

1.2 Structure and Properties of ARs 2

1.3 Motivation – Influence of Tropical Cyclones (TCs) on ARs in Western North Pacific 5

Chapter 2 Data and Methods 12

2.1 Data Sources 12

2.1.1 Atmospheric Variables and the Best Track Data 12

2.1.2 El Niño-Southern Oscillation 12

2.2 Methods 13

2.2.1 Two Commonly Used Fields for AR Detection 13

2.2.2 The Modified AR-detection Algorithm 14

2.2.3 Prefigurance and Postagreement of AR and Extreme Rainfall 19

Chapter 3 Results and Discussion 26

3.1 Climatology of ARs in Western North Pacific 26

3.1.1 Seasonal Variability of ARs 26

doi:10.6342/NTU201701272

3.1.2 Interannual Variability - ENSO 28
3.1.3 ARs with TC Influence in the WNP 29
3.2 The Hypotheses of TCs' Impact on ARs in the WNP 32
3.2.1 The Case Study - Brief Introduction of TC Goni (2015 16W) 32
3.2.2 Mechanisms of the AR Formation and Maintenance 33
3.3 Heavy Rainfall and ARs in Taiwan 35
Chapter 4 Conclusions 60
REFERENCE 62
Appendix A. The Modified AR Detection Algorithm 66
Appendix B. AR Without Further TC Criteria 78
Appendix C. Details of the Boxplots 79
Appendix D. Prefigurance and Postagreement Based on anomalous IVT fields 80
Appendix E. Sensitivity Test of the Prefigurance and the Postagreement on the Smaller Domain of Taiwan 82
Appendix F. AR evolution in the Mei-Yu Season and in the Typhoon Season of Taiwan 84

doi:10.6342/NTU201701272

LIST OF FIGURES

Fig. 1.1 Total precipitable water (mm) on 26 Aug 2015 at 00 UTC. Generally, there are about four to five transient filamentary structures existing at each hemisphere. The data source is the Morphed Integrated Microwave Imagery at CIMSS (Cooperative Institute for Meteorological Satellite Studies) - Total Precipitable Water (MIMIC-TPW). 9

Fig. 1.2 A graphic of an atmospheric river (AR) interacting with the mountains with a mid-latitude cyclone over the northeast Pacific on 5 February 2015. The shaded region represents integrated water vapor (IWV). Entrance of an AR is labeled as a tropical moisture export and a warm conveyor belt (WCB) is labeled ahead of a cold front. Image credit: Adapted from NOAA/ESRL/PSD; Source: EOS Meeting Report. 9

Fig. 1.3 Conceptual representation of an atmospheric river (AR) over the northeastern Pacific Ocean summarized from the composite of satellite and aircraft dropsonde observation. (1) Plan-view schematic showing the relative positions of the polar-cold-front and the Low Level Jet (LLJ; blue solid arrow). The black hollow arrow shows the AR and the dark green shows the integrated water vapor (IWV) ≥ 2 cm. Along the AR, the associated rain-rate enhancement (RR) ≥ $0.5\ \mathrm{mm\ h^{-1}}$ is shaded in red. The blue dashed line represents a symbolic area of precipitation associated to the full system. The magenta line A–B defines a cross-section projection for (3) and the pink segments a and b over the pre-cold-frontal LLJ marked the endpoints of the region to be integrated to get profiles in (2). The light green at the bottom

doi:10.6342/NTU201701272

shows the tropical IWV reservoir ($\geq$ 3 cm). (2) Vertical schematic structure of moisture flux (left; red), moist static stability (middle; green) and wind speed (right; blue) along the LLJ [a–b in (1)]. (3) Cross section schematic through an AR [along A–B in (1)] highlighting the vertical structure of the alongfront isotachs (blue contours; $\mathrm{m\ s-1}$), water vapor specific humidity (dotted green contours; $\mathrm{g\ kg-1}$), and surface integral of horizontal alongfront moisture flux over cross-sectional area (Fh; red contours and shaded; $\times 105\ \mathrm{kg\ s-1}$). This figure is adopted from Figure 2 by Gimeno et al. (2014). 10

Fig. 1.4 A brief diagram of August 2015 AR case. The mean precipitation rate ($\mathrm{mm\ day-1}$) during 25-31 August 2015 is shaded and the 500 hPa geopotential height is contoured. The height interval is 40 m and the black bold contour shows the 5880 m contour. The track of TC Goni is marked by the cyclonic icons at 00 UTC of the date besides. The data source of the rain rate is from TRMM. The other meteorological variables are from NASA MERRA-2 reanalysis dataset. The best track data are from JTWC. 11

Fig. 2.1 The left panel is the integrated water vapor (IWV; mm; shaded) and the right panel is the integrated water vapor transport (IVT; $\mathrm{kg\ m-1\ s-1}$; shaded) at 00 UTC on 30 July 1993. The regions of high integrated water vapor are broader and less filamentary than those of high integrated water vapor transport. 21

Fig. 2.2 The 1980-2015 climatological (solid) and 2015 anomalous (dash) time series of integrated water vapor transport (IVT; $\mathrm{kg\ m-1\ s-1}$) at $(125\mathrm{oE}, 25\mathrm{oN})$. The climatology representing the seasonal cycle is the sum of the mean and first two harmonics of the 36-year time series. 21

doi:10.6342/NTU201701272

Fig. 2.3 The snapshot of the anomalous, climatological, and total integrated water vapor transport (IVT; $\mathrm{kg\ m-1\ s-1}$) at 06Z on 29 August 2015 over the north Pacific. The climatological IVT was calculated as the mean and the first two harmonics of the time series at each grid point during 1980-2015.....22

Fig. 2.4 The mean integrated water vapor transport (IVT; $\mathrm{kg\ m-1\ s-1}$) of all season in 1980-2015 near Taiwan. The top left panel shows the three domain to be averaged – the largest box ($110\mathrm{oE}, 130\mathrm{oE} \times [20\mathrm{oN}, 30\mathrm{oN}]$) surrounded by the purple line, the left inner box ($110\mathrm{oE}, 120\mathrm{oE} \times [20\mathrm{oN}, 30\mathrm{oN}]$) filled with yellow color and the right inner box ($120\mathrm{oE}, 130\mathrm{oE} \times [20\mathrm{oN}, 30\mathrm{oN}]$) filled with blue color. The top right panel shows the mean value of IVT varying with seasons in the largest domain (purple line). The bottom left panel shows the mean value of IVT in the left inner box (shaded with yellow) and the bottom right one shows the results of the right inner box (shaded with blue). 23

Fig. 2.5 An example of the results of the atmospheric river detection algorithm applying to the total integrated water vapor transport (IVT) field (top) and the anomalous IVT field (bottom) at 18 UTC on 29 August 2015. Both figures have shaded background representing the total integrated water vapor transport and the red contour circling the detected AR region. The axis of each AR is marked by the black dots which were identified by the standard image process of skeletonization. 24

Fig. 2.6 The illustration of TC-influenced (blue circle) region and the AR-influenced region (red rectangle). The center of the blue circle is at $121\mathrm{oE}, 24\mathrm{oN}$ (the cross mark) with radius of 700 km. If TC center locates within the blue circle, then the date would be classified as “OTHERS”. The red rectangle around

doi:10.6342/NTU201701272

Taiwan represents the domain $118oE, 124oE \times [20oN, 27oN]$. If the detected AR ever covers part of this rectangle, the date of AR-influenced was labeled as "AR". 25

Fig. 2.7 The illustration of the prefigurance and the postagreement. 25

Fig. 3.1 The all-season AR occurrence mean frequencies (top), and the AR frequency differences for JJA (middle), and for DJF (bottom) subtracting the all-season AR frequencies in 1980-2015. Blue (red) color refers to higher (lower) frequency than the annual mean and every positive (negative) odd value is contoured as solid (dash) line. 38

Fig. 3.2 The all-season AR occurrence mean frequencies (top), and the AR frequency differences for JJA (middle), and for DJF (bottom) subtracting the all-season AR frequencies in 1979-2014. Blue (red) color refers to higher (lower) frequency than the annual mean. Adapted from the Fig. 2. (top) and Fig. 5. (middle and bottom) of Mundhenk et al. (2016). 39

Fig. 3.3 The mean flow patterns of AR periods in May and June (a) and in July and August 2015. The streamline and the colors representing the wind speed $(\mathrm{m\ s-1})$ is at 850 hPa. The contours shows the sea-level pressure (Pa)..40

Fig. 3.4 The winter (DJF) AR frequency differences between ENSO phases and the winter AR frequencies in 1980-2015. The El Niño period is shown in the top panel and the La Niña period is in the bottom panel. Blue (red) color refers to higher (lower) frequency than the annual mean and every positive (negative) odd value is contoured as solid (dash) line. 41

Fig. 3.5 The summer (JJA) AR frequency differences between ENSO phases and the summer AR frequencies in 1980-2015. The El Niño period is shown in the top panel and the La Niña period is in the bottom panel. Blue (red) color refers

doi:10.6342/NTU201701272

to higher (lower) frequency than the annual mean and every positive (negative) odd value is contoured as solid (dash) line. 42

Fig. 3.6 Seasonal variability of displayed as the percent change of the AR frequency in the WNP ($100oE, 140oE \times [10oN, 40oN]$) compared to the 3-month seasonal mean AR frequency according to the left vertical axis. Solid lines represent El Niño (red) and La Niña (blue) conditions. The orange dash line shows the seasonality of the mean number of AR periods within the WNP according to the right vertical axis. The triangles indicate seasons in which the percent change in AR frequency for El Niño periods is statistically significant from La Niña periods at the 90% confidence level based on a t test. 43

Fig. 3.7 The mean numbers of AR periods with in the Western North Pacific and the ONI index of DJF during 1980-2015. The mean numbers of AR periods are solid lines represent the whole year mean in blue, DJF in orange, MAM in gray, JJA in yellow, and SON in dark blue corresponding to the left vertical axis. The ONI index in DJF is shown in black dash line corresponding to the right vertical axis. The WNP domain is defined by $100oE, 140oE \times 10oN, 40oN$. Since the data of MERRA-2 start from 1980, there are no December 1979 data and the first point of DJF curve is left blank. 44

Fig. 3.8 The mean location of the AR centroids in WNP. The blue lines show the mean longitude according to the left vertical axis and the orange lines show the mean latitude according to the right vertical axis. The solid lines represent the mean location of total ARs with centroids in WNP. The long dash lines represent the mean location of ARs without influences of TCs (noted as xTC) and the dot lines represent the mean location of ARs with influence of TCs

doi:10.6342/NTU201701272

(noted as TC) in WNP. 45

Fig. 3.9 The comparison of the length (left) and the median (middle) anomalous integrated water vapor (IVT) of ARs without/with TC influenced in July and August with centroids in the WNP $100oE, 140oE \times [10oN, 40oN]$. The "Without TC" group of ARs includes every AR that don't coexist with any TCs in a circle of radius 1000km centered at the AR's centroid; otherwise, ARs are classified into the group of "With TC". The values in the brackets show how much percentage of total 1639 detected ARs during July and August each group has in the WNP. The details of these boxplot is in Chapter 3.1.2. 46

Fig. 3.10 (a–c) Composite maps of filtered 850 hPa geopotential height anomalies (shaded) on day -4, day -2, and day 0 for category OC. The filter combines two low-pass filters: 3-day-weighted running average and 31-day-weighted running average. The background states of 850 hPa geopotential height (contours) are depicted. The contoured and shaded intervals are 40 m and 5 m, respectively. The location and track of the typhoons as identified by the best track data provided by the Regional Specialized Meteorological Center (RSMC) Tokyo-Typhoon Center are shown with circles. Day 0 denotes the day of maximum development of the typhoons. The right panels (d-f) are the same as the left panels but for 500 hPa geopotential height. Adapted from Fig. 3 by Hirata and Kawamura (2014). (g) is the same composite map but for filtered 925 hPa moisture flux anomalies (vectors) and their flux convergences (blue contours) on day -1. The contoured interval is $1.0 \times 10-8$ kg kg -1 s -1. Anomalies of less than $2.0 \times 10-8$ kg kg -1 s -1 have been suppressed. The reference arrow is 0.1 kg kg $-$

doi:10.6342/NTU201701272

$1\ \mathrm{m\ s-1}$. Fluxes of less than $0.01\ \mathrm{kg\ kg-1\ m\ s-1}$ have been suppressed. Superimposed is the background state of 925 hPa moisture flux convergence (shaded). The shaded interval is $2.0 \times 10-8\ \mathrm{kg\ kg-1\ s-1}$. Adapted from Fig. 6 (b) by Hirata and Kawamura (2014). 47

Fig. 3.11 (a) Composite map of filtered 850 hPa geopotential height anomalies (shaded) on day 0 for category OC in August. The filter combines two low-pass filters: 3-day-weighted running average and 31-day-weighted running average. The background state of 850 hPa geopotential height (black contours) is superimposed. The contoured and shaded intervals are 40 m and 5 m, respectively. The locations of the typhoons are depicted with circles. (b) The same as in Figure 12a but for filtered 925 hPa moisture flux anomalies (vectors) and their flux convergences (blue contours) on day -1. The contoured interval is $1.0 \times 10-8\ \mathrm{kg\ kg-1\ s-1}$. Anomalies of less than $2.0 \times 10-8\ \mathrm{kg\ kg-1\ s-1}$ have been suppressed. The reference arrow is $0.1\ \mathrm{kg\ kg-1\ m\ s-1}$. Fluxes of less than $0.01\ \mathrm{kg\ kg-1\ m\ s-1}$ have been suppressed. Superimposed is the background state of 925 hPa moisture flux convergence (shaded). The shaded interval is $2.0 \times 10-8\ \mathrm{kg\ kg-1\ s-1}$. Adapted from Fig. 12 by Hirata and Kawamura (2014).....49

Fig. 3.12 The track of TC Goni. The data source is Central Weather Bureau (CWB).50

Fig. 3.13 The geostationary infrared satellite imagery (11μm) with overlaid satellite derived low-level cloud drift winds during 23-31 August 2015. The low-level cloud-drift winds (green: 800-950 hPa, yellow: 600-799 hPa, cyan: 400-599 hPa) are created by a combination of both visible and infrared imagery, comprised of coverage by the METEOSAT-5, MTSAT-1R, and GOES-West

doi:10.6342/NTU201701272

satellites. The data source is CIMSS (Cooperative Institute for Meteorological Satellite Studies). 51

Fig. 3.14 The results of modified AR algorithm during 23-31 August 2015 and the ARs evolution. The integrated water vapor transport (kg $m-1$ $s-1$) is shaded and the features detected as ARs are contoured in red. 52

Fig. 3.15 The evolution of TC Goni and the ridge of the Pacific subtropical high during 23-25 August 2015. The subtropical high is depicted as the black contour representing the 5880 m isobaric line and other gray contours represent the isobaric lines at 500 hPa with 20 m interval. The potential vorticity (PVU; shaded) and the water vapor flux (kg $kg-1$ m $s-1$; arrow) are calculated at 320 K isentropic surface. The PV field and the water vapor flux are suppressed if the grids have water vapor flux less than 0.02 kg $kg-1$ m $s-1$. 53

Fig. 3.16 The evolution of the trough and the AR during 26-31 August 2015. The shaded regions, contours, and arrows are the same as those in Fig. 3.15. 54

Fig. 3.17 The potential vorticity on 320 K isentropic surface (contoured; PVU) calculated from ECMWF during 07-08 August1994. The interval of contour is 0.1 PVU. The strong circulation roughly depicted the location of TC Doug and the wind vectors show the region with south component of wind larger than 0.3 m $s-1$. 55

Fig. 3.18 The tracks of the 16 cases used in the composite in Fig. 3.19. 56

Fig. 3.19 The composite of 16 cases with similar TC tracks showing the AR evolution. The potential vorticity (PV; shaded) and the water vapor flux (arrow) are calculated at 320 K isentropic surface. The PV field and the water vapor flux are suppressed if the grids have water vapor flux less than 0.02 kg $kg-$

doi:10.6342/NTU201701272

1 m s − 1. The contours show the geopotential high at 500 hPa. The day 0 is defined as the maximum intensity of each TC over 20oN. 57

Fig. 3.20 The number of days that Taiwan are influenced by ARs in May and June (top) or in July and August (bottom) during 2000-2015. The definition of the four groups can be find in Chapter 2.2.3. 58

Fig. 3.21 The prefigurance and the postagreement in May and June (top) or July and August (bottom) during 2000-2015 are denoted in solid line. The mean values of them are in dash line. 59

Fig. A The code of the modified AR detection algorithm. 77

Fig. B Same as Fig. 3.1 but for removing the criteria of excluding the round TC-included features. 78

Fig. C The schematic of notched box plot. Adapted from David's Statistics website (https://sites.google.com/site/davidsstatistics/home/notched-box-plots). 79

Fig. D The number of days that Taiwan are influenced by ARs in (a) May and June or in (b) July and August during 2000-2015. The definition of the four groups can be find in Chapter 2.2.3. The prefigurance and the postagreement in (c) May and June or (d) July and August are denoted in solid line. The mean values of them are in dash line. The fields applied to the AR detection algorithm are the anomalous IVT fields. 81

Fig. E The days that Taiwan are influenced by ARs in (a) May and June or in (b) July and August during 2000-2015. The definition of the four groups is defined in Chapter 2.2.3. The prefigurance and the postagreement in (c) May and June or (d) July and August during 2000-2015 are denoted in solid line. The mean values of them are in dash line. The fields applied to the AR

doi:10.6342/NTU201701272

detection algorithm are the total IVT fields. 83

Fig. F The AR evolution (a) in the “Mei-Yu Season” during 06-21 June 2015 and (b) in the “Typhoon Season” during 17-28 July 2015. The integrated water vapor transport (kg $\mathrm{m}-1\ \mathrm{s}-1$) is shaded and the features detected as ARs (using the algorithm with anomalous IVT fields) are contoured in red. 85

doi:10.6342/NTU201701272

Chapter 1 Introduction

1.1 Overview of Atmospheric Rivers (ARs)

Moisture transfer is important for both the general circulation and the water and energy budgets of the earth's atmosphere (Peixoto and Oort 1992). In the zonally averaged perspective, the main moisture source is ocean evaporation in the subsiding region of the Hadley circulation at about 25^{o}N/S. This region are the equatorward parts of the large subtropical maritime highs and the evaporation in this region is 5 $\mathrm{mm\ day^{-1}}$ larger than precipitation (Kållberg et al. 2005). Considering the global atmospheric water vapor, the majority of it is concentrated within the tropics due to higher temperature. (Fig. 1.1).

Through observation in the mid-latitudes, it is worth noted that over 90 % of the poleward horizontal water vapor transport is constrained in four to five conveyors in each hemisphere which occupy only 10 % of the hemispheric circumference (Zhu and Newell 1998). As shown in Fig. 1.1, these transient moisture filaments (length >2000 km and width ~500 km), each of which typically transports equivalent water as the Amazon does, were first called atmospheric rivers (ARs) in the late 1990s and their spatial patterns were thought to correspond to planetary wavenumber 4-5 (Zhu and Newell 1998). In Newell et al. (1992), Ralph et al. (2004), and Neiman et al. (2008a,b), these are also called ARs. However, Bao et al. (2006) and Knippertz and Martin (2007) referred to them as "moisture conveyor belts" to highlight the similarity to the well-established conveyor belt model of extratropical cyclones.

Various names were given to these filaments depending on the location or the landfalling places. For example, at the upstream of ARs (usually in the subtropical

doi:10.6342/NTU201701272

regions), the airflows exporting moisture out of the tropics are termed as the "tropical moisture export" (TME; Knippertz and Wernli 2010; Knippertz et al. 2013); while to the downstream edge of ARs, the water vapor fluxes are often lifted along the "warm conveyor belts" (WCB) of extratropical cyclones or lie ahead of upper-level troughs (Browning 1990; Carlson 1991). A consensus was reached to unify the definition of each AR component at the International Atmospheric Rivers Workshop, and was summarized schematically in Fig. 1.2. Entrance of an AR is labeled as TME and the downstream northern part of an AR ahead of a cold front is labeled as WCB. Besides, ARs have some other local names commonly used by the forecasters, e.g., Hawaiian Fire Hose, Pineapple Express (PE), and Maya Express. Hawaiian Fire Hose and PE refer to the landfalling AR events at the western United States originating from the Hawaiian Islands, and Maya Express extends from Mexico or Yucatan Peninsula (Lackmann and Gyakum 1999; Dirmeyer et al. 2009).

1.2 Structure and Properties of ARs

Structural analysis of ARs have gained great attention among not only scientists but also operational forecasters and policy makers, since ARs often play an important role in extreme precipitation events, flooding and water supply in California, Arizona and the Western European (Guan et al. 2010; Dettinger et al. 2011; Ralph et al. 2006; Rivera et al. 2014; Cavazos and Rivas 2004; Ramos et al. 2015; Ramos et al. 2016; Lavers and Villarini 2013). The mechanisms of AR formation and maintenance were therefore of great concern (Lackmann and Gyakum 1999; Ralph et al. 2004; Ralph et al. 2005; Gimeno et al. 2014; Payne and Magnusdottir 2014, among others).

As early as 1999, Lackmann and Gyakum (1999) revealed the linkage between the

doi:10.6342/NTU201701272

cold-season PE hitting the western United States and the subtropical moisture bursts [termed *moisture bursts* by McGuirk et al. (1987)]. Through analyzing both slowly varying planetary-scale and relatively fast moving synoptic-scale (or cyclone-scale) composite flow patterns of 42 PE events and a case study in mid-January 1986, they confirmed the contribution of the mobile extratropical cyclone to moisture transport are predominant and planetary-scale flow may help maintain the lasting storm tracks.

Later, several studies proposed the detailed mechanism of AR formation (Gimeno et al. 2014; Ralph et al. 2004; Ralph et al. 2005) and the influence of large-scale flow (Payne and Magnusdottir 2014) on ARs for the cold-season ARs in the mid-latitudes. A brief mini-review of previous works was done by Gimeno et al. (2014). They documented the conceptual models of ARs structure with extratropical cyclones or frontal waves from the aspects of observation, modeling and the features of landfalling ARs. Summarization of ARs' composite structure over the Eastern North Pacific (ENP) is shown in Fig. 1.3, which is adapted from Fig. 2 by Gimeno et al. (2014) yet was first proposed by Ralph et al. (2004) and Ralph et al. (2005). This conceptual model scheme based on the composite of satellite and aircraft dropsonde data portrays an AR developing along a polar-cold front. This AR is accompanied with the Low Level Jet (LLJ) (Fig. 1.3 (1)) with 75% of moisture flux confined below 2.5 km and the maximum wind speed locating at about 1 km (Fig. 1.3 (2)). Besides, it has strong low-level horizontal alongfront moisture flux (F_h; shaded in Fig. 1.3 (3)), which is defined as $F_h = (\rho U q) \times \Delta z \times \Delta L$, where ρ: layer-mean values of air density, U: layer-mean values of alongfront wind speed, q: layer-mean values of water vapor specific humidity within each vertical increment (Δz), and ΔL: the mean horizontal spacing between dropsonde data in Ralph et al. (2004). Considering the large-scale flow influencing ARs prior to the landfalling over the west coast of North America, Payne and Magnusdottir (2014) noted that the location of jet, Rossby wave propagation,

doi:10.6342/NTU201701272

and the Rossby wave breaking in the upper troposphere are important. In their AR trajectories analyses, ARs lie approximately south of the storm track consistent with their relation with WCB. Among the strongest ARs in their study, ARs have initial locations primarily in the Western North Pacific (WNP) and are associated with a sustained upper-level jet, while the weakest ARs located more eastward at the beginning with a weaker jet. Payne and Magnusdottir (2014) also illustrated that El Niño–Southern Oscillation (ENSO) might modulate these landfalling ARs over through affecting the position of the jet and the location of the Rossby wave breaking region. During El Niño periods, the landfalling latitudes as well as the upper-level jets shift equatorward (Payne and Magnusdottir 2014).

Recently, Mundhenk et al. (2016) found that ARs are not only cold-season phenomena but also occur in warm-season by employing their occurrence-based AR detection algorithm to the all-season instantaneous anomalous vertically integrated water vapor transport fields over the North Pacific. A thorough AR climatology, including the influence of ENSO and the Madden-Julian Oscillation (MJO), over the basin is provided in their work and a displacement of ARs' location from the southeast in cold season to the northwest in warm season over the North Pacific basin is shown. This seasonal shift of AR incidence in the Western North Pacific is thought of as a contribution of the prevailing mei-yu or East Asian monsoon in warm season. Ascribed to these two same contributions, Knippertz and Wernli (2010) found that the amount of summertime tropical moisture export (TME) across $35^{o}\mathrm{N}$ has a maximum of 4835×10^{12} g day^{-1} over $120^{o}-130^{o}\mathrm{E}$ (East China Sea). This means that the summer TME in East China Sea alone, which contributes only less than 3% of the earth's circumstance, is responsible for 15% of the global TME across $35^{o}\mathrm{N}$ in summer.

doi:10.6342/NTU201701272

1.3 Motivation – Influence of Tropical Cyclones (TCs) on ARs in Western North Pacific

In addition to the mei-yu front and the East Asian monsoon mentioned in Mundhenk et al. (2016) and Knippertz and Wernli (2010), tropical cyclones (TCs) in the Western North Pacific might also affect water vapor transport through different mechanisms. Since ARs are composed of strong water vapor transport belts, these mechanisms are thus potential influential factors for ARs. In the previous studies (Archambault et al. 2013; Cordeira et al. 2013; Bosart et al. 2017; Payne and Magnusdottir 2014; Yoshida and Itoh 2012; Hirata and Kawamura 2014), the influences of TCs on water vapor transport can vary depending on their location and interaction with the environment. These studies gave some hints about how TCs may influence ARs.

First, Archambault et al. (2013) found that during August-November, TCs are more likely to recurve and the recurving TCs have stronger association with the Rossby wave amplification and dispersion over the mid-latitude North Pacific. Generally, this strengthened flow persists for about four days (Archambault et al. 2013). Also, as Cordeira et al. (2013) portrayed, the AR hit the western coast of the United States in late October 2010 was composed of multiple conveyor branches in proximity to the recurving WNP TCs. In their study, two ARs developing close to TCs later merged to be one AR along the anticyclonic shear side of an intensifying North Pacific jet stream in the central North Pacific. For another example, Bosart et al. (2017) found that four extreme weather events (EWEs) happened in conjunction with the enhanced Rossby wave train in late October 2007 over the North America. One of these EWEs was the heavy rainfall in the central Mississippi Valley, which was supported by a persistent corridor established by an elongated, slow-moving potential vorticity streamer associated with the wave

doi:10.6342/NTU201701272

amplification (Bosart et al. 2017). In addition, during the extended winter (November-March), Payne and Magnusdottir (2014) found that the amplified extratropical flow pattern is likely to enhance ARs and often contributes to the onset of high-impact weather events far downstream over North America. Before TC recurvature in the higher latitudes, TCs close to the western flank of the western Pacific subtropical high could enhance the poleward moisture transport through the negative planetary vorticity advection which increases the pressure gradient and the wind speed between the subtropical high and TCs (Yoshida and Itoh 2012; Hirata and Kawamura 2014).

While several previous studies (Archambault et al. 2013; Cordeira et al. 2013; Bosart et al. 2017; Yoshida and Itoh 2012; Hirata and Kawamura 2014) highlight the strengthening mechanisms of water vapor transport by TCs and the associated EWEs in the Pacific region, the scope of the research is limited in fall and winter in the ENP (Cordeira et al. 2013; Archambault et al. 2013; Bosart et al. 2017) or in summer in the mid-latitudes of the WNP (Hirata and Kawamura 2014). However, the strong water vapor transport or ARs and the related extreme rainfall events could also bring damage to the sub-latitude of the WNP over East Asia. For example, in the last 7 days of August 2015, the continual occurrences of extreme rainfall events in Taiwan were accompanied with an AR staying almost stationary above Taiwan; moreover, this AR was seem to formed along the track of TC Goni turned north (details are discussed in Chapter 3.2). A brief diagram in Fig. 1.4 shows the track of TC Goni during 17-26 August 2015, the mean precipitation rate, and the mean 500 hPa geopotential height over 25-31 August 2015. Since this AR stayed almost stationary, the mean states shown in Fig. 1.4 could basically represent the temporal AR during the period. The damage due to this event, though, was mild compared to the flood and mudslide caused by the landing of typhoons, yet the tremendous precipitation sustained by ARs formed after the track of a TC could be hazardous since it

doi:10.6342/NTU201701272

was easier to be neglected.

During this AR event, the concomitant extreme rainfall over the whole Taiwan was still astonishing. For instance, on 25 August 2015, the rain rate got higher than 90 mm h^{-1} at Shuilin Township in Yunlin County (雲林縣水林鄉). On 26 August, Jiangjun District in Tainan City (台南市將軍區) received a shower with the rain rate up to 63.5 mm h^{-1}. In the following five days, the highest hourly rain rate records of all stations in Taiwan of each day were not less than 30 mm h^{-1} and up to four of these days got the rain rate roughly equal to or higher than 50 mm h^{-1}. This continual heavy rain caused flooding over several places, such as Tucheng District (土城區), Xindian District (新店區) in New Taipei City (新北市), which also suffered from the heavy rain with rain intensity over 50 mm h^{-1}.

This case aroused our curiosity of how TCs induce or enhance ARs and to what extent TCs amplify ARs in the sub-latitude Western North Pacific. From the previous studies (Cordeira et al. 2013; 李 1997; Yoshida and Itoh 2012; Hirata and Kawamura 2014), the circulation of a TC and the interaction between a TC and a subtropical high are recognized as key components to increase and sustain the water vapor transport. Further, since a wind component is necessary for water vapor to be transported, there should be potential vorticity strips along the filamentary ARs due to their wind speed gradient to the surrounding. Compared with those potential vorticity streamers protruding downward from high level in Bosart et al. (2017), the potential vorticity strips of our concern are at the low level where ARs have maximum transport of water vapor. In addition, as demonstrated in 李 (1997), TCs might reorganize the weak PV regions nearby and enhance the southwesterly winds through these resultant PV strips.

Before further investigation of the interaction between TCs and ARs in the sub-

doi:10.6342/NTU201701272

latitude Western North Pacific, the preliminary understanding of the definition and properties of ARs in this region is necessary. Therefore, we referred to Mundhenk et al. (2016), who first developed and applied an objective AR detection algorithm suitable for the whole North Pacific region. In our study, we modified the algorithm extending to the coastal region of East Asia to get a brief perception of the climatology characteristics in this region. The data and methodologies are presented in Chapter 2. The climatology and variability of the detected ARs, the impact of TCs on ARs in the WNP, and the relation between ARs and extreme rainfall events in Taiwan are shown in Chapter 3. The conclusions are summarized in Chapter 4.

doi:10.6342/NTU201701272

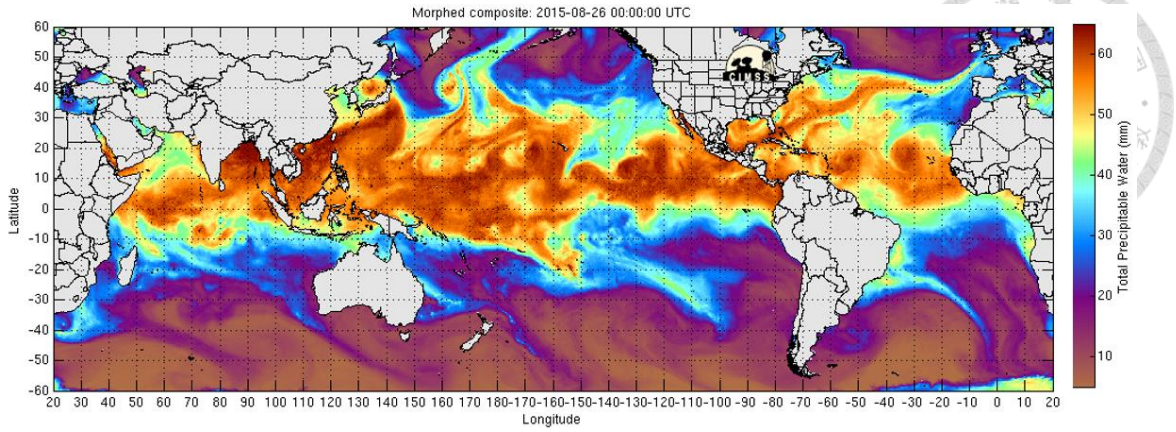

Fig. 1.1 Total precipitable water (mm) on 26 Aug 2015 at 00 UTC. Generally, there are about four to five transient filamentary structures existing at each hemisphere. The data source is the Morphed Integrated Microwave Imagery at CIMSS (Cooperative Institute for Meteorological Satellite Studies) - Total Precipitable Water (MIMIC-TPW).

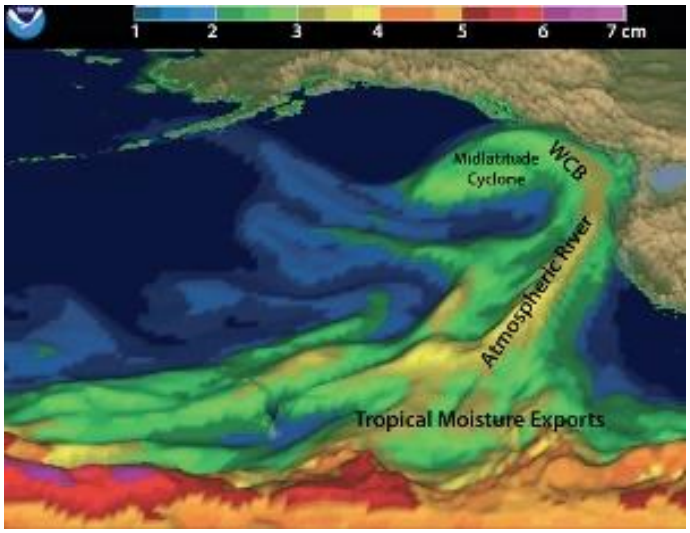

Fig. 1.2 A graphic of an atmospheric river (AR) interacting with the mountains with a mid-latitude cyclone over the northeast Pacific on 5 February 2015. The shaded region represents integrated water vapor (IWV). Entrance of an AR is labeled as a tropical moisture export and a warm conveyor belt (WCB) is labeled ahead of a cold front. Image credit: Adapted from NOAA/ESRL/PSD; Source: EOS Meeting Report.

doi:10.6342/NTU201701272

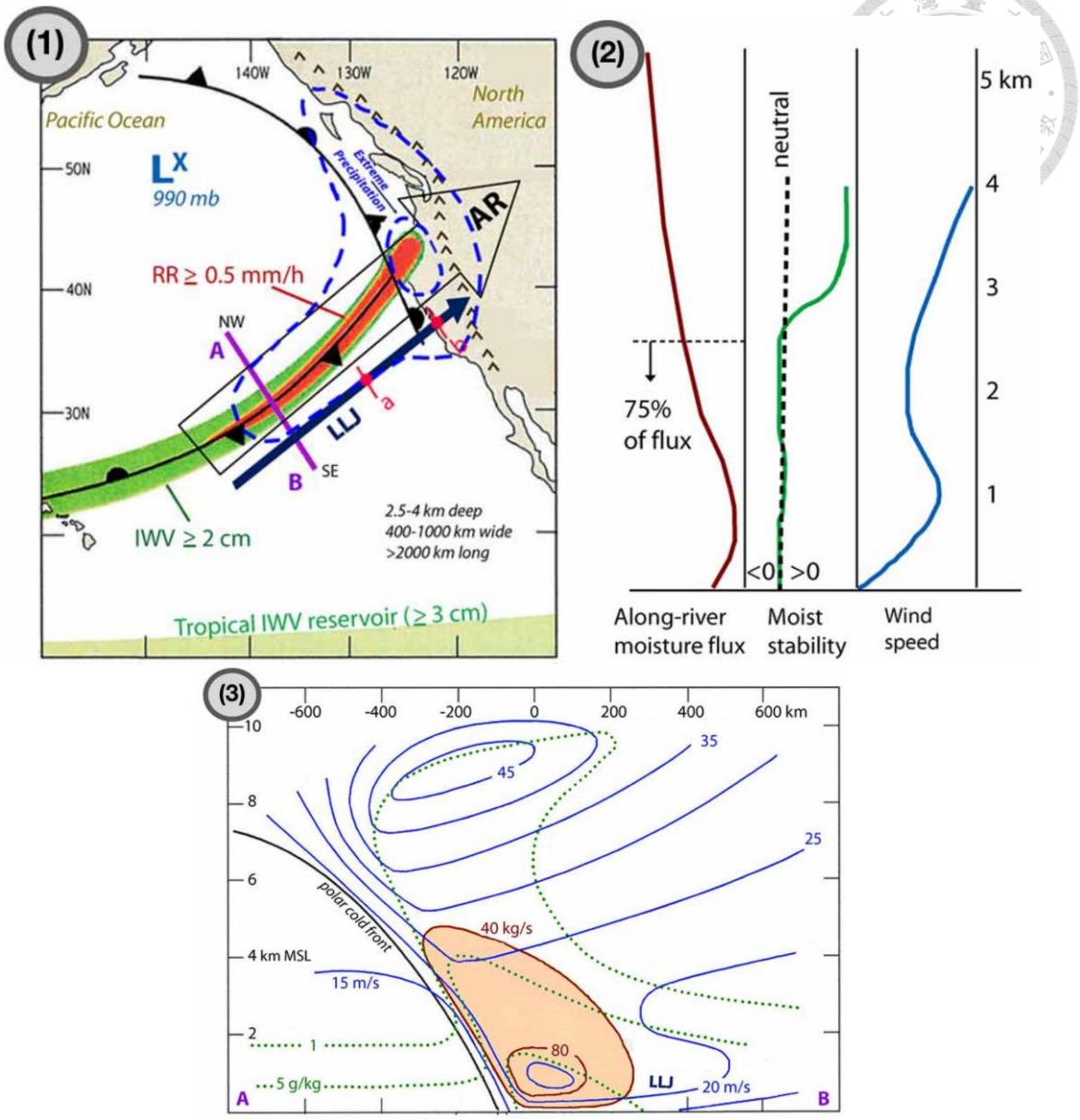

Fig. 1.3 Conceptual representation of an atmospheric river (AR) over the northeastern Pacific Ocean summarized from the composite of satellite and aircraft dropsonde observation. (1) Plan-view schematic showing the relative positions of the polar-cold-front and the Low Level Jet (LLJ; blue solid arrow). The black hollow arrow shows the AR and the dark green shows the integrated water vapor (IWV) ≥ 2 cm. Along the AR, the associated rain-rate enhancement (RR) ≥ 0.5 mm h^{-1} is shaded in red. The blue dashed line represents a symbolic area of precipitation associated to the full system. The magenta line A–B defines a cross-section projection for (3) and the pink segments a and

doi:10.6342/NTU201701272

b over the pre-cold-frontal LLJ marked the endpoints of the region to be integrated to get profiles in (2). The light green at the bottom shows the tropical IWV reservoir ($\geq$ 3 cm). (2) Vertical schematic structure of moisture flux (left; red), moist static stability (middle; green) and wind speed (right; blue) along the LLJ [a–b in (1)]. (3) Cross section schematic through an AR [along A–B in (1)] highlighting the vertical structure of the alongfront isotachs (blue contours; m s^{-1}), water vapor specific humidity (dotted green contours; g kg^{-1}), and surface integral of horizontal alongfront moisture flux over cross-sectional area (F_h; red contours and shaded; $\times 10^5$ kg s^{-1}). This figure is adopted from Figure 2 by Gimeno et al. (2014).

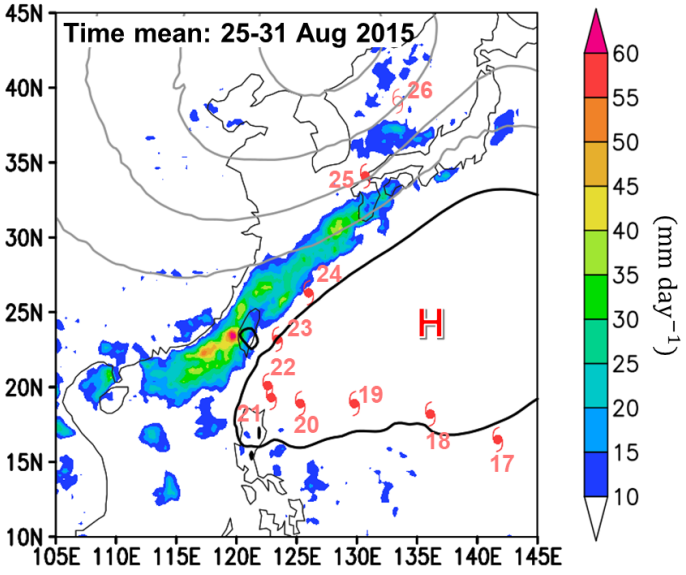

Fig. 1.4 A brief diagram of August 2015 AR case. The mean precipitation rate (mm day^{-1}) during 25-31 August 2015 is shaded and the 500 hPa geopotential height is contoured. The height interval is 40 m and the black bold contour shows the 5880 m contour. The track of TC Goni is marked by the cyclonic icons at 00 UTC of the date besides. The data source of the rain rate is from TRMM. The other meteorological variables are from NASA MERRA-2 reanalysis dataset. The best track data are from JTWC.

doi:10.6342/NTU201701272

Chapter 2 Data and Methods

2.1 Data Sources

2.1.1 Atmospheric Variables and the Best Track Data

The data of meteorological variables, such as zonal wind, meridional wind, specific humanity, geopotential height and pressure are from the NASA Modern-Era Retrospective Analysis for Research and Applications Version 2 (MERRA-2) reanalysis dataset. MERRA-2 has better assimilation system and higher resolution than the first version – MERRA, which already has refined representation of the atmosphere's hydrological cycle (Rienecker et al. 2011). The 36 years (1980-2015) instantaneous fields of horizontal winds and specific humanity are retrieved at native spatial resolution ($1/2^{o}$ latitude $\times 5/8^{o}$ longitude) and 6-h temporal resolution on isobaric surfaces. The best track data of the Western North Pacific Ocean from the Joint Typhoon Warning Center (JTWC) were used to define the center of TC in Western North Pacific. These two kinds of data were used in the AR detection algorithm. In addition, the hourly rainfall data over Taiwan in 2000-2015 were from the records of 28 manual observation stations and 172 automatic observation stations of the Central Weather Bureau (CWB). These stations were chosen for their continuous observation in this 16-year long period. These rainfall data were used for comparing the relation between ARs and the heavy rainfall events in Taiwan and the best track data of JTWC were also involved for excluding the days in which TCs were close to Taiwan.

2.1.2 El Niño-Southern Oscillation

The Oceanic Niño Index (ONI), the official ENSO indicator of the National Oceanic and Atmospheric Administration's (NOAA), was used to measure the El Niño-Southern

doi:10.6342/NTU201701272

Oscillation (ENSO). The ONI index is based on a 3 month running mean of Extended Reconstructed Sea Surface Temperature Version 4 (ERSST.v4; Huang et al. 2015) SST anomalies in the Niño 3.4 region ($[120^{o}\mathrm{W}, 170^{o}\mathrm{W}] \times [5^{o}\mathrm{S}, 5^{o}\mathrm{N}]$)], based on centered 30-year base periods updated every 5 years. The warm or El Niño (cold or La Niña) episodes are defined when the threshold of $+0.5^{o}\mathrm{C}$ ($-0.5^{o}\mathrm{C}$) for the Oceanic Niño Index (ONI) is met for at least 5 consecutive over-lapping seasons. For the frequency comparison between El Niño and La Niña, the composite maps of the two conditions were made. For summer, there are 9 El Niño years (1982, 1987, 1991, 1992, 1997, 2002, 2004, 2009, and 2015) and 5 years La Niña (1988, 1998, 1999, 2000, and 2010). For winter, 12 El Niño years (1980, 1983, 1987, 1988, 1992, 1995, 1998, 2003, 2005, 2007, 2010, and 2015) composed of the composite and 9 years (1985, 1989, 1996, 1999, 2000, 2001, 2008, 2011, and 2012) are responsible for the winter La Niña composite.

2.2 Methods

2.2.1 Two Commonly Used Fields for AR Detection

There are two kinds of spatial fields commonly used to detect ARs: total precipitable water (or integrated water vapor, IWV) and integrated water vapor transport (IVT). Zhu and Newell (1998) first noticed these filaments and called them ARs through calculating the IVT larger than the mean flux plus 0.3 times of the difference of the maximum and minimum flux at the same latitude by using the grid point data from the European Centre for Medium-Range Weather Forecasts (ECMWF). Latter, Ralph et al. (2004) verified IWV as a proxy of ARs. In a case study during California Land-falling Jets Experiment (CALJET) in 1997/98, they examined this proxy through both the satellite-derived IWV from Special Sensor Microwave Imager (SSM/I) sensor and the airborne observations.

doi:10.6342/NTU201701272

This proxy simplified the recognition of ARs since in situ low-level wind data over ocean were rare. Both of IWV and IVT were commonly used in AR studies, and other criteria on the appearance (e.g., length ≥ 2000 km and width ≤ 1000 km) and strength (e.g., IWV ≥ 20 mm, IVT ≥ 250 kg m^{-1} s^{-1}) of ARs were selected depending on different research purposes. Some other typical criteria of AR detection were summarized in Supplementary Table II of Gimeno et al. (2014).

Among these two fields, IVT was chosen for its clear and dynamical features. Since the water vapor is usually abundant in Western North Pacific, the IWV regions in this region are usually broader and disordered (e.g., Fig. 2.1). Besides the reason for clarity, in aid of the dynamically consistent reanalysis data, using IVT could represent the moisture transport and gave the perspective on analyzing the structure of ARs. Therefore, with more filamentary features and with wind component, the IVT field become a better choice for the following application for the standard image processing to detect ARs. Here, we followed the method of Zhu and Newell (1998), Lavers et al. (2012) and Mundhenk et al. (2016) to calculate IVT integrating from 1000 hPa to 300 hPa:

$$\text{IVT} = \int_{1000\text{hPa}}^{300\text{hPa}} \left(q|\vec{\boldsymbol{V}}|\right) \frac{dp}{g} ,$$

where q is layer-averaged specific humidity in kg kg^{-1}, $|\vec{\boldsymbol{V}}|$ is magnitude of the layer-averaged horizontal wind vector in m s^{-1}, g is gravitational acceleration, and dp is the pressure difference between adjacent pressure levels. The value of IVT is not sensitive to the upper bound of the integration, since most of the water vapor remains in the low altitude.

2.2.2 The Modified AR-detection Algorithm

To investigate the relation between the heavy rain and AR in Taiwan and to bridge and extend the AR study to the Western North Pacific, two kinds of IVT fields were used

doi:10.6342/NTU201701272

in this study. One is total IVT and another is anomalous IVT which means to remove the climatology from the total IVT.

First, using total IVT to process the standard image processing techniques was for the examination of relevance between AR and the heavy rain in Taiwan. Normally, ARs are thousands of kilometers long and serve as suitable environments for the convection to develop. However, the occurrences of extreme rainfall not only consist of a suitable environment but also other forcing mechanisms. Given the focus on the potential relation between ARs and the heavy rainfall, the strict criteria on IVT fields were not necessary and the total IVT fields with a looser threshold than the anomalous IVT fields were used. The problem of using the anomalous IVT fields was that it often missed the features carrying abundant moisture which could probably provide favorable environments for convection yet were not strong enough to be identify as ARs. Further discussion was compiled in Section 3.

Second, regarding those specific filaments carrying more water vapor than usual, the climatological IVT was removed. In addition, this process helped clarify the image and gave a more filamentary features of anomalous IVT. The mean and first two harmonics of the IVT time series at each grid point data representing the mean seasonal cycle were eliminated through fast Fourier transform. For example, Fig. 2.2 shows the 1980-2015 climatological and 2015 instantaneous time series of IVT at $(125^{o}\mathrm{E}, 25^{o}\mathrm{N})$, and Fig. 2.3 shows a snapshot of the anomalous, climatological, and the total IVT. This removed the more persistent features, such as the tropical moisture reservoir, and improved the AR-like image detection.

The AR-detection algorithm based on occurrence developed by Mundhenk et al. (2016) was composed of several criteria on intensity and geometry. (Their algorithm was written in the Python 2.7 programming language and is available online at

doi:10.6342/NTU201701272

http://hdl.handle.net/10217/170619.) They combined the works of Lavers and Villarini (2013), Wick et al. (2013), Payne and Magnusdottir (2014), and Nayak et al (2014) to developed the objective detection approaches. Lavers and Villarini (2013) set different IVT thresholds corresponding to the latitudinal bands and asked for duration over 18 hours to count an event. Wick et al. (2013) introduced the standard image processing techniques including thresholding and skeletonization to characterize the satellite-observed or model derived IWV signatures to identify ARs. Payne and Magnusdottir (2014) selected landfalling ARs through percentile-based analysis using Modern-Era Retrospective Analysis for Research and Applications (MERRA) reanalysis data. Then, temporal persistence was not required as shown in Nayak et al. (2014), while focusing on the occurrences. Consequently, in Mundhenk et al. (2016), the MERRA dataset (grid size: $1/2^{o}$ latitude $\times 2/3^{o}$ longitude) were used to get the anomalous IVT fields, which represented similar results from the percentile-based methods, and the thresholds were set on both the magnitude and the appearance through standard image processing techniques. In this paper, the MERRA-2 reanalysis data with higher resolution—$1/2^{o}$ latitude $\times 5/8^{o}$ longitude—were used. Every AR hit per time step (i.e., per 6 hour) was recorded when the following criteria were met:

[1] The least number of continuous grids of total IVT (anomalous IVT) greater than 450 (250) kg m^{-1} s^{-1} were 150 grids.

[2] The characteristics of retaining blobs from [1] were determined using standard image processing techniques.

[3] The length of the major axis of the feature needed to be larger than 35 grid points (approximately 2000 km, but variable corresponding to the position in the domain) and ratio of major to minor axis length should be larger than 1.6. This excluded the less plumelike features.

doi:10.6342/NTU201701272

[4] Weak features with minimum mean anomalous IVT less than $305\ \mathrm{kg\ m^{-1}\ s^{-1}}$ (For total IVT, there is no restriction on the mean IVT of the features.) and/or those whose centroids (determined by the weighted anomalous IVT values) equatorward of $20^{o}\mathrm{N}$ lying almost parallel to the latitude lines with less than 0.95 radians were removed. Also, those with centroids equatorward of $5^{o}\mathrm{N}$ were eliminated. These blobs were thought to be weak or more related to the west-east-oriented broad lower-frequency moisture swells along ITCZ respectively and were thus removed.

[5] Further test on the filamentary features were processed by requiring the eccentricity of a representative ellipse with the same second moments greater than about 0.87. (Eccentricity is a parameter greater equal to 0 and less than 1. When eccentricity equals to 0, the curve is a circle.)

[6] Blobs equatorward of $25^{o}\mathrm{N}$ with eccentricity larger than 0.87 and had mean anomalous IVT lager than $375\ \mathrm{kg\ m^{-1}\ s^{-1}}$ (For total IVT, there is no restriction on the mean IVT of the features.) extending over 50% of the area of the bounding box were removed. These might be tropical cyclones or similar storms.

[7] Features with centroids equatorward of $20^{o}\mathrm{N}$ and with holes smaller than 5 pixels were mostly eyes of tropical cyclones and were excluded.

[8] To further remove the stormlike features, those with aspect ratio larger than 1.9 and with solidity (the proportion of the pixels in the convex hull that were also in the region, that is $\mathrm{Area/ConvexArea}$) greater than 0.9 extending over 40% of the area of the bounding box were abandoned.

[9] This step was added in this paper to ensure the removal of the TC-dominated plumes, since several features apparently dominated by TCs only were still

doi:10.6342/NTU201701272

not been identified in the above steps. As a result, the TC centers were introduced from the JTWC best track data to eliminate the features extending over 40% of the area of the bounding box and containing at least one tropical cyclone center.

[10] The following steps after [1]-[8] were designed to clarify the retaining features, if multiple peaks of total IVT (anomalous IVT) were detected. First, if a segment of a retaining feature whose centroid was equatorward of $27.5^{o}\mathrm{N}$ has a hole, the segment was then eliminated from the original retaining feature. This kind of segments were mostly TCs inside the long moisture conveyors.

[11] For those segments with eccentricity less than 0.86, the segmental portion were also removed from the features, since they were not filament-like enough.

[12] Weak connection between two anomalous IVT peaks was removed if the mean intensity of anomalous IVT of the segment was weaker than $305\ \mathrm{kg\ m^{-1}\ s^{-1}}$. (For total IVT, there is no restriction on the mean IVT of the features and thereby skipping this process.)

[13] While the segments have centroids were equatorward of $12.5^{o}\mathrm{N}$, their orientation are estimated. Those whose orientation off the parallels of less than 0.95 radians were excluded.

[14] The centroids of the features locate equatorward of $20^{o}\mathrm{N}$ with any peak segment orients in parallel to latitudinal line with in 10 degrees were partially taken off.

It was to obtain longer (roughly over 2000 km) and less TC-dominated features that the occurrence-based AR image recognition detection algorithm developed by Mundhenk et al. (2016) was modified. The threshold of total IVT at step [1] was according to the value of IVT which was one standard deviation higher than the mean IVT near Taiwan in

doi:10.6342/NTU201701272

the warm season (Fig. 2.4). Also, another filtering condition that features with extent rate (area of the feature over the area of the bounding box) over 40% and contained at least one TC center was set. These features were found to be misidentified when TCs were marginally distorted by the terrain yet were still composed of the strong circulation around TCs. The differences between the results based on total IVT field (top panel) and anomalous IVT field (bottom panel) are shown in Fig. 2.5. The red contour circles the detected AR and the total IVT are shaded in both panel regardless which field is applied to the algorithm. Two examined fields – total IVT and anomalous IVT – gave results with different length and width. As can be expected, processing the anomalous IVT fields gave features with shorter and narrower appearances. Sometimes, features that were not identified as ARs in the anomalous IVT fields were detected as ARs with the total IVT fields. The code of this modified AR algorithm is provided in Appendix A.

2.2.3 Prefigurance and Postagreement of AR and Extreme Rainfall

As was shown by the case happening in the last August 2015, the intermittent extreme rain continuously showering for more than a week was accompanied with an AR wandering over Taiwan simultaneously. Hence, this gave us an incentive to investigate the relation between the AR and extreme rainfall over Taiwan. The prefigurance and the postagreement were introduced from the forecasting points of view to examine the forecasting ability of AR to extreme rainfall. Since only the extreme rainfall which might related to ARs was of concern, those rainy days corresponding to the TC were unwanted and classified as "OTHERS". The removal of these dates were done by eliminating the dates when any TC centers located in the circle with radius of 700 km centered at $(121^{o}\mathrm{E}, 24^{o}\mathrm{N})$ (Fig. 2.6). To simply the analysis, the definition of the extreme rainfall refers partially to the threshold of the heavy rain by CWB. Then, the hourly rainfall data from 200 surface observation stations with continuous observation over 2000-2015 were

doi:10.6342/NTU201701272

used to define the date of "HEAVY RAIN" if there were any hourly rainfall records larger than $40\ \mathrm{mm\ h^{-1}}$ among any of these stations at any hour of the day. The date influenced by the "AR" was defined as the date in which the box of Taiwan ($[118^{o}\mathrm{E}, 124^{o}\mathrm{E}] \times [20^{o}\mathrm{N}, 27^{o}\mathrm{N}]$, shown in Fig. 2.6), was partially cover by the contour of the detected AR. When both the conditions of the "HEAVY RAIN" and "AR" were met, the date was defined as "HIT" since "AR" here was thought as a forecasting factor.

On the one hand, the prefigurance means the accurate forecasting ratio of the total observational events. The postagreement, on the other hand, means the ratio of accuracy over the total forecasting events (Fig. 2.7). In this part of analysis, an "AR" event was seen as a forecast and a "HEAVY RAIN" event was seen as an observation result to be forecast. Hence, the prefigurance was defined as the number of the "HIT" days over the number of the "HEAVY RAIN" days and the postagreement was defined as the number of the "HIT" days over the "AR" days. To get a quick concept of the prefigurance and the postagreement, the necessary condition and sufficient condition were introduced to draw an analogy. However, note that the definition of the "HEAVY RAIN" is not strict, so it is not proper to call the prefigurance/postagreement as the necessary/sufficient condition. If the prefigurance in this case is close to 100%, then "AR" is likely to be the necessary condition for the heavy rainfall events. On the contrary, if the postagreement is close to 100%, "AR" could be analogized as the sufficient condition of the heavy rainfall events; however, if the postagreement is low, this means that using AR as a forecasting factor would lead to too much false alarm.

doi:10.6342/NTU201701272

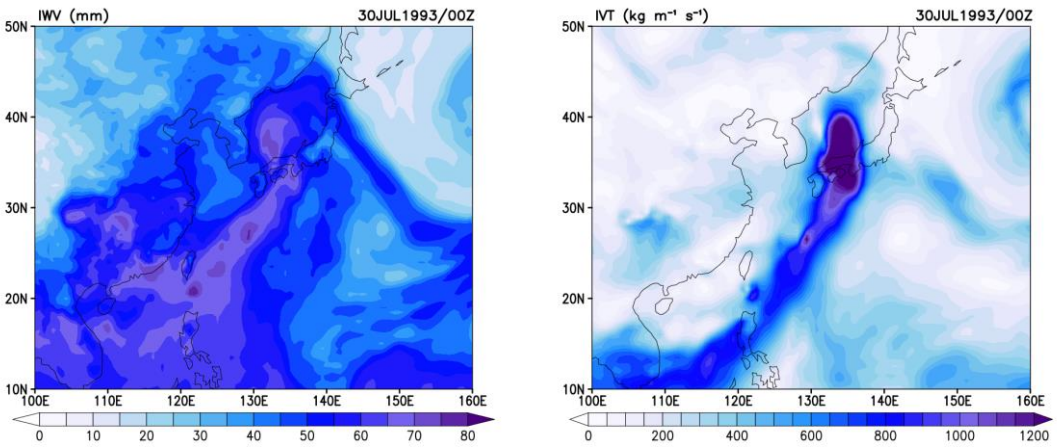

Fig. 2.1 The left panel is the integrated water vapor (IWV; mm; shaded) and the right panel is the integrated water vapor transport (IVT; kg m^{-1} s^{-1}; shaded) at 00 UTC on 30 July 1993. The regions of high integrated water vapor are broader and less filamentary than those of high integrated water vapor transport.

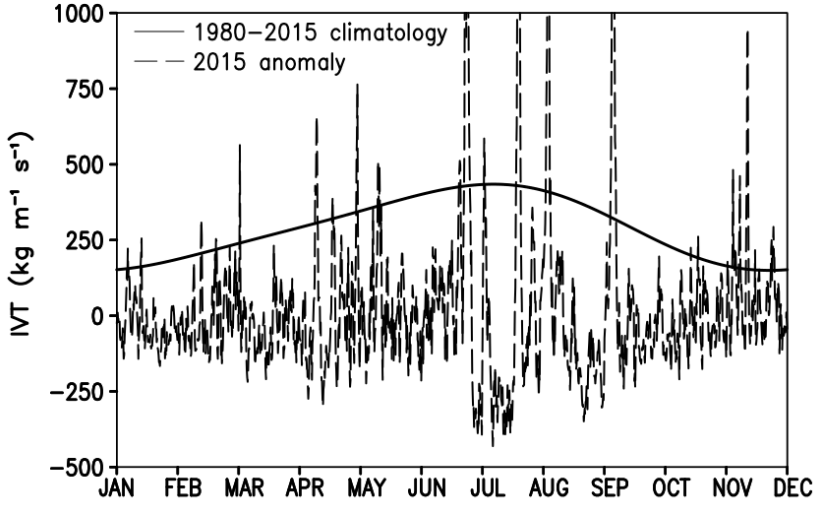

Fig. 2.2 The 1980-2015 climatological (solid) and 2015 anomalous (dash) time series of integrated water vapor transport (IVT; kg m^{-1} s^{-1}) at $(125^{o}E, 25^{o}N)$. The climatology representing the seasonal cycle is the sum of the mean and first two harmonics of the 36-year time series.

doi:10.6342/NTU201701272

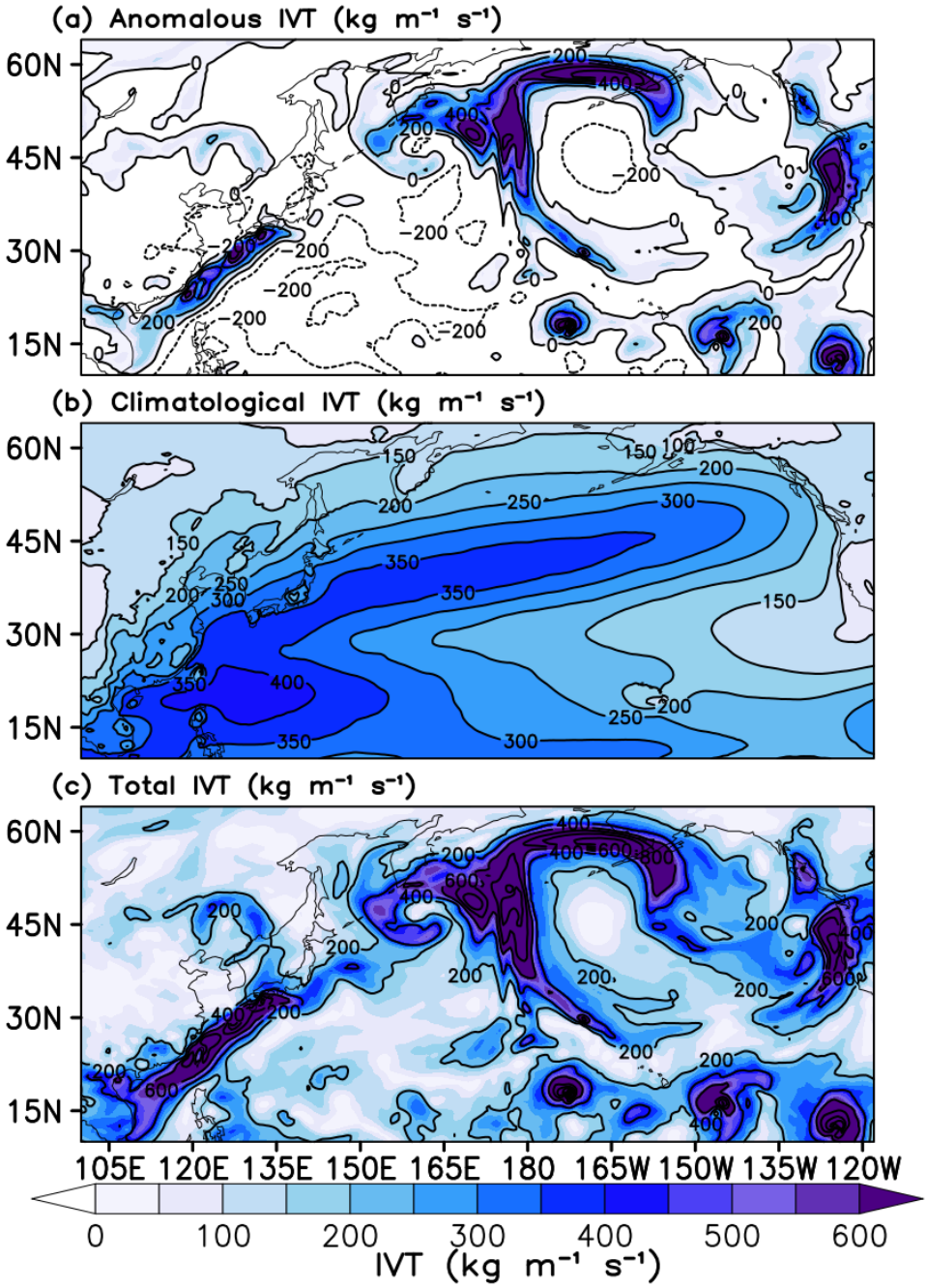

Fig. 2.3 The snapshot of the anomalous, climatological, and total integrated water vapor transport (IVT; kg m^{-1} s^{-1}) at 06Z on 29 August 2015 over the north Pacific. The climatological IVT was calculated as the mean and the first two harmonics of the time series at each grid point during 1980-2015.

doi:10.6342/NTU201701272

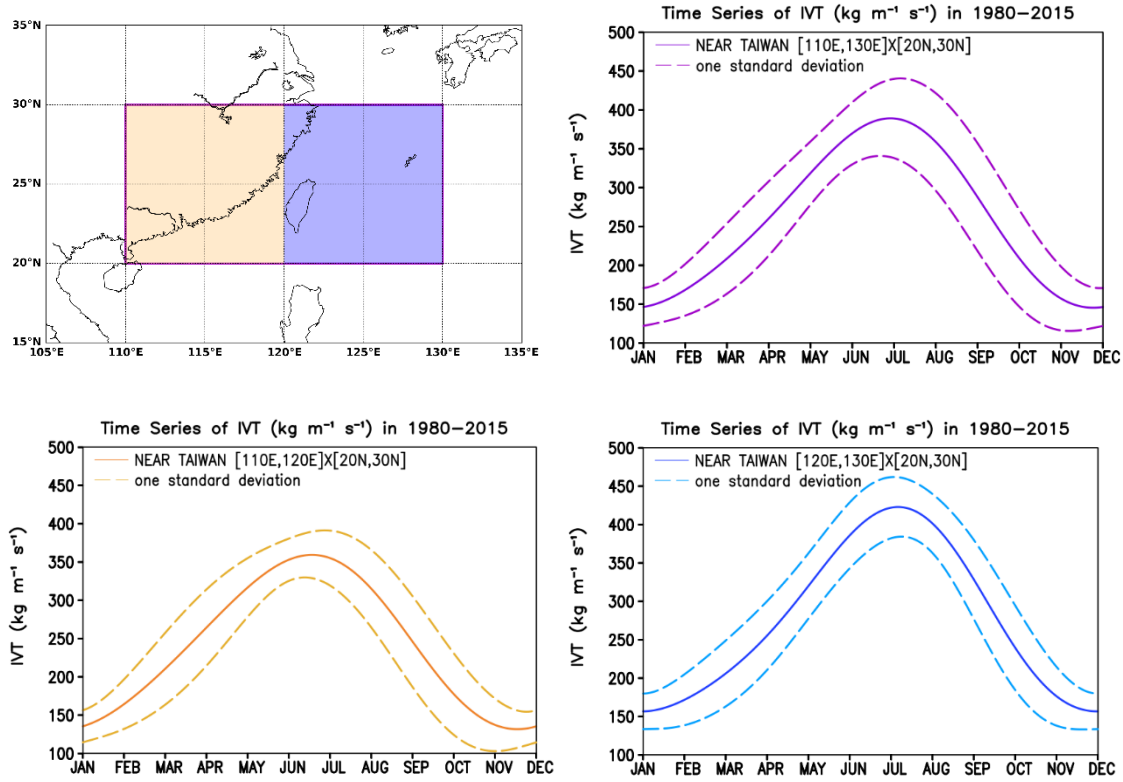

Fig. 2.4 The mean integrated water vapor transport (IVT; kg m^{-1} s^{-1}) of all season in 1980-2015 near Taiwan. The top left panel shows the three domain to be averaged – the largest box ($[110^oE, 130^oE] \times [20^oN, 30^oN]$) surrounded by the purple line, the left inner box ($[110^oE, 120^oE] \times [20^oN, 30^oN]$) filled with yellow color and the right inner box ($[120^oE, 130^oE] \times [20^oN, 30^oN]$) filled with blue color. The top right panel shows the mean value of IVT varying with seasons in the largest domain (purple line). The bottom left panel shows the mean value of IVT in the left inner box (shaded with yellow) and the bottom right one shows the results of the right inner box (shaded with blue).

doi:10.6342/NTU201701272

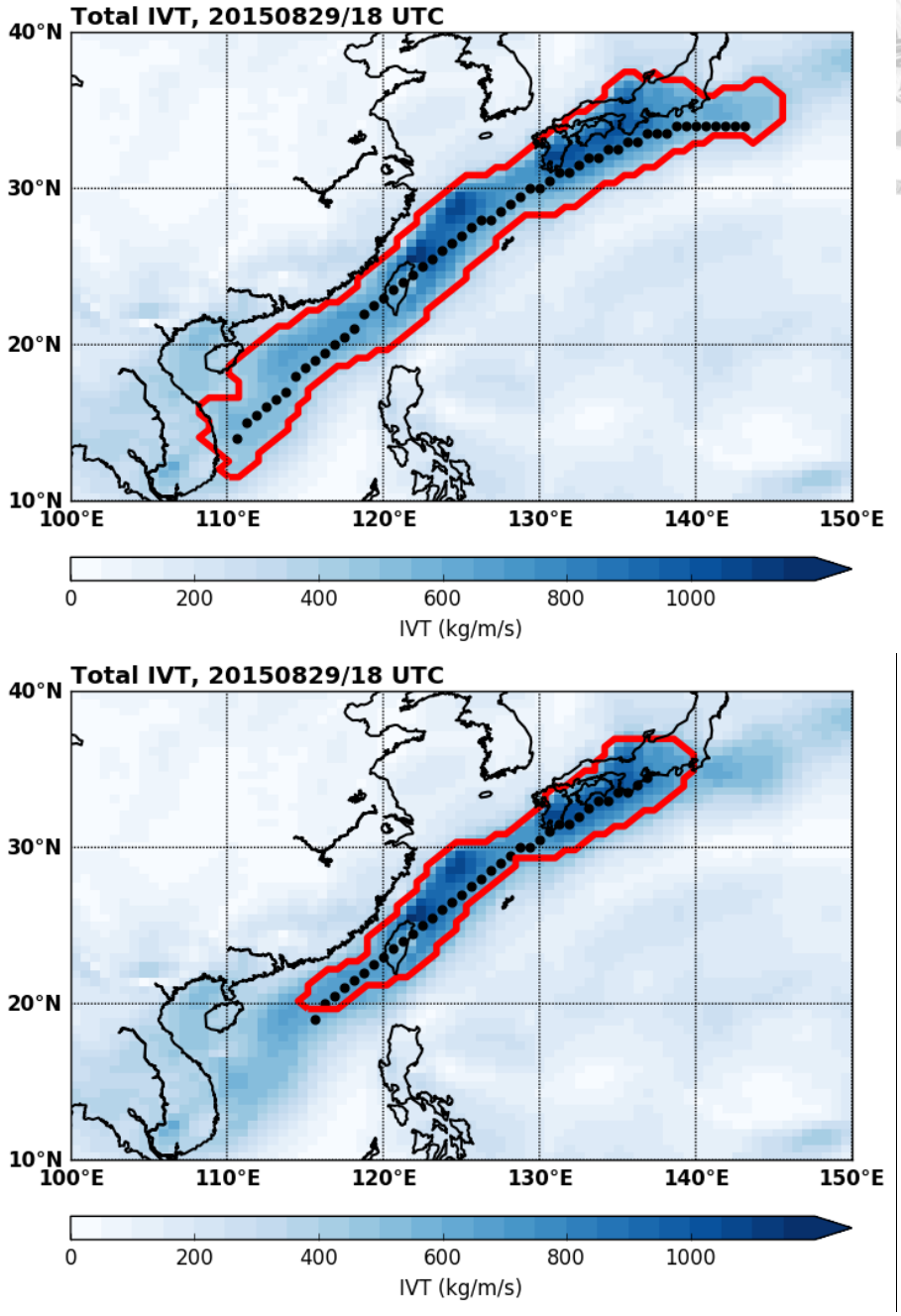

Fig. 2.5 An example of the results of the atmospheric river detection algorithm applying to the total integrated water vapor transport (IVT) field (top) and the anomalous IVT field (bottom) at 18 UTC on 29 August 2015. Both figures have shaded background representing the total integrated water vapor transport and the red contour circling the detected AR region. The axis of each AR is marked by the black dots which were identified by the standard image process of skeletonization.

doi:10.6342/NTU201701272

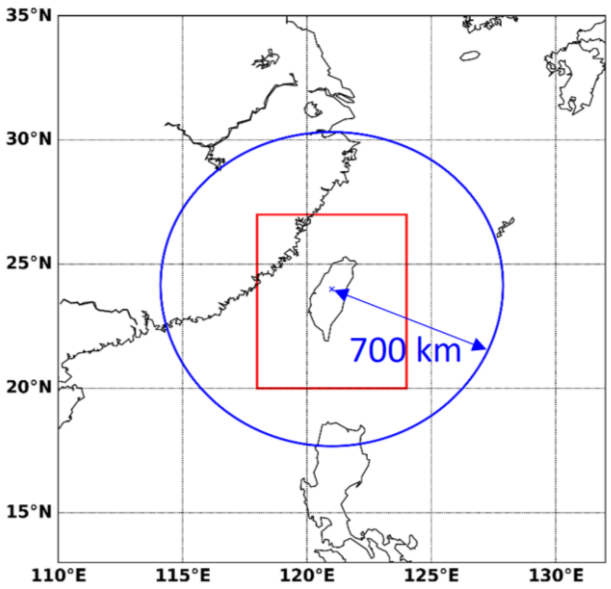

Fig. 2.6 The illustration of TC-influenced (blue circle) region and the AR-influenced region (red rectangle). The center of the blue circle is at $(121^{o}\mathrm{E}, 24^{o}\mathrm{N})$ (the cross mark) with radius of 700 km. If TC center locates within the blue circle, then the date would be classified as "OTHERS". The red rectangle around Taiwan represents the domain $[118^{o}\mathrm{E}, 124^{o}\mathrm{E}] \times [20^{o}\mathrm{N}, 27^{o}\mathrm{N}]$. If the detected AR ever covers part of this rectangle, the date of AR-influenced was labeled as "AR".

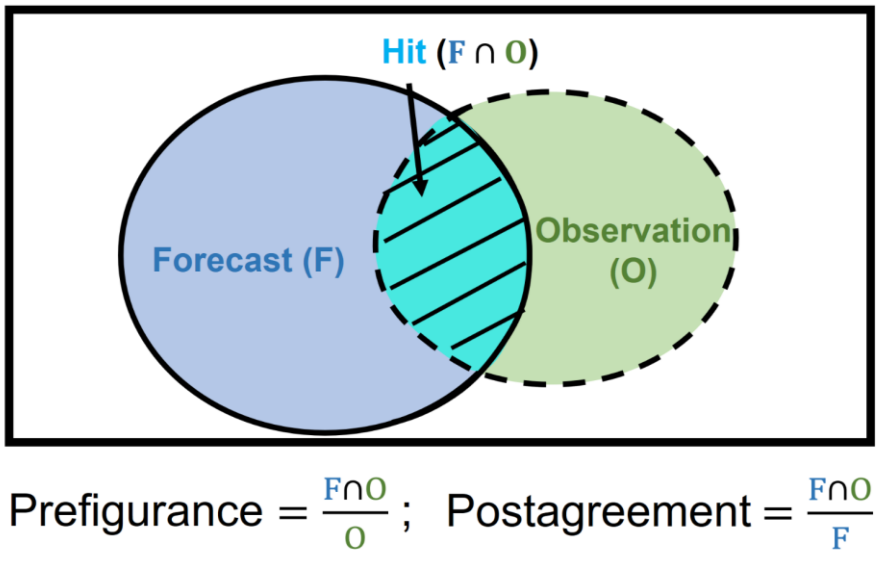

Fig. 2.7 The illustration of the prefigurance and the postagreement.

doi:10.6342/NTU201701272

Chapter 3 Results and Discussion

The discussion was divided into three parts: the climatology of ARs in the WNP, hypothesis of TCs on ARs in the WNP, and the relation between AR and the heavy rainfall over Taiwan. Notice that when the climatology of AR was discussed, the results were achieved from the AR detection algorithm applying to the anomalous IVT fields. The anomalous IVT fields were used since the results often represent stronger conveyors and are more filamentary than other features. Also, this kind of fields was used in Mundhenk et al. (2016) and therefore become convenient and easy for comparing the results with their research. While focusing on the relation between AR and the heavy rain, total IVT was preferable. (The results of using anomalous IVT fields is shown in Appendix D.)

3.1 Climatology of ARs in Western North Pacific

3.1.1 Seasonal Variability of ARs

With the modified AR detection algorithm applying to the anomalous IVT fields, the results in Fig. 3.1 show an all-season climatology of AR frequency and the differences between the mean frequency of JJA or DJA and the all-season. These results are consistent with those in Mundhenk et al. (2016) shown in Fig. 3.2, yet give further information of AR frequency along the coastal region and the sub-latitude region of Asia .

Similar to Mundhenk et al. (2016) in Fig. 3.2, the all-season mean frequency (top panel of Fig. 3.1) has the maximum frequency over 12% located in the central basin and the frequency over the Northeast Asia is comparable to that along the northern California and the west coast of Canada. The annual mean AR frequency gradient poleward of the Tropic of Cancer was found to be tied to the Rossby wave dynamics

doi:10.6342/NTU201701272

and the northern extension of the Hadley circulation (Mundhenk et al. 2016). Averaging speaking, ARs occur more frequently over the East Asia in the warm season and the maximum anomalous frequency is at the East China Sea with roughly 6% higher than the annual mean, which means that about 12% of the days (~11 days) in JJA over this Sea are influenced by ARs. This anomalous high frequency over the East Asia in summer (middle panel of Fig. 3.1 and Fig. 3.2) was thought to be connected with the prevailing mei-yu fronts and the East Asian summer monsoon (Mundhenk et al. 2016; Knippertz and Wernli 2013) while the anomalous low AR frequency in winter indicates the absence of these two systems (bottom panel of Fig. 3.1 and Fig. 3.2). In addition, as Wang et al. (2013) stated, "the western Pacific Subtropical High (WPSH) is a prime circulation system affecting East Asian summer monsoon (EASM) and western North Pacific TS activities …" In Fig. 3.3, the mean flow patterns of AR periods in May and June (Fig. 3.3 (a)) and in July and August (Fig. 3.3 (b)) are shown. The seasonal shift of the ARs' location is consistent with the seasonal shift of the subtropical high. This consistence is probably an indication of the importance of subtropical high to ARs.

Though the spatial patterns of AR frequency are almost the same between the results of the modified algorithm and those in Mundhenk et al (2016), some apparent differences exist in the Western North Pacific. The all-season frequency drops 1-2% (top panel of Fig. 3.1 and Fig. 3.2), and the same decline can be observed in the seasonal frequency differences (middle and bottom panel of Fig. 3.1 and Fig. 3.2). However, these differences are subtle (Fig. 3.2 and Fig. 3.3), if there are no criterion on excluding round TC-included features (Fig. A.3). Thus, to further investigate the interaction between TCs and more AR-like conveyors, it is thought necessary to remove the misidentified TC-dominated features to give more clear results in Western North Pacific. Besides, by extending the domain, the outputs of the modified algorithm show

doi:10.6342/NTU201701272

that the distribution of AR frequency extends to the sub-latitude region of the East Asia and the frequency at $120^{o}\mathrm{E}$ is 1-4% higher than that at $120^{o}\mathrm{W}$ in the low-latitude between $15^{o}\mathrm{N} - 30^{o}\mathrm{N}$. Furthermore, consider the incidence of AR in boreal summer (middle panel of Fig. 3.1), the AR frequency near Taiwan is 2-3% more than the annual mean. This climatological result is consistent with our experiences of often seeing an elongated water vapor conveyor in satellite images over Taiwan when we try to figure out what causes summertime heavy rainfall and what environment is suitable for summertime strong convection to develop. Some relevant discussion between ARs and heavy rainfall in Taiwan is in Chapter 3.3. Although the values of the frequency change as the threshold of anomalous IVT ≥ 250 kg m^{-1} s^{-1} changes, the spatial patterns are robust and leave us a concept of the AR climatology.

3.1.2 Interannual Variability - ENSO

The frequency anomalies between two ENSO phases are shown in Fig. 3.4 for winter and Fig. 3.5 for summer. Compared to the regular winter and summer, the most significant differences are in the central and eastern North Pacific and minor differences in the WNP.

In winter, more ARs occur close to the western coast of the United States than usual during the El Niño period. The maximum frequency difference shifts to the central Pacific during La Niña period. While in the WNP, the frequency differences during both the El Niño period and the La Niña period are fine.

In summer, two maximum AR frequency differences occur in the central Pacific and near Japan at the latitude about $38^{o}\mathrm{N}$ during the El Niño period. The maximum in the central Pacific is about 5^{o} southern and is 3% higher than the difference between total summer and the all-season mean. Another maximum near Japan is about 1% higher than the difference between total summer and the all-season mean but at the same position. During La Niña period, the maximum in the central Pacific extends zonally and extends

doi:10.6342/NTU201701272

southwestward to Japan and the coastal region of the East Asia.

Regarding the WNP region in $[100^{o}\mathrm{E}, 140^{o}\mathrm{E}] \times [10^{o}\mathrm{N}, 40^{o}\mathrm{N}]$, the seasonal variability displayed as percent change of AR frequency compared to the 3-month seasonal mean is shown in Fig. 3.6. The higher AR frequency previously mentioned in La Niña warm season in this region can also be seen in Fig. 3.6. Besides, in the late summer to the early fall, more ARs tend to occur during La Niña periods than during the El Niño period. However, it turns to the opposite in the late fall and in the spring that ARs occur more frequently during the El Niño period. The higher frequency in the spring during El Niño periods may relate to the persistent anomalous lower-tropospheric anticyclone over the Philippine Sea after the peak El Niño discussed in Wang et al. (2000). This anomalous anticyclone may persist until June and probably benefit the water vapor transport and ARs in the WNP. The lag response of the flow pattern in WNP to the peak ENSO events, which are usually in winter, also seem to exist in the number of ARs. In Fig. 3.7, for example, 7 peaks of AR numbers in the spring and summer of 1983, 1987, 1995, 1998, 2003, 2010, and 2015 seem to have a close relation with the ONI index of the previous winter. The ARs in WNP might be influenced by complex air-sea-land interaction and other tropical (e.g., MJO) and extratropical variability, and the remote impact of ENSO on ARs in the WNP might be one of the influential factors.

3.1.3 ARs with TC Influence in the WNP

As was shown in the previous studies (Cordeira et al. 2013; Archambault et al. 2013; Bosart et al. 2017; Hirata and Kawamura 2014), TCs could enhance water vapor transport in many different ways. However, these amplified transport which probably compose ARs received less attention in the low-latitude East Asia. Since these ARs had higher potential to cause damage in Taiwan and other costal Asian places, we narrowed down the domain of interest to $[100^{o}\mathrm{E}, 140^{o}\mathrm{E}] \times [10^{o}\mathrm{N}, 40^{o}\mathrm{N}]$, hereafter refers to Western North Pacific

doi:10.6342/NTU201701272

(WNP). To find a representative center or core of an AR feature, anomalous IVT was analogized to mass and a centroid of the anomalous IVT of the feature was defined as the center of the AR. Although most of the AR centroids located inside the ARs and were close to the strongest IVT part of ARs, some ARs with non-convex shapes had centroids outside themselves. However, since these centroids were only used to filter the ARs with centroids outside WPN and to classify ARs depending on their distance between the centers of TCs, the locations of the centroids inside ARs or not were not very important.

In Fig. 3.8 and Fig. 3.9, ARs in July and August with centroids in WNP were divided into two groups: “with TC” group and “Without TC” group. If the distance between the TC center and the centroid of the AR was less than 1000 km, the AR was classified in the group of “With TC”; otherwise, if the distance was longer equal to 1000 km or no TCs exist simultaneously, the AR was classified into the group of “Without TC”. As a consequence, there were 1639 ARs with centroids in WPN and 13.5% of them were grouped in “With TC”. The comparison of these two groups is shown in Fig. 3.8 and Fig. 3.9 in three aspects: the mean longitude and latitude of ARs, length of ARs and the median anomalous IVT of ARs. The median anomalous IVT was chosen to represent the strength of each AR feature because the value is less sensitive to the extreme values and was not dominant by the TC circulation. On average, ARs shift westward and equatorward with the influences of TCs (Fig. 3.8). Only the cases during May and November are discussed and other months are neglected because of few typhoons. In the left panel of Fig. 3.9, it is shown that the mean length of “With TC” ARs is about 1.2 times (600 km) longer than the “Without TC” ARs. Also, the mean of the median anomalous IVT of ARs in the “With TC” group is around 440 $\mathrm{kg\ m^{-1}s^{-1}}$, which is about 1.1 times larger than that in “Without TC” group. The details of Fig. 3.9 are documented in Appendix C. Note that due to the removal of those round TC-included features in the algorithm, the median

doi:10.6342/NTU201701272

values of the anomalous IVT of ARs are less likely attributed to the strong IVT in eyewalls of TCs but are more likely enhanced by TCs nearby through other mechanisms.

These mechanisms included, for example, the mechanism proposed by Yoshida and Itoh (2012) and Hirata and Kawamura (2014) that a TC could induce an anomalous anticyclonic circulation to its east by negative potential vorticity advection and could enhance the western ridge of the North Pacific subtropical high. They thought that the enhanced pressure gradient between the TC and the subtropical high could increase the poleward moist advection. In Hirata and Kawamura (2014), a TC is classified as the Okinawa Island course (OC) if it passes through the 30°N line between 120°E and 130°E. With their composite results in July (Fig. 3.10), the positive height anomalies in both the 850 hPa and the 500 hPa become conspicuous along the west periphery of the North Pacific subtropical high as the TCs reach their maximum intensity, denoted as “day 0”. In addition, they found that the negative height anomalies to the west of TCs also become pronounced perhaps due to the dispersive westward phase propagation of Rossby waves, and the similar patterns were also exhibit in the composite maps in August. The associated moisture fluxes and the moisture fluxes convergence at the low level (925 hPa) are shown in Fig. 3.10 (g) for July and Fig. 3.11 (b) for August. Though the argument of Hirata and Kawamura (2014) is that the distribution of the fluxes convergence would determine the patterns and strength of rainfall events over Japan, we focus on the significant enhanced moisture fluxes between the TCs and the subtropical high and those to south of the TCs which were also observed in the late August 2015 AR case. This case was also associated with an TC of OC group by the definition in Hirata and Kawamura (2014). The details of the case and a composite of the 16 AR cases associated with similar TC tracks are presented in the following sub-chapter to discuss the hypotheses of TCs’ impact on ARs.

doi:10.6342/NTU201701272

3.2 The Hypotheses of TCs' Impact on ARs in the WNP

As mentioned in Chapter 1, during the period that AR stayed almost stationary over Taiwan in the late August 2015, plenty of extreme rainfall events occurred almost everywhere in Taiwan and brought a lot of damage. Besides, this AR seemed to form along TC Goni, which moved from the east of Taiwan on 23 August 2015 to the Sea of Japan on 26 August 2015. Therefore, some mechanism from the previous studies were organized to state the hypotheses of TC's impact on the ARs in the WNP. These hypotheses include the mechanism of the interaction between TCs and the subtropical high proposed by Hirata and Kawamura (2014) and the mechanism proposed by 李 (1997) that TCs may help organize the PV strips to sustain the water vapor transport. First, the case study in the late August 2015 was provided to discuss the mechanism. Then, a composite result of the 16 cases with similar TC tracks was shown.

3.2.1 The Case Study - Brief Introduction of TC Goni (2015 16W)

TC Goni (16W) formed on 13 August 2015 and later moved along the southern edge of the Pacific subtropical high to the north of Luzon Island on 21 August (Fig. 3.12). After remaining almost stationary for two days, Goni turned north and moved to the northeast of Taiwan with a clear eye on late 23 August (Fig. 3.13(a)). At this time, Goni reached its maximum intensity with the lowest pressure of 937 hPa. Then, Goni moved northeast and crossed Kyushu region of Japan around 12 UTC on 25 August; meanwhile, it transitioned into an extratropical cyclone and dissipated at 00 UTC on 26 August with the minimum pressure of 985 hPa. Although Goni weakened all the way from the east of Taiwan to the Sea of Japan, the clouds following developed more intensively over these region during this period (Fig. 3.13).

doi:10.6342/NTU201701272

3.2.2 Mechanisms of the AR Formation and Maintenance

Different from the prevalent hypotheses that ARs are resulted from extratropical cyclones and frontal wave in the mid-latitudes, this case shows that a TC may be an important factor for low-latitude ARs to form.

From the cloud bands in Fig. 3.13 and the IVT fields (shaded) in Fig. 3.14, this AR started to form on late 25 August after TC Goni reached the Sea of Japan and stayed stationary over Taiwan until 31 August. However, since our modified algorithm applying to the anomalous IVT was designed for identifying filamentary features that convey extraordinary moisture, this AR was not detected until 18 UTC on 28 August 2015 and remained its strength by 18 UTC on 30 August (red contour in Fig. 3.14).

To investigate the mechanisms for this AR formation and maintenance, we examined the interaction between TC Goni and the environment from the "PV thinking" perspective. The potential vorticity (PV) on the isentropic surface was introduced due to its close relation to the wind gradient between the AR and the surrounding and its conservative property.

Regarding the potential factors of the AR formation, the corresponding development of the low level flow patterns is essential since most of the water vapor transport of the AR is confined in the low level. As expected, the overlapped positive PV fields (shaded) on the 320 K (~ 850 hPa) isentropic surface demonstrate a tie relation with the moisture flux that high PV regions lie at the cyclonic shear side of the strong moisture fluxes (Fig. 3.15 and Fig. 3.16). According to Hirata and Kawamura (2014), the interaction between TCs and the North Pacific subtropical high can enhance the moisture transport between each other by negative PV advection to the west of the TC. In the AR case of August 2015, the westward extension of the western flank of the subtropical high and the stronger moisture fluxes (vectors) between Goni and the subtropical high was indeed getting clear

doi:10.6342/NTU201701272

during 23 August and 24 August (Fig. 3.15). In addition, as demonstrated in 李 (1997), a TC might be able to reorganize and elongate the weak PV region to the west of it and increase southwesterly winds through the consequent elongated PV strips (Fig. 3.17). Due to the conservative property, the corresponding geopotential heights, winds, and temperature fields can be retrieved by PV inversion, provided that the balance relation and the boundary conditions are suitably given (Davis and Emanuel 1991). Through the piecewise potential vorticity inversion (PPVI) on the reanalysis data of European Centre for Medium-Range Weather Forecasts (ECMWF), 李 (1997) found that the partitioned PV region of Doug dominated PV fluxes and moisture fluxes at 700 hPa. Further, 李 (1997) conducted an experiment in the idealized shallow water model. Since a one-layer shallow water is physically identical to a layer between two isentropic surfaces, the idealized experiment can somewhat simulate the real case. After implanting a vortex representing Doug and a pool of weak PV, the stretching feature along the circulation of Doug was clear and the PV strip form.

The maintenance of the AR and the PV strip can be contributed to the sustainable southwesterly wind along the western ridge of subtropical high in front of the upper level trough. After 25 August, the subtropical high extended further westward making the preferable position of AR locate above Taiwan (Fig. 3.16). Meanwhile, the upper level trough (dash contour) which was likely deepen by the cold advection Goni in an extratropical transition stage also extended close to Taiwan and provided the suitable southerly wind for AR to sustain (Fig. 3.16).

Since different tracks of TCs have different interaction with the western ridge of the Pacific subtropical high (Hirata and Kawamura 2014), only 16 TCs were chosen to make a composite. The simple way to find these 16 cases is to filter other TC cases which don’t

doi:10.6342/NTU201701272

pass both the north region $[122^{o}\mathrm{E}, 130^{o}\mathrm{E}] \times [29^{o}\mathrm{N}, 31^{o}\mathrm{N}]$ and the south region $[122^{o}\mathrm{E}, 130^{o}\mathrm{E}] \times [21^{o}\mathrm{N}, 23^{o}\mathrm{N}]$. Then, those cases close to or influenced by other TCs besides were eliminated subjectively. The 16 cases remained have very similar tracks (Fig. 3.18) as the August 2015 case and have accompanied with an AR during their lifetime or in 3 days after the TC dissipated.

The composite result (Fig. 3.19) shows a rather clear PV strip along the strong water vapor transport region than the 2015 case. Day 0 denotes the maximum intensity of each TC over $20^{o}\mathrm{N}$. However, the amplification of the trough was not that clear as the 2015 case. This is probably because of the different upper level conditions between 16 cases. This further confirm the argument that the TC may be the major factor to help the AR form at the low latitude while the trough was probably the minor factor or the factor of maintenance.

3.3 Heavy Rainfall and ARs in Taiwan

From the statistics provided in the previous sections, we found that ARs are more frequently in summertime and they might cause damage to Taiwan, if passing through Taiwan. However, as is shown in Fig. 3.14, the intensive total IVT regions are long filamentary with an averaging magnitude over 450 $\mathrm{kg\ m^{-1}\ s^{-1}}$ from 25 August to 30 August although they were only detected between late 28 August to 30 August. In addition, the extreme rainfall events had already happened on 25 August and continually occurred in the following 7 days in various places in Taiwan. Thus, the modified algorithm applying to the anomalous IVT fields with threshold of $250\ \mathrm{kg\ m^{-1}\ s^{-1}}$ was thought unsuitable if the forecast ability were of our concern. Hence, to examine the potential cause-effect relation between extreme rainfall and ARs in Taiwan, a

doi:10.6342/NTU201701272

concession was made to moderate the criterion to include the intensive IVT features with total IVT larger at each grid points larger than $450\ \mathrm{kg\ m^{-1}\ s^{-1}}$. Also, the definition of the extreme rainfall partially referred to the threshold of the heavy rainfall defined by CWB and thus the term - heavy rainfall is used hereafter.

The prefigurance and the postagreement defined in Chapter 2.2.3 are introduced to examine the forecasting ability of AR occurrence to heavy rainfall occurrence. In the "Mei-Yu Season" defined as May and June by the Central Weather Bureau, Taiwan is covered by ARs roughly over 30 days and nearly half of them are coincidence with the heavy rainfall events (Fig. 3.20, top panel). On the other hand, the heavy rainfall events in "Mei-Yu Season" are almost associated with ARs over Taiwan (Fig. 3.20, top panel). These ratios can be more specified as the prefigurance and the postagreement. The mean prefigurance is over 70 % and it got over 90% in some of the years like 2003, 2010, and 2015 (Fig. 3.21, top panel). The postagreement in the "Mei-Yu Season" is relative low with a mean about 46%; however, it can be larger than 50%, such as in 2001 and 2012, and is not lower than 30% over the 16 years (Fig. 3.21, top panel).

On the contrary, the days that AR covered Taiwan in July and August are about one-third of those in the "Mei-Yu Season" (Fig. 3.20). These two months are classified into the "Typhoon Season" of Taiwan due to the frequently invasion of TCs. Contradictory to the high ratio in the "Mei-Yu Season," the prefigurance is lower than the postagreement in this "Typhoon Season." The mean prefigurance drops over 30% and the postagreement increases about 10% from the "Mei-Yu Season" to the following two months. The sensitivity of the prefigurance and postagreement on the domain size of Taiwan is briefly tested by reducing the size and the result is shown in Appendix E.

With high prefigurance in the "Mei-Yu Season," it shows that most of the heavy rainfall events are accompanied with ARs covering Taiwan; however, the lower

doi:10.6342/NTU201701272

postagreement indicates that when there is an AR over Taiwan, it is possible that no heavy rainfall events would happen. Therefore, using AR occurrences as forecaster tools would lead to high false alarm ratio in the “Mei-Yu Season.” In contrast, the prefigurance is low in the “Typhoon Season” and this means that plenty of heavy rainfall events are without ARs. The high postagreement shows that when there are an AR over Taiwan, there is a high potential to witness a heavy rainfall event. Two AR cases were chosen as examples to show the AR evolution during the “Mei-Yu Season” and the “Typhoon Season” of Taiwan (Appendix F).

doi:10.6342/NTU201701272

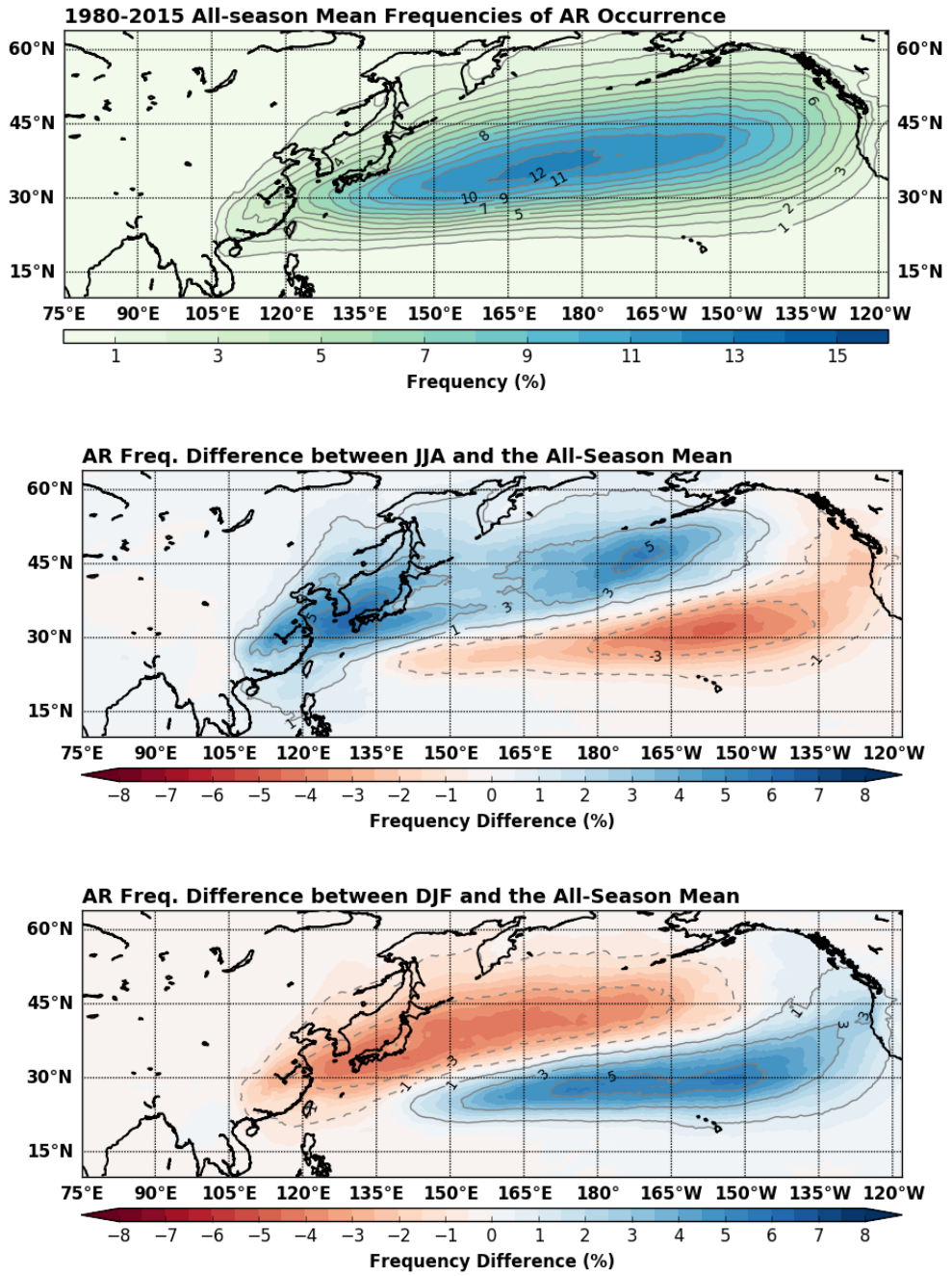

Fig. 3.1 The all-season AR occurrence mean frequencies (top), and the AR frequency differences for JJA (middle), and for DJF (bottom) subtracting the all-season AR frequencies in 1980-2015. Blue (red) color refers to higher (lower) frequency than the annual mean and every positive (negative) odd value is contoured as solid (dash) line.

doi:10.6342/NTU201701272

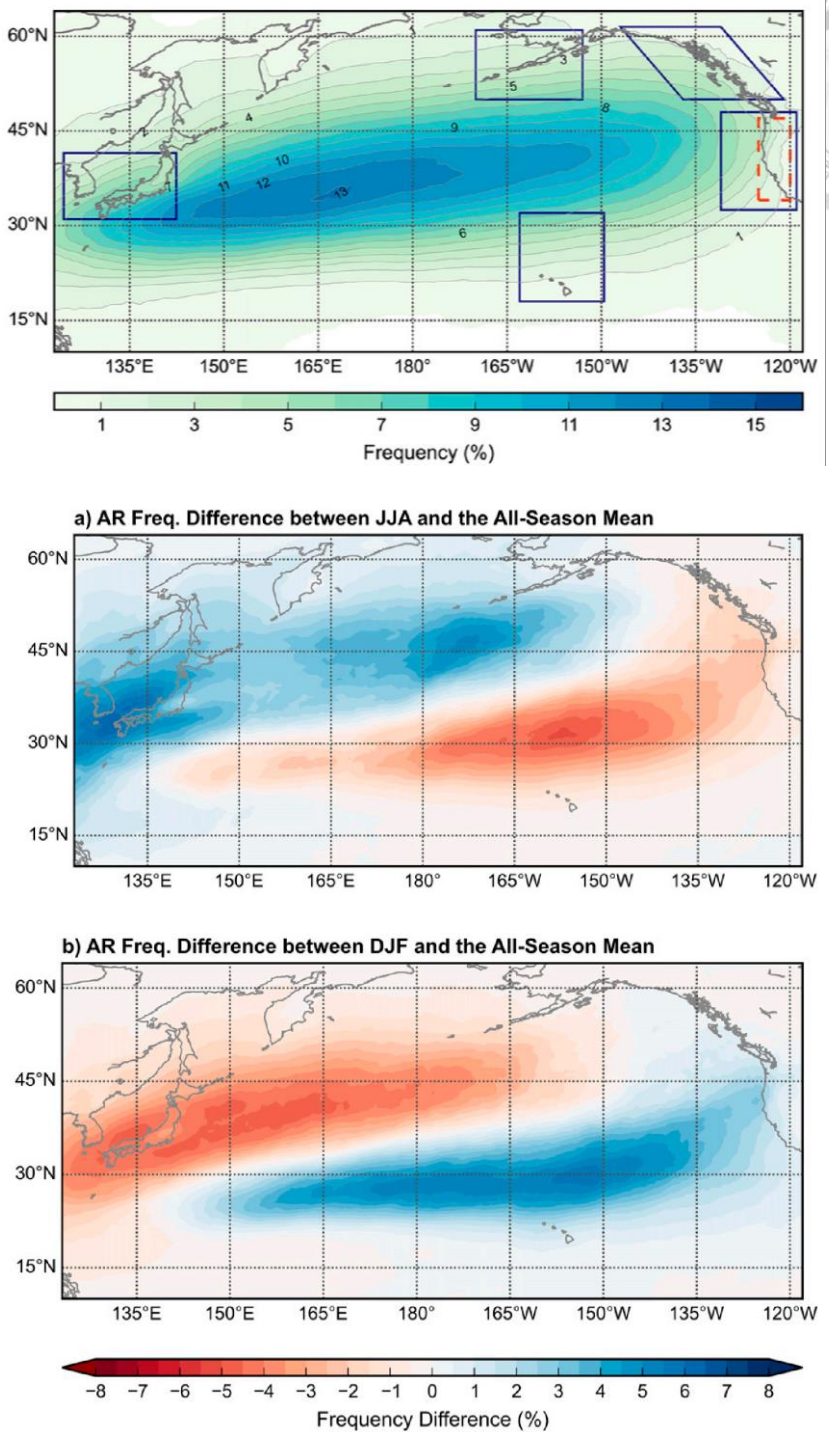

Fig. 3.2 The all-season AR occurrence mean frequencies (top), and the AR frequency differences for JJA (middle), and for DJF (bottom) subtracting the all-season AR frequencies in 1979-2014. Blue (red) color refers to higher (lower) frequency than the annual mean. Adapted from the Fig. 2. (top) and Fig. 5. (middle and bottom) of Mundhenk et al. (2016).

doi:10.6342/NTU201701272

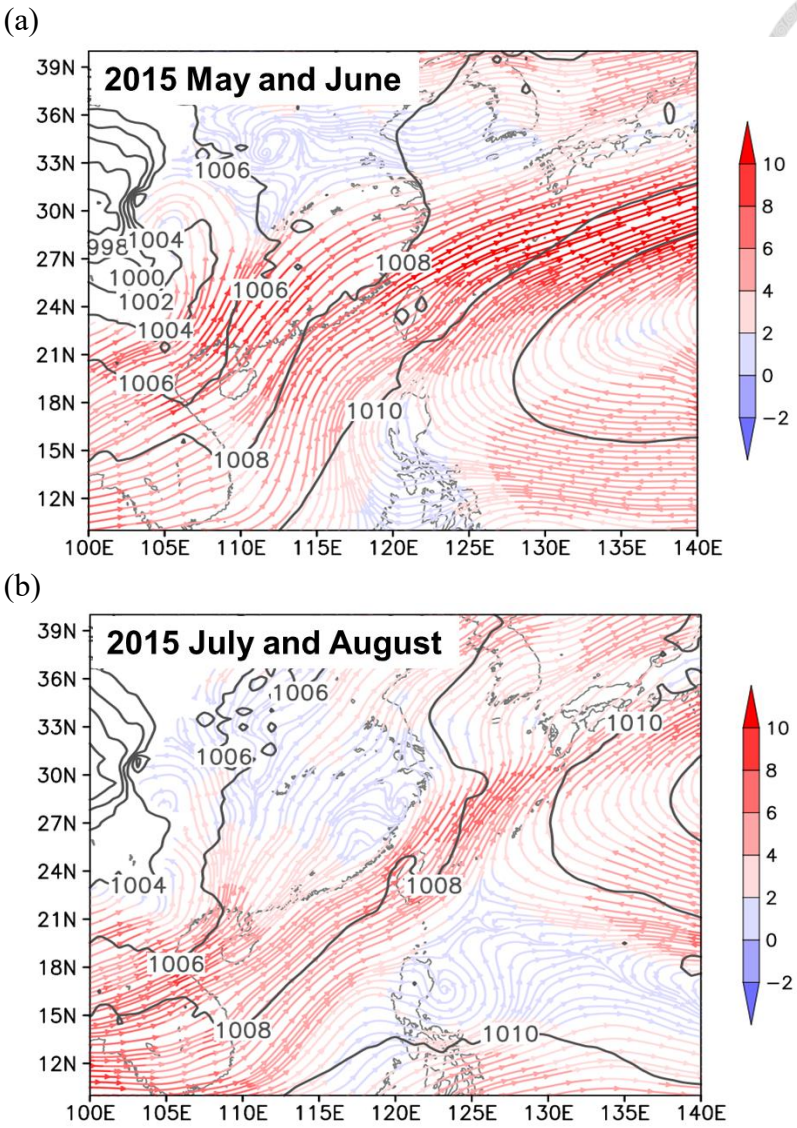

Fig. 3.3 The mean flow patterns of AR periods in May and June (a) and in July and August 2015. The streamline and the colors representing the wind speed (m s^{-1}) is at 850 hPa. The contours shows the sea-level pressure (Pa).

doi:10.6342/NTU201701272

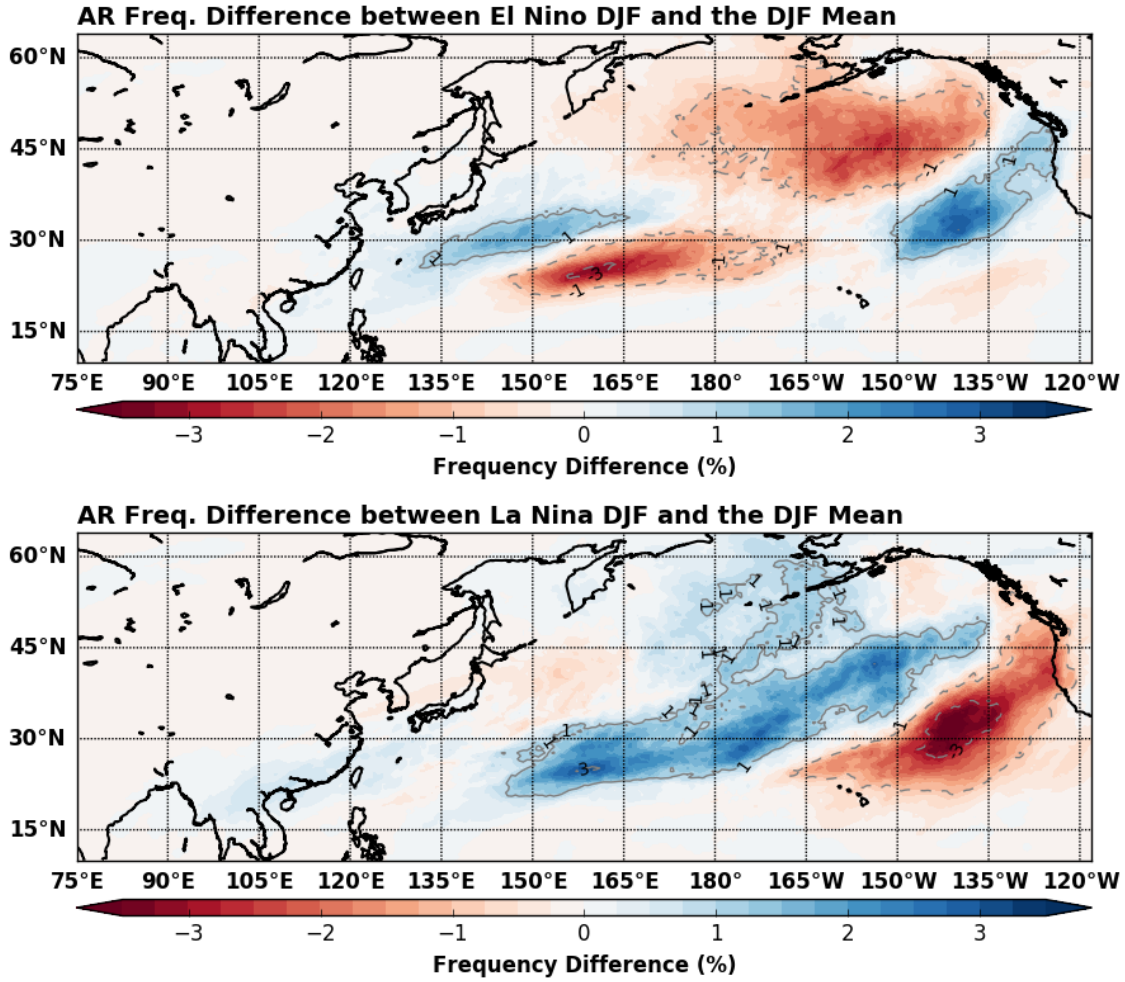

Fig. 3.4 The winter (DJF) AR frequency differences between ENSO phases and the winter AR frequencies in 1980-2015. The El Niño period is shown in the top panel and the La Niña period is in the bottom panel. Blue (red) color refers to higher (lower) frequency than the annual mean and every positive (negative) odd value is contoured as solid (dash) line.

doi:10.6342/NTU201701272

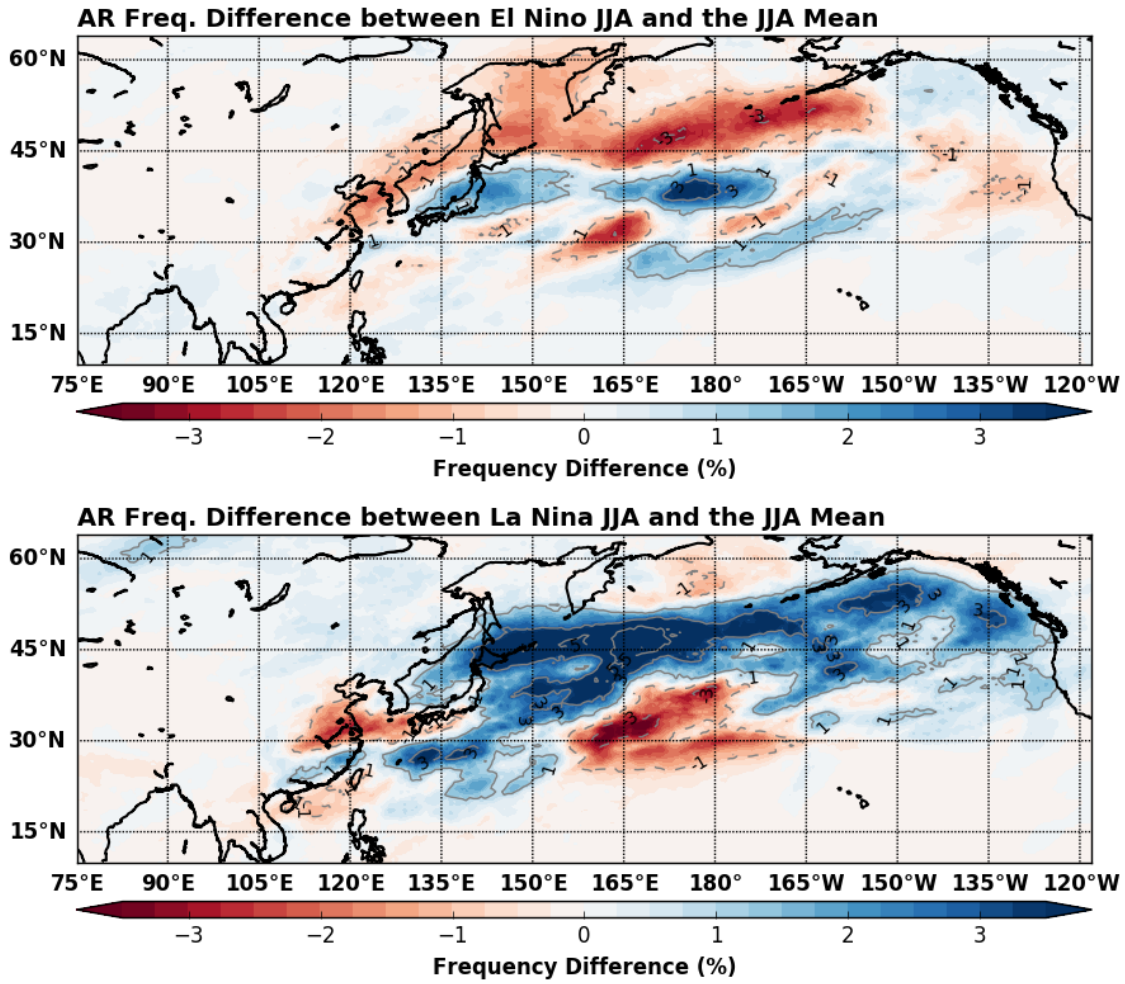

Fig. 3.5 The summer (JJA) AR frequency differences between ENSO phases and the summer AR frequencies in 1980-2015. The El Niño period is shown in the top panel and the La Niña period is in the bottom panel. Blue (red) color refers to higher (lower) frequency than the annual mean and every positive (negative) odd value is contoured as solid (dash) line.

doi:10.6342/NTU201701272

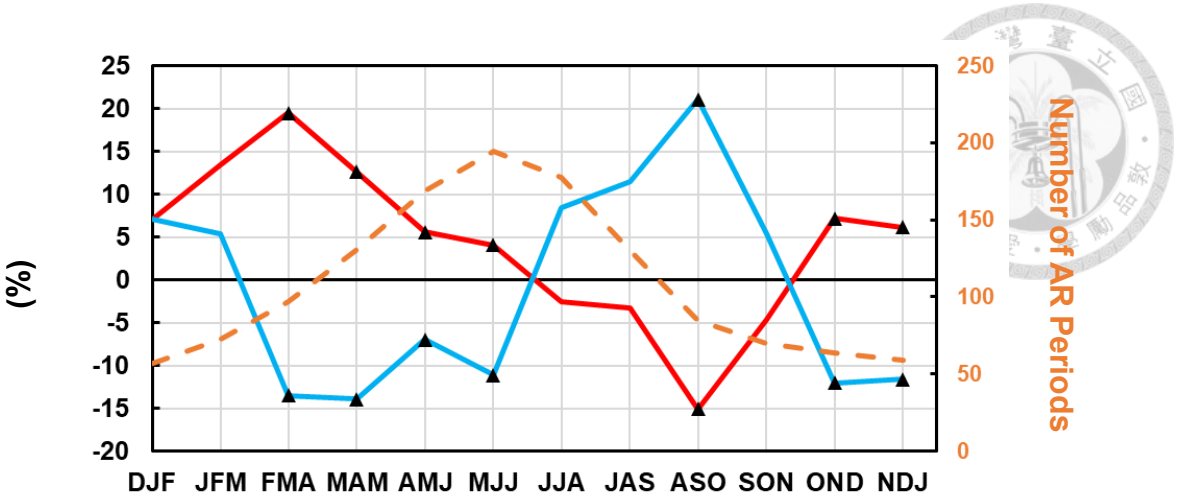

Fig. 3.6 Seasonal variability of displayed as the percent change of the AR frequency in the WNP ($[100^{o}\mathrm{E}, 140^{o}\mathrm{E}] \times [10^{o}\mathrm{N}, 40^{o}\mathrm{N}]$) compared to the 3-month seasonal mean AR frequency according to the left vertical axis. Solid lines represent El Niño (red) and La Niña (blue) conditions. The orange dash line shows the seasonality of the mean number of AR periods within the WNP according to the right vertical axis. The triangles indicate seasons in which the percent change in AR frequency for El Niño periods is statistically significant from La Niña periods at the 90% confidence level based on a t test.

doi:10.6342/NTU201701272

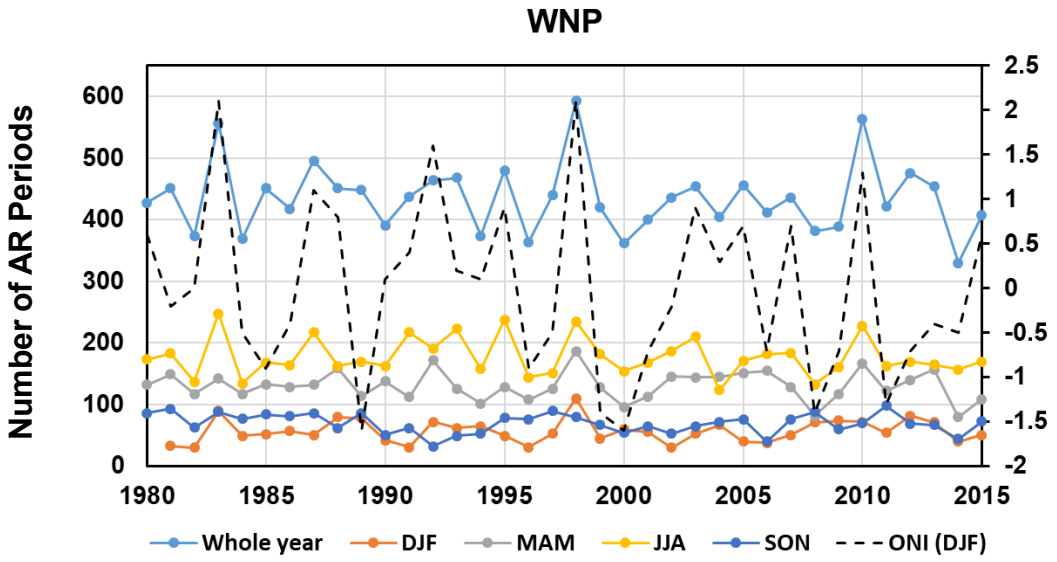

Fig. 3.7 The mean numbers of AR periods with in the Western North Pacific and the ONI index of DJF during 1980-2015. The mean numbers of AR periods are solid lines represent the whole year mean in blue, DJF in orange, MAM in gray, JJA in yellow, and SON in dark blue corresponding to the left vertical axis. The ONI index in DJF is shown in black dash line corresponding to the right vertical axis. The WNP domain is defined by $[100^{o}\mathrm{E}, 140^{o}\mathrm{E}] \times [10^{o}\mathrm{N}, 40^{o}\mathrm{N}]$. Since the data of MERRA-2 start from 1980, there are no December 1979 data and the first point of DJF curve is left blank.

doi:10.6342/NTU201701272

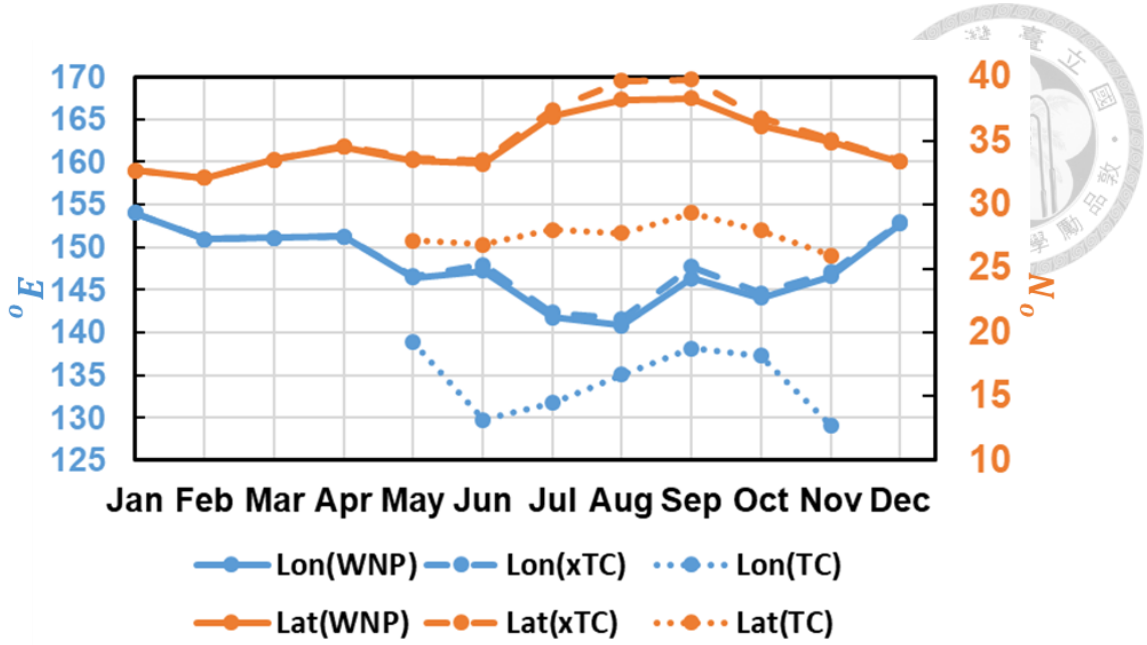

Fig. 3.8 The mean location of the AR centroids in WNP. The blue lines show the mean longitude according to the left vertical axis and the orange lines show the mean latitude according to the right vertical axis. The solid lines represent the mean location of total ARs with centroids in WNP. The long dash lines represent the mean location of ARs without influences of TCs (noted as xTC) and the dot lines represent the mean location of ARs with influence of TCs (noted as TC) in WNP.

doi:10.6342/NTU201701272

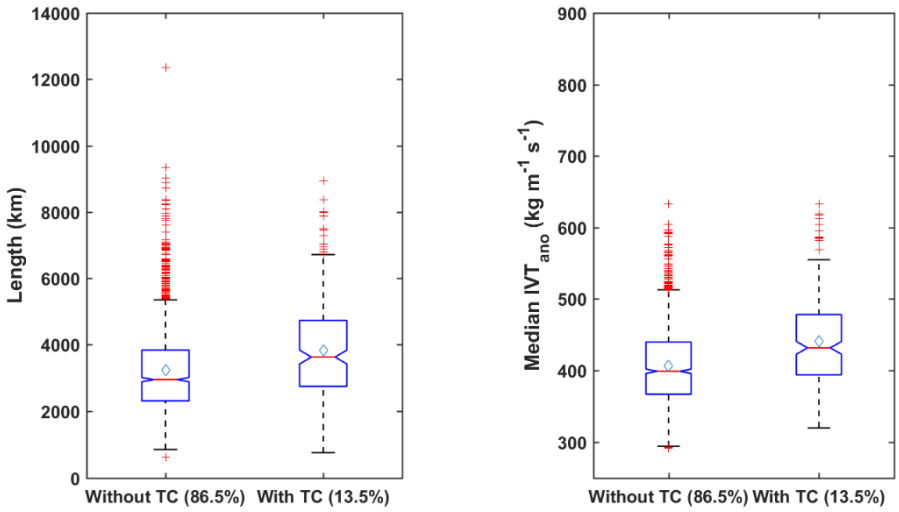

Fig. 3.9 The comparison of the length (left) and the median (middle) anomalous integrated water vapor (IVT) of ARs without/with TC influenced in July and August with centroids in the WNP $[100^{o}\mathrm{E}, 140^{o}\mathrm{E}] \times [10^{o}\mathrm{N}, 40^{o}\mathrm{N}]$. The "Without TC" group of ARs includes every AR that don't coexist with any TCs in a circle of radius 1000km centered at the AR's centroid; otherwise, ARs are classified into the group of "With TC". The values in the brackets show how much percentage of total 1639 detected ARs during July and August each group has in the WNP. The details of these boxplot is in Chapter 3.1.2.

doi:10.6342/NTU201701272

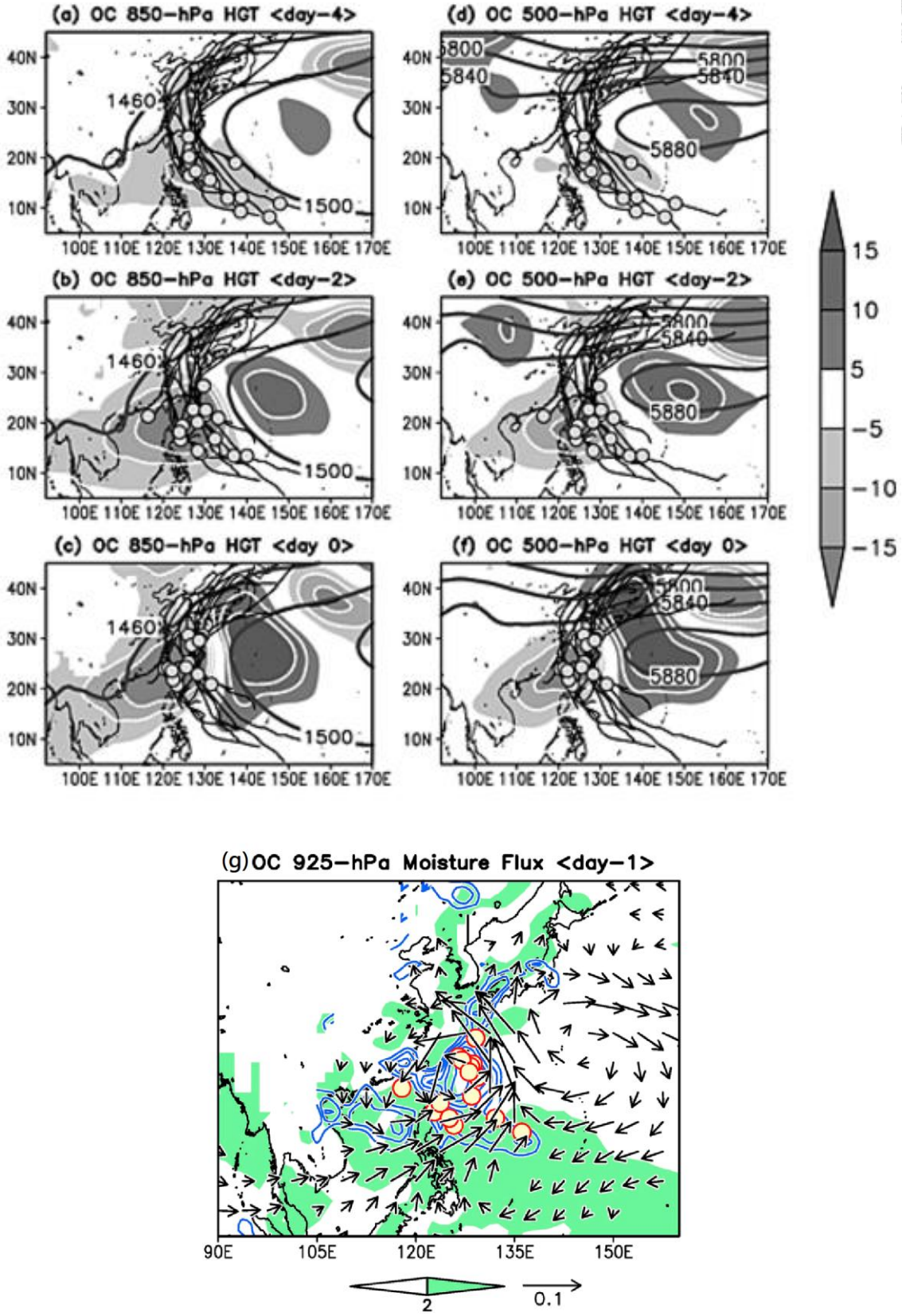

Fig. 3.10 (a–c) Composite maps of filtered 850 hPa geopotential height anomalies (shaded) on day -4, day -2, and day 0 for category OC. The filter combines two low-

doi:10.6342/NTU201701272

pass filters: 3-day-weighted running average and 31-day-weighted running average. The background states of 850 hPa geopotential height (contours) are depicted. The contoured and shaded intervals are 40 m and 5 m, respectively. The location and track of the typhoons as identified by the best track data provided by the Regional Specialized Meteorological Center (RSMC) Tokyo-Typhoon Center are shown with circles. Day 0 denotes the day of maximum development of the typhoons. The right panels (d-f) are the same as the left panels but for 500 hPa geopotential height. Adapted from Fig. 3 by Hirata and Kawamura (2014). (g) is the same composite map but for filtered 925 hPa moisture flux anomalies (vectors) and their flux convergences (blue contours) on day -1. The contoured interval is 1.0×10^{-8} kg kg^{-1} s^{-1}. Anomalies of less than 2.0×10^{-8} kg kg^{-1} s^{-1} have been suppressed. The reference arrow is 0.1 kg kg^{-1} m s^{-1}. Fluxes of less than 0.01 kg kg^{-1} m s^{-1} have been suppressed. Superimposed is the background state of 925 hPa moisture flux convergence (shaded). The shaded interval is 2.0×10^{-8} kg kg^{-1} s^{-1}. Adapted from Fig. 6 (b) by Hirata and Kawamura (2014).

doi:10.6342/NTU201701272

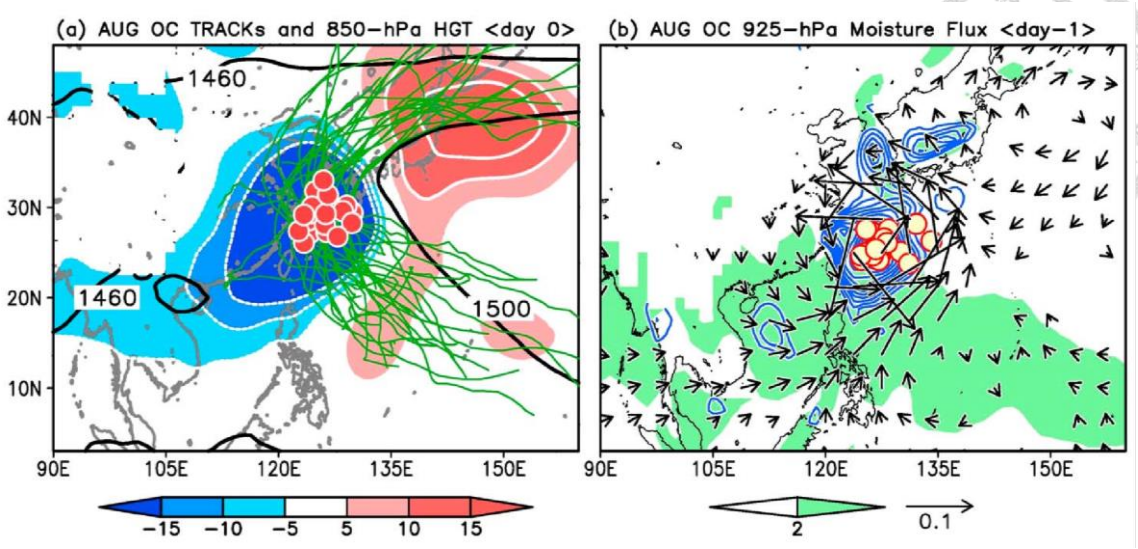

Fig. 3.11 (a) Composite map of filtered 850 hPa geopotential height anomalies (shaded) on day 0 for category OC in August. The filter combines two low-pass filters: 3-day-weighted running average and 31-day-weighted running average. The background state of 850 hPa geopotential height (black contours) is superimposed. The contoured and shaded intervals are 40 m and 5 m, respectively. The locations of the typhoons are depicted with circles. (b) The same as in Figure 12a but for filtered 925 hPa moisture flux anomalies (vectors) and their flux convergences (blue contours) on day -1. The contoured interval is 1.0×10^{-8} kg kg^{-1} s^{-1}. Anomalies of less than 2.0×10^{-8} kg kg^{-1} s^{-1} have been suppressed. The reference arrow is 0.1 kg kg^{-1} m s^{-1}. Fluxes of less than 0.01 kg kg^{-1} m s^{-1} have been suppressed. Superimposed is the background state of 925 hPa moisture flux convergence (shaded). The shaded interval is 2.0×10^{-8} kg kg^{-1} s^{-1}. Adapted from Fig. 12 by Hirata and Kawamura (2014).

doi:10.6342/NTU201701272

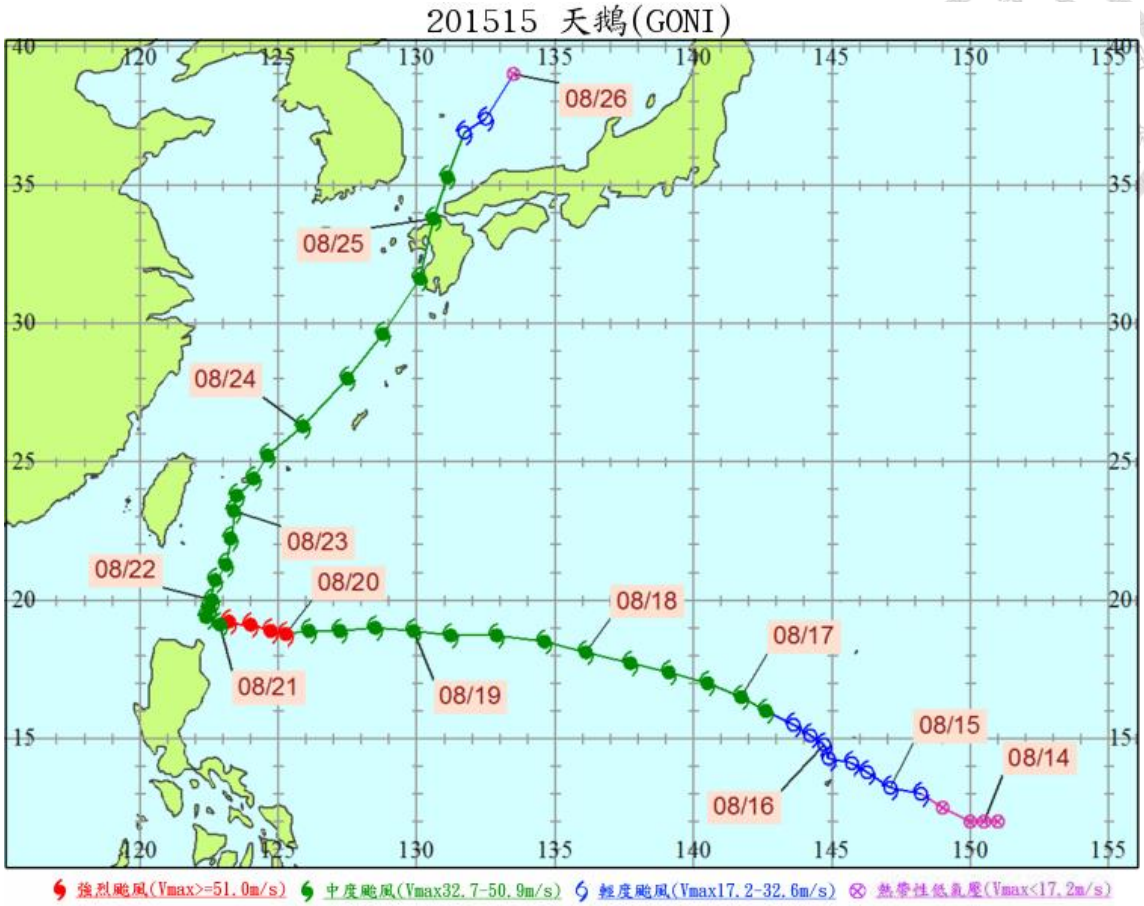

Fig. 3.12 The track of TC Goni. The data source is Central Weather Bureau (CWB).

doi:10.6342/NTU201701272

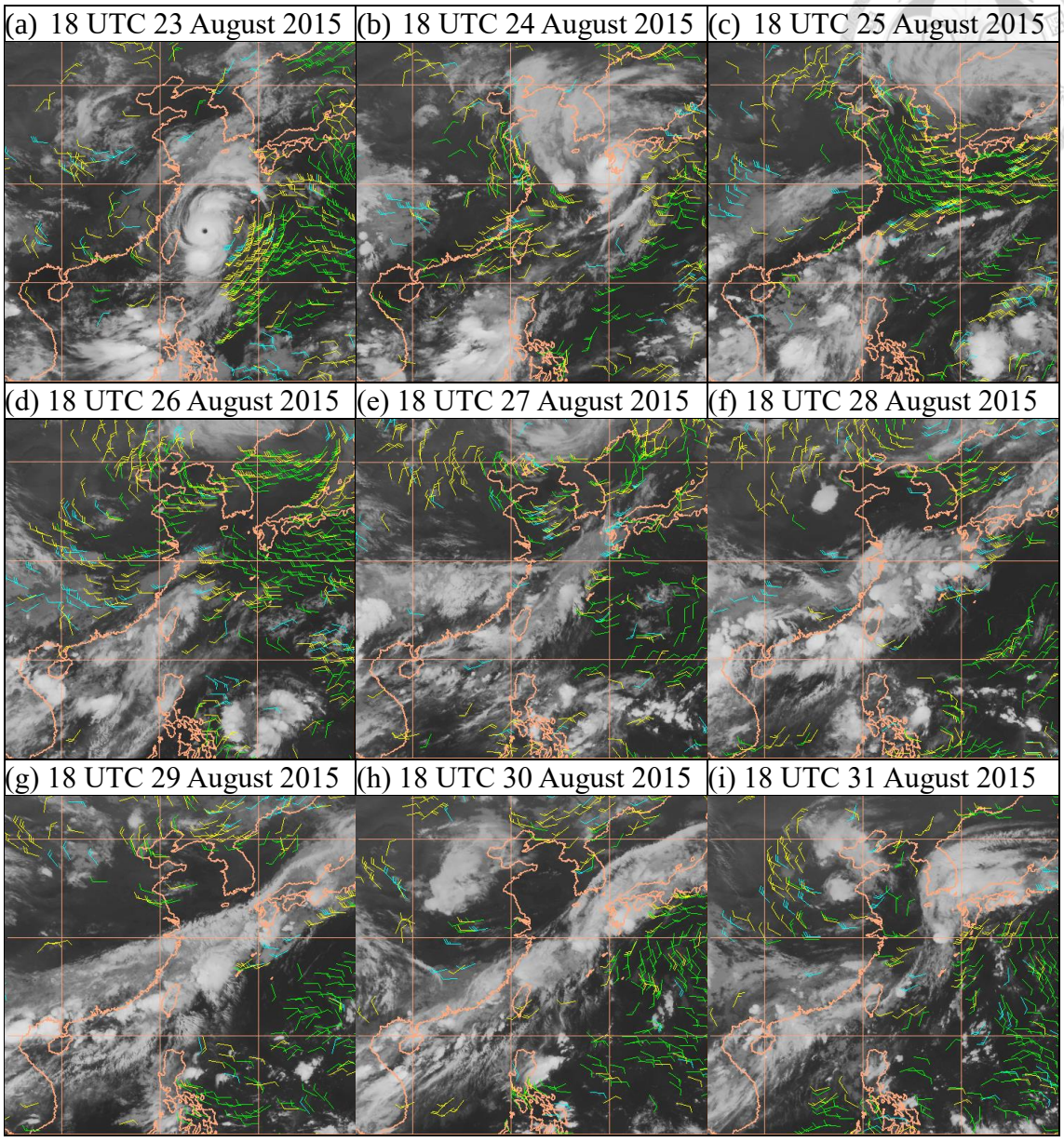

Fig. 3.13 The geostationary infrared satellite imagery (11μm) with overlaid satellite derived low-level cloud drift winds during 23-31 August 2015. The low-level cloud-drift winds (green: 800-950 hPa, yellow: 600-799 hPa, cyan: 400-599 hPa) are created by a combination of both visible and infrared imagery, comprised of coverage by the METEOSAT-5, MTSAT-1R, and GOES-West satellites. The data source is CIMSS (Cooperative Institute for Meteorological Satellite Studies).

doi:10.6342/NTU201701272

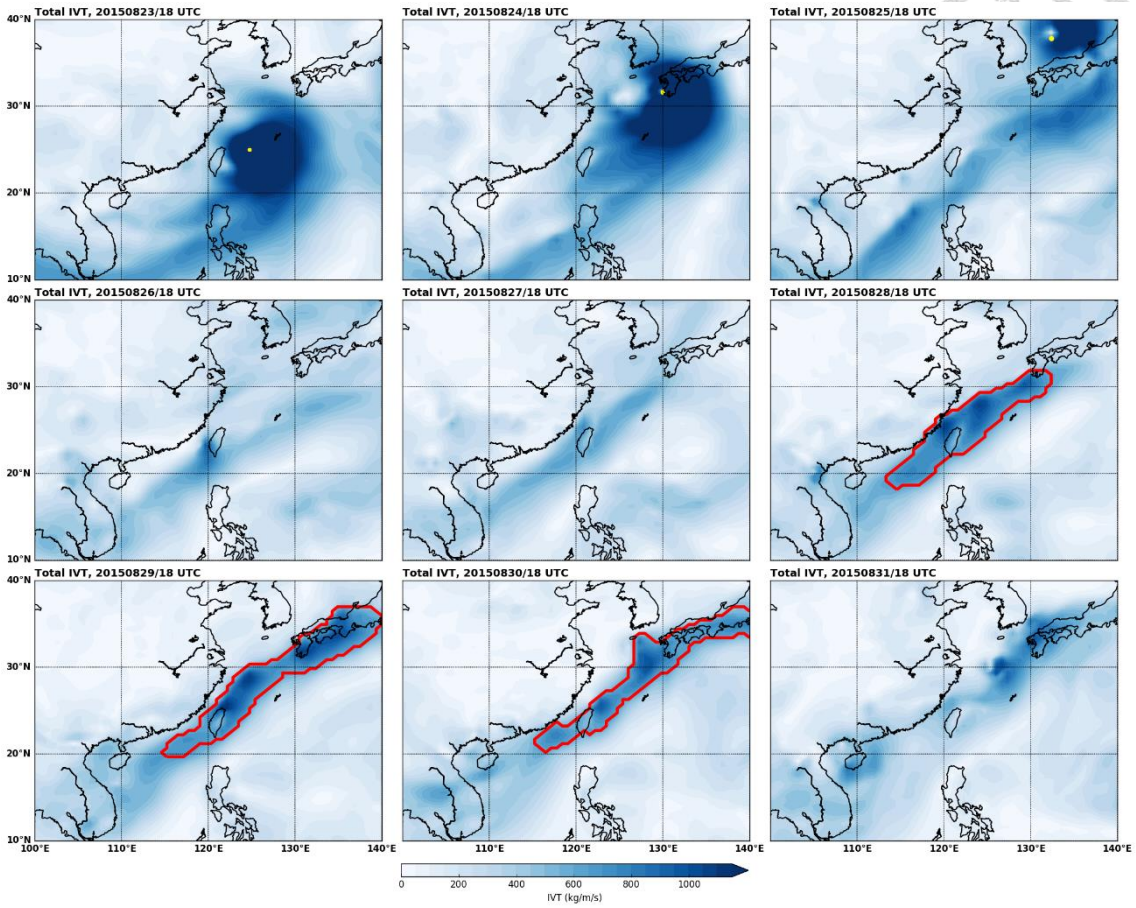

Fig. 3.14 The results of modified AR algorithm during 23-31 August 2015 and the ARs evolution. The integrated water vapor transport (kg m^{-1} s^{-1}) is shaded and the features detected as ARs are contoured in red.

doi:10.6342/NTU201701272

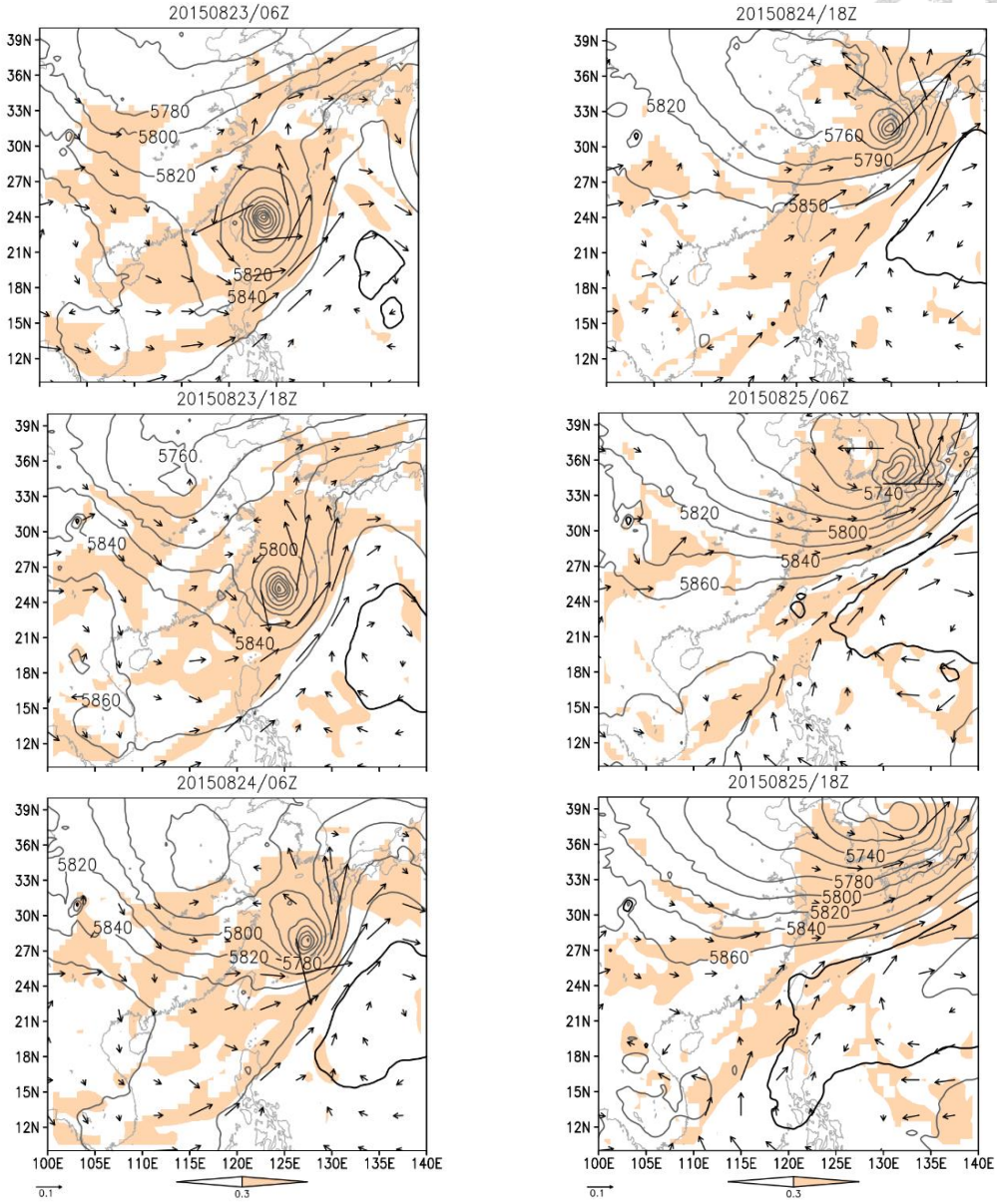

Fig. 3.15 The evolution of TC Goni and the ridge of the Pacific subtropical high during 23-25 August 2015. The subtropical high is depicted as the black contour representing the 5880 m isobaric line and other gray contours represent the isobaric lines at 500 hPa with 20 m interval. The potential vorticity (PVU; shaded) and the water vapor flux (kg kg^{-1} m s^{-1}; arrow) are calculated at 320 K isentropic surface. The PV field and the water vapor flux are suppressed if the grids have water vapor flux less than 0.02 kg kg^{-1} m s^{-1}.

doi:10.6342/NTU201701272

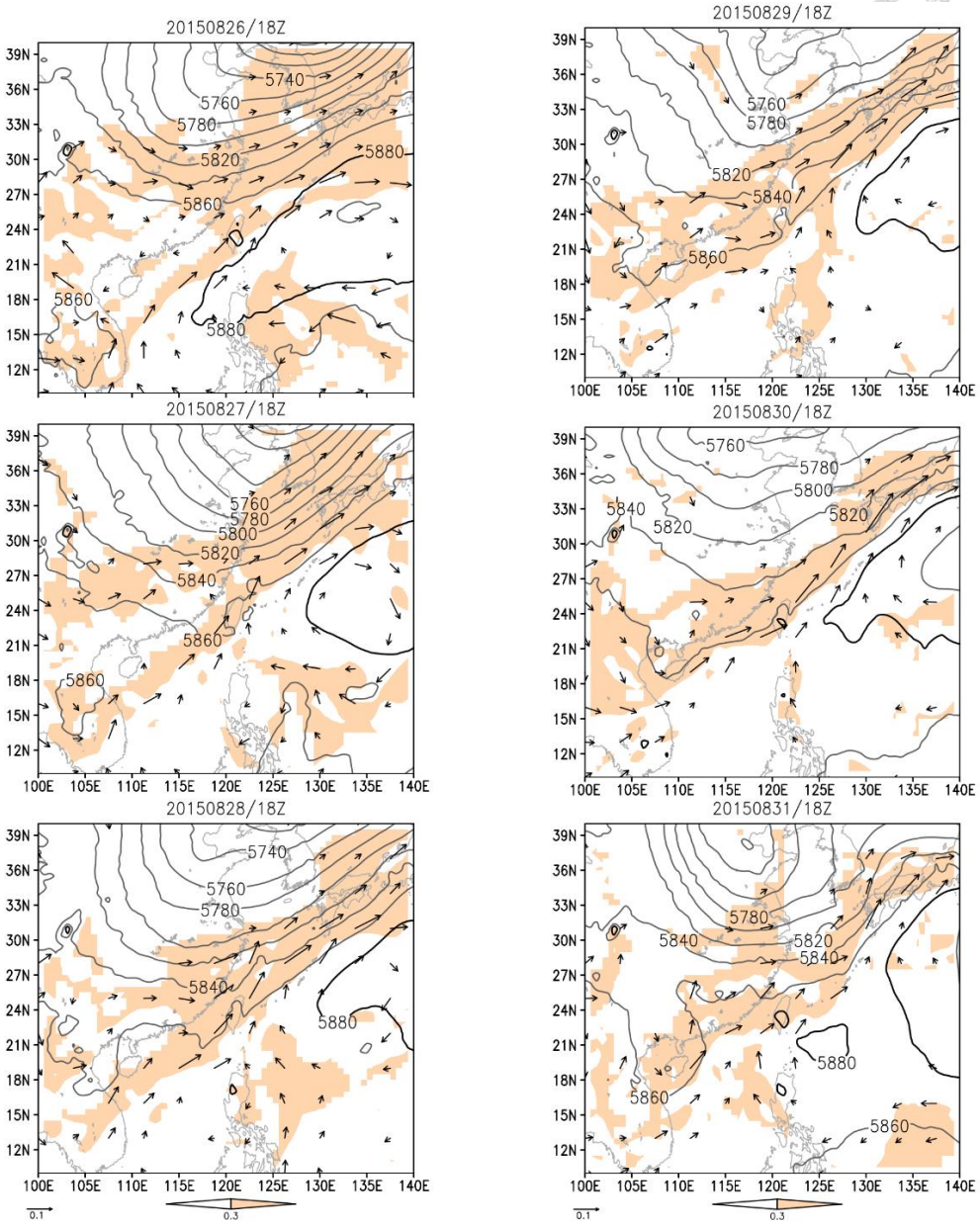

Fig. 3.16 The evolution of the trough and the AR during 26-31 August 2015. The shaded regions, contours, and arrows are the same as those in Fig. 3.15.

doi:10.6342/NTU201701272

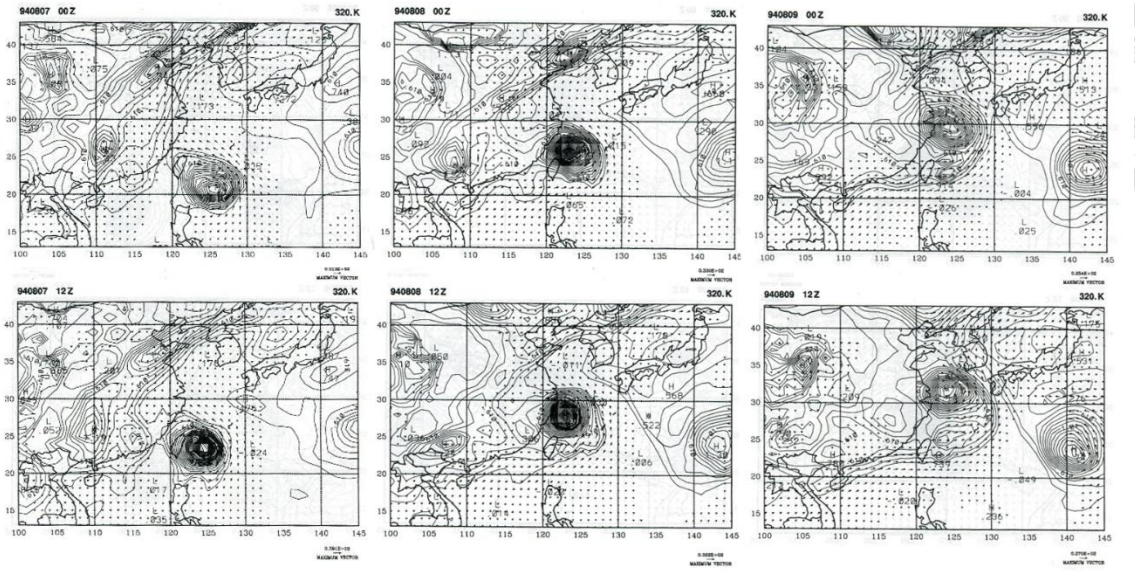

Fig. 3.17 The potential vorticity on 320 K isentropic surface (contoured; PVU) calculated from ECMWF during 07-08 August1994. The interval of contour is 0.1 PVU. The strong circulation roughly depicted the location of TC Doug and the wind vectors show the region with south component of wind larger than 0.3 $\mathrm{m\ s^{-1}}$.

doi:10.6342/NTU201701272

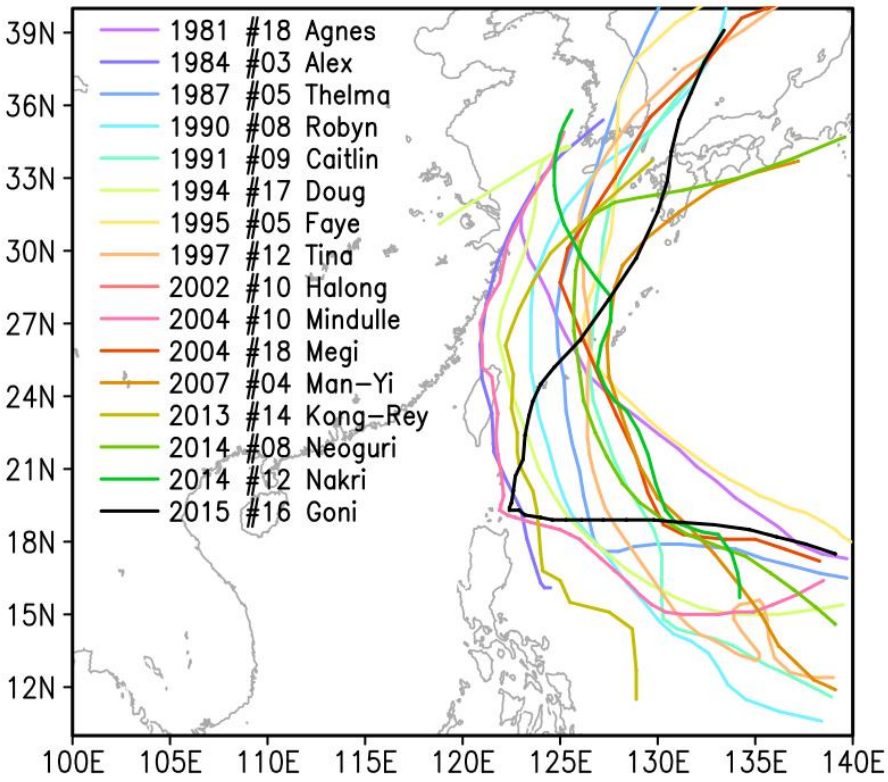

Fig. 3.18 The tracks of the 16 cases used in the composite in Fig. 3.19.

doi:10.6342/NTU201701272

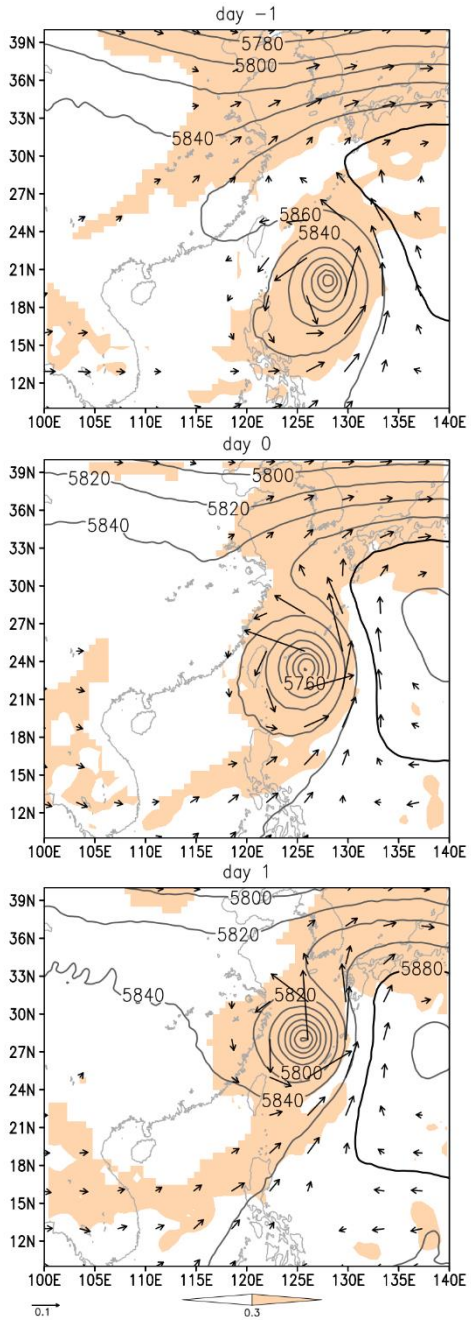

Fig. 3.19 The composite of 16 cases with similar TC tracks showing the AR evolution. The potential vorticity (PV; shaded) and the water vapor flux (arrow) are calculated at 320 K isentropic surface. The PV field and the water vapor flux are suppressed if the grids have water vapor flux less than 0.02 kg kg^{-1} m s^{-1}. The contours show the geopotential high at 500 hPa. The day 0 is defined as the maximum intensity of each TC over 20^{o}N.

doi:10.6342/NTU201701272

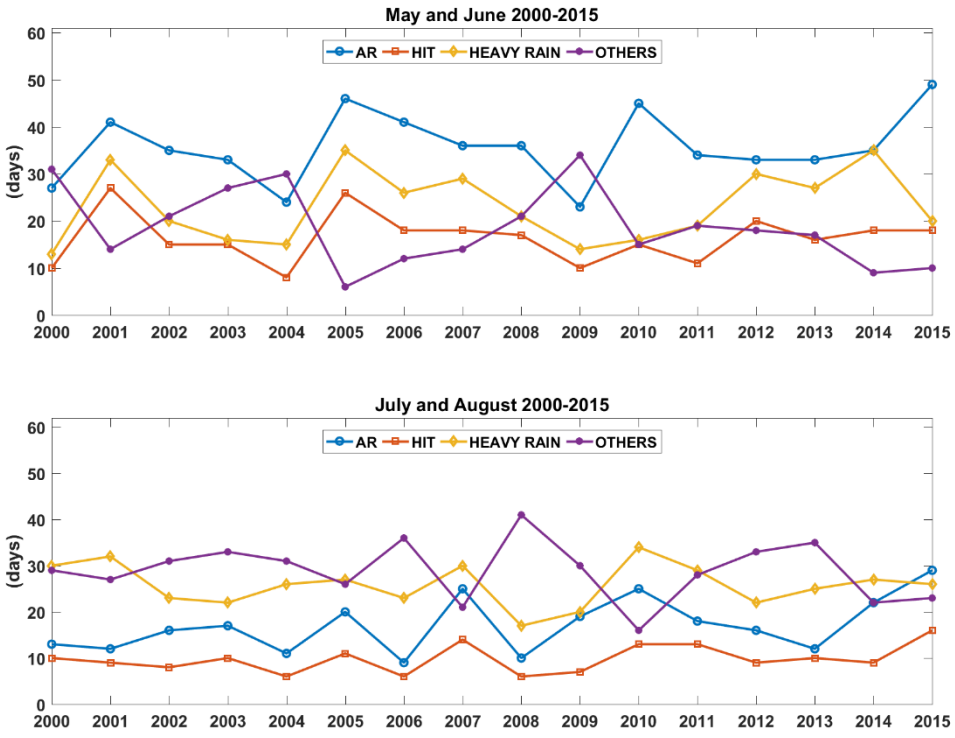

Fig. 3.20 The number of days that Taiwan are influenced by ARs in May and June (top) or in July and August (bottom) during 2000-2015. The definition of the four groups can be find in Chapter 2.2.3.

doi:10.6342/NTU201701272

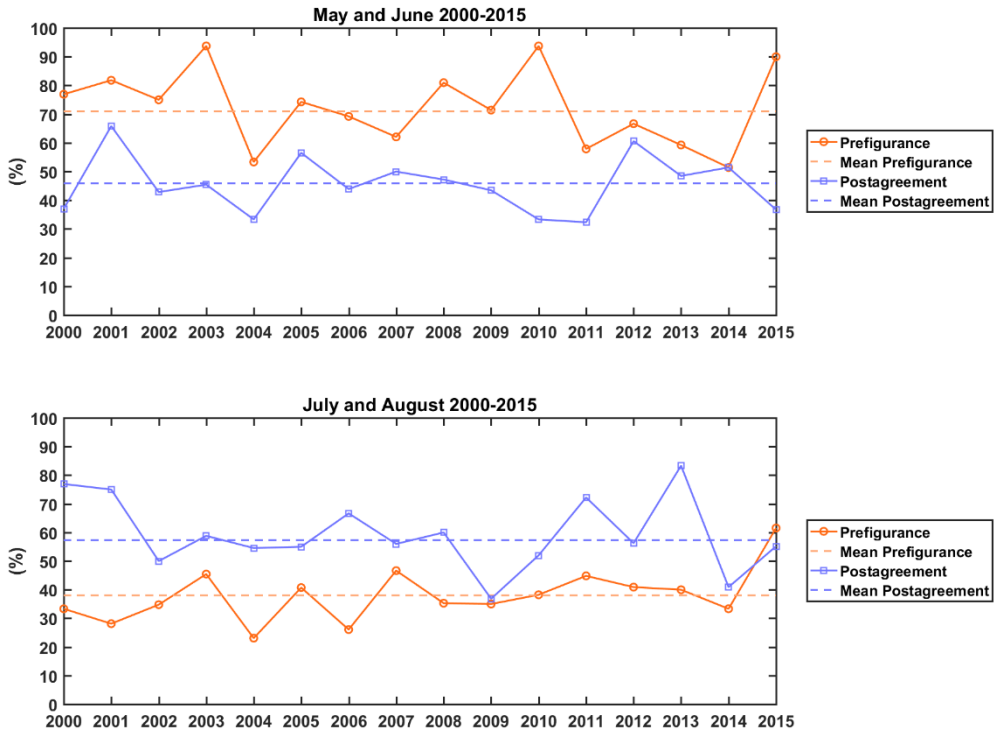

Fig. 3.21 The prefigurance and the postagreement in May and June (top) or July and August (bottom) during 2000-2015 are denoted in solid line. The mean values of them are in dash line.

doi:10.6342/NTU201701272

Chapter 4 Conclusions

Statistics of atmospheric rivers (ARs) and the impact of tropical cyclones (TCs) in Western North Pacific (WNP) region including the domain of $[100^{o}\mathrm{E}, 140^{o}\mathrm{E}] \times [10^{o}\mathrm{N}, 40^{o}\mathrm{N}]$ are provided in this study for their potential societal importance of the East Asian coastal region. The modified occurrence-based detection algorithm of AR using MERRA-2 reanalysis data and the best track data of JTWC was applied to the anomalous integrated water vapor transport (IVT) fields from 1980 to 2015 for identifying the extraordinary IVT features. One of these severe cases in the late August 2015 motivated us to investigate to what extend TCs can enhance ARs and how TCs help AR formation and maintenance in the sub-latitudes WNP. The modified AR algorithm was also applied to the total IVT fields in 2000 – 2015 to include more filamentary features for linking the occurrence of AR to the extreme rainfall events defined according to the hourly rain rate data among 200 surface observation stations of CWB. The major findings in this study are summarized in brief as follows:

1. Considering the mean all-season AR frequency and the mean AR frequency differences of JJA and DJF from the all-season mean, the differences between our results and Mundhenk et al (2016) in the WNP show the necessary additional criterion on excluding round features containing TCs for further comparison of ARs with and without TC influences.
2. On average, ARs with TCs are 600 km longer and are 1.1 times more intensive than those without TC.
3. The long lasting AR in the late August 2015 was attributed to the interaction between TC Goni and the subtropical high, and to the interaction between TC Goni and the upper trough.

doi:10.6342/NTU201701272

4. Through the composite of 16 ARs cases accompanied with TCs with similar tracks, we found that TCs are likely to help ARs to form at low latitude through uniting the potential vorticity (PV) strips.
5. During the “Mei-Yu Season” in May and June, the mean prefigurance is as high as 71.0% and the mean postagreement is 45.9%; on the contrary, during the “Typhoon Season” in July and August, the postagreement is 57.3% and the prefigurance is 38.0%. These opposite results show that most of the extreme rainfall events are associated with ARs in the “Mei-Yu Season” while over half of the ARs in the “Typhoon Season” are associated with extreme rainfall in Taiwan.

This study extends the scope of AR research to the coastal region of the WNP and highlights the importance of the interaction between a TC and its surroundings. According to our study, this interaction may induce, enhance and maintain the AR in the WNP. In addition, the analyses of ARs are beneficial to the forecast of the extreme rainfall events in Taiwan. Further studies on the mechanisms of the interaction and the relationship with extreme rainfall are necessary to improve our understandings of this phenomenon.

doi:10.6342/NTU201701272

REFERENCE

季明立，1997：颱風離台引進西南氣流探討，國立台灣大學大氣科學研究所碩士論文，128 頁。

Archambault, H. M., L. F. Bosart, D. Keyser, and J. M. Cordeira, 2013: A climatological analysis of the extratropical flow response to recurving western North Pacific tropical cyclones. *Monthly Weather Review*, **141,** 2325-2346.

Bao, J., S. Michelson, P. Neiman, F. Ralph, and J. Wilczak, 2006: Interpretation of enhanced integrated water vapor bands associated with extratropical cyclones: Their formation and connection to tropical moisture. *Monthly weather review*, **134,** 1063-1080.

Bosart, L. F., B. J. Moore, J. M. Cordeira, and H. M. Archambault, 2017: Interactions of North Pacific tropical, midlatitude, and polar disturbances resulting in linked extreme weather events over North America in October 2007. *Monthly Weather Review*, **145,** 1245-1273.

Browning, K. A., 1990: Organization of clouds and precipitation in extratropical cyclones. *Extratropical Cyclones: The Erik Palmén Memorial Volume***,** 129-153.

Carlson, T. N., 1991: *Mid-latitude weather systems.* United States: New York, NY (United States); Routledge, Chapman Hall, Inc., 507 pp.

Cavazos, T., and D. Rivas, 2004: Variability of extreme precipitation events in Tijuana, Mexico. *Climate Research*, **25,** 229-243.

Chambers, J., W. Cleveland, B. Kleiner, and P. A. Tukey, 1983: Comparing data distributions. *Graphical Methods for Data Analysis (Bell Laboratories)***,** 47-73.

Cordeira, J. M., F. M. Ralph, and B. J. Moore, 2013: The development and evolution of two atmospheric rivers in proximity to western North Pacific tropical cyclones in October 2010. *Monthly Weather Review*, **141,** 4234-4255.

Davis, C. A., and K. A. Emanuel, 1991: Potential vorticity diagnostics of cyclogenesis. *Monthly weather review*, **119,** 1929-1953.

Dettinger, M. D., F. M. Ralph, T. Das, P. J. Neiman, and D. R. Cayan, 2011: Atmospheric rivers, floods and the water resources of California. *Water*, **3,** 445-478.

Dirmeyer, P., J. Kinter III, A. Michalak, and R. Jackson, 2009: The "Maya Express": Floods in the US Midwest. *Eos*, **90,** 101-102.

Gimeno, L., R. Nieto, M. Vázquez, and D. A. Lavers, 2014: Atmospheric rivers: a mini-review. *Frontiers in Earth Science*, **2,** 2.

Guan, B., N. P. Molotch, D. E. Waliser, E. J. Fetzer, and P. J. Neiman, 2010: Extreme snowfall events linked to atmospheric rivers and surface air temperature via satellite

doi:10.6342/NTU201701272

measurements. *Geophysical Research Letters*, **37**.

Hirata, H., and R. Kawamura, 2014: Scale interaction between typhoons and the North Pacific subtropical high and associated remote effects during the Baiu/Meiyu season. *Journal of Geophysical Research: Atmospheres*, **119,** 5157-5170.

Knippertz, P., and H. Wernli, 2010: A Lagrangian climatology of tropical moisture exports to the Northern Hemispheric extratropics. *Journal of Climate*, **23,** 987-1003.

Knippertz, P., H. Wernli, and G. Gläser, 2013: A global climatology of tropical moisture exports. *Journal of Climate*, **26,** 3031-3045.

Knippertz, P., and J. E. Martin, 2007: A Pacific moisture conveyor belt and its relationship to a significant precipitation event in the semiarid southwestern United States. *Weather and forecasting*, **22,** 125-144.

Kållberg, P., P. Berrisford, B. Hoskins, A. Simmons, S. Lamy-thépaut, and R. Hine, 2005: ERA-40 atlas. ERA-40 Project Report Series 19, ECMWF, 103 pp.

Lackmann, G. M., and J. R. Gyakum, 1999: Heavy cold-season precipitation in the northwestern United States: Synoptic climatology and an analysis of the flood of 17–18 January 1986. *Weather and forecasting*, **14,** 687-700.

Lavers, D. A., and G. Villarini, 2013: The nexus between atmospheric rivers and extreme precipitation across Europe. *Geophysical Research Letters*, **40,** 3259-3264.

Lavers, D. A., G. Villarini, R. P. Allan, E. F. Wood, and A. J. Wade, 2012: The detection of atmospheric rivers in atmospheric reanalyses and their links to British winter floods and the large-scale climatic circulation. *Journal of Geophysical Research: Atmospheres*, **117**.

McGuirk, J. P., A. H. Thompson, and N. R. Smith, 1987: Moisture bursts over the tropical Pacific Ocean. *Monthly weather review*, **115,** 787-798.

Mundhenk, B. D., E. A. Barnes, and E. D. Maloney, 2016: All-season climatology and variability of atmospheric river frequencies over the North Pacific. *Journal of Climate*, **29,** 4885-4903.

Nayak, M. A., G. Villarini, and D. A. Lavers, 2014: On the skill of numerical weather prediction models to forecast atmospheric rivers over the central United States. *Geophysical Research Letters*, **41,** 4354-4362.

Neiman, P. J., F. M. Ralph, G. A. Wick, J. D. Lundquist, and M. D. Dettinger, 2008a: Meteorological characteristics and overland precipitation impacts of atmospheric rivers affecting the West Coast of North America based on eight years of SSM/I satellite observations. *Journal of Hydrometeorology*, **9,** 22-47.

Neiman, P. J., and Coauthors, 2008b: Diagnosis of an intense atmospheric river impacting the Pacific Northwest: Storm summary and offshore vertical structure observed with

doi:10.6342/NTU201701272

COSMIC satellite retrievals. *Monthly Weather Review*, **136,** 4398-4420.

Newell, R. E., N. E. Newell, Y. Zhu, and C. Scott, 1992: Tropospheric rivers?–A pilot study. *Geophysical research letters*, **19,** 2401-2404.

Payne, A. E., and G. Magnusdottir, 2014: Dynamics of landfalling atmospheric rivers over the North Pacific in 30 years of MERRA reanalysis. *Journal of Climate*, **27,** 7133-7150.

Peixoto, J. P., and A. H. Oort, 1992: Physics of climate. Institude of Physics, 520pp.

Ralph, F. M., P. J. Neiman, and G. A. Wick, 2004: Satellite and CALJET aircraft observations of atmospheric rivers over the eastern North Pacific Ocean during the winter of 1997/98. *Monthly Weather Review*, **132,** 1721-1745.

Ralph, F. M., P. J. Neiman, and R. Rotunno, 2005: Dropsonde observations in low-level jets over the northeastern Pacific Ocean from CALJET-1998 and PACJET-2001: Mean vertical-profile and atmospheric-river characteristics. *Monthly weather review*, **133,** 889-910.

Ralph, F. M., P. J. Neiman, G. A. Wick, S. I. Gutman, M. D. Dettinger, D. R. Cayan, and A. B. White, 2006: Flooding on California's Russian River: Role of atmospheric rivers. *Geophysical Research Letters*, **33**.

Ramos, A. M., R. M. Trigo, M. L. Liberato, and R. Tomé, 2015: Daily precipitation extreme events in the Iberian Peninsula and its association with atmospheric rivers. *Journal of Hydrometeorology*, **16,** 579-597.

Ramos, A. M., R. M. Trigo, M. L. Liberato, and D. A. Lavers, 2016: Atmospheric rivers moisture sources from a Lagrangian perspective. *Earth System Dynamics*, **7,** 371.

Rienecker, M. M., and Coauthors, 2011: MERRA: NASA's modern-era retrospective analysis for research and applications. *Journal of climate*, **24,** 3624-3648.

Rivera, E. R., F. Dominguez, and C. L. Castro, 2014: Atmospheric rivers and cool season extreme precipitation events in the Verde River basin of Arizona. *Journal of Hydrometeorology*, **15,** 813-829.

Wang, B., R. Wu, and X. Fu, 2000: Pacific–East Asian teleconnection: how does ENSO affect East Asian climate? *Journal of Climate*, **13,** 1517-1536.

Wang, B., B. Xiang, and J.-Y. Lee, 2013: Subtropical high predictability establishes a promising way for monsoon and tropical storm predictions. *Proceedings of the National Academy of Sciences*, **110,** 2718-2722.

Wick, G. A., P. J. Neiman, and F. M. Ralph, 2013: Description and validation of an automated objective technique for identification and characterization of the integrated water vapor signature of atmospheric rivers. *IEEE Transactions on Geoscience and Remote Sensing*, **51,** 2166-2176.

doi:10.6342/NTU201701272

Yoshida, K., 2012: Indirect effects of tropical cyclones on heavy rainfall events in Kyushu, Japan, during the Baiu season. *Journal of the Meteorological Society of Japan. Ser. II*, **90,** 377-401.

Zhu, Y., and R. E. Newell, 1998: A proposed algorithm for moisture fluxes from atmospheric rivers. *Monthly weather review*, **126,** 725-735.

doi:10.6342/NTU201701272

Appendix A. The Modified AR Detection Algorithm

modified_merra_ar_6hly_regional_analysis_web.py Page 1 of 12

```
#!/usr/local/bin/python
# ----------------------------------------------------------------------------
# Program: modified_merra_ar_6hly_regional_analysis_web.py
#
# Purpose:
# Manipulates the pre-calculated IVT files to isolate atmospheric rivers (ARs)
# from within positive IVT anomalies, using the pre-processed FFT file for the
# long-term mean and seasonal cycle.
#
# Defined Functions:
# days_in_month - Provides the number of days in a month
# distance_2points - Calculate the distance of two points
# save_binary - Saves array as NumPy binary file
# read_data_anoIVT - Read in the anomalous IVT data
# read_data_totalIVT - Read in the anomalous IVT data
# skeleton_length - Approximates feature length in km
#
# History:
# B. Mundhenk, Sep 2014; Created for exploratory global analysis of ARs
#              Mar 2015; Adjusted for regional use and relaxed thresholds
#              Jul 2015; Modified for web posting
# Ying-Ju Chen, May 2017; Modified the web posting code of B. Mundhenk
#
# ----------------------------------------------------------------------------

import csv
import datetime
import operator
import socket
import sys
import time
import os
import numpy as np
from math import sin, cos, sqrt, atan2, radians
from scipy import ndimage
from skimage.measure import regionprops
from skimage.feature import peak_local_max
from skimage.segmentation import random_walker
from skimage.morphology import skeletonize

# ------------------------- Setting Output and Control Variables ------------------
save_csv = False # Optional saving of AR characteristics in CSV file only WPAC,
#-------------------------------------------------------------------------------
-

data_str = 'MERRA2' # for file naming
bounds = (64.,10.,242.,75.) # As: N, S, E, W
region_str = 'WPAC'

# Dates to process...
target_years = ['1980','1981','1982','1983','1984','1985','1986','1987','1988','1989','
1990','1991','1992','1993','1994','1995','1996','1997','1998','1999','2000','2001','200
2','2003','2004','2005','2006','2007','2008','2009','2010','2011','2012','2013','2014',
'2015']
targetmonth_str = region_str+'_1980-2015_ALLbasin_'
target_months = ['01','02','03','04','05','06','07','08','09','10','11','12']
target_hours = ['00','06','12','18']

# ------------------------- Setting Variables for Feature Testing -----------------
min_IVT = 250. # IVT anomaly threshold used to identify blobs
size_mask = 150. # Minimum blob size allowed for testing
min_aspect = 1.6 # Minimum length/width ratio for retained feature
min_orientation = 0.95 # Minimum orientation (taken as np.abs())
```


doi:10.6342/NTU201701272

```
min_length = 35. # Shortest feature length (in pixels)
min_meanintensity = 305. # Lowest mean IVT anomaly intensity within a feature
min_eccentricity = .87 # Minimum eccentricity of a retained feature
lat_cutoff = 3.0 # Will restrict features centered about the equator
lat_forceorient = 20.0 # Threshold for increased testing (mostly TC-focused)
min_forceorient = .5 # Orientation threshold for near-EQ features
# ------------------------------------------------------------------------------

# ------------------------- Setting Path Variables --------------------------------
#file of MERRA-2 IVT
nx=576
ny=361


# ------------------------- Function: days_in_month --------------------------------
def days_in_month(year,month):
    " Returns the number of days in the month provided "

    if month in ['01','03','05','07','08','10','12']:
        return 31
    elif month == '02':
        if operator.mod(int(year),4) == 0:
            return 29
        else:
            return 28
    elif month in ['04','06','09','11']:
        return 30

#------------------------- Function: distance_2points ---------------------------
def distance_2points(lon1,lat1,lon2,lat2):
    R = 6373.0
    lat1 = radians(lat1)
    lat2 = radians(lat2)
    lon1 = radians(lon1)
    lon2 = radians(lon2)
    dlon = lon2 - lon1
    dlat = lat2 - lat1
    a = sin(dlat /2)**2 + cos(lat1) * cos(lat2) *sin(dlon /2)**2
    c= 2*atan2(sqrt(a),sqrt(1-a))
    distance = abs(R*c)
    return distance

# ------------------------- Function: save_binary ---------------------------------
def save_binary(data_array,yr,mo,dy,data_label):
    " Saves array of data in NumPy binary format "
    outfilename = data_str+'_'+data_label+'_'+yr+mo+dy+'.npy'
    np.save(outpath+outfilename,data_array)

# ------------------------- Function: skeleton_length -----------------------------
def skeleton_length(array):
    " Skeletonizes the feature to estimate feature length in km "

    sk = skeletonize(array)
    ir,ic = np.nonzero(sk)
    numri = np.max(ir) - np.min(ir)
    numci = np.max(ic) - np.min(ic)
    if numri*1./2. > numci*5./8.:
        arr_flag = 'vert'
    else:
        arr_flag = 'horiz'

    newr,newc = [],[]
    if arr_flag == 'horiz':
```


doi:10.6342/NTU201701272

```
        duplicates = []
        for ind,col in enumerate(ic):
            if np.count_nonzero(np.where(ic == ic[ind])) > 1 and col not in duplicates:
                duplicates.append(col)
                newc.append(ic[ind])
                newr.append(np.min(ir[np.where(ic == ic[ind])]))
            elif col in duplicates:
                continue
            else:
                newr.append(ir[ind])
                newc.append(ic[ind])
        snewr, snewc = (list(el) for el in zip(*sorted(zip(newr, newc))))
        z = np.polyfit(snewc,snewr,3)
        p = np.poly1d(z)
        x = np.arange(np.min(snewc),np.max(snewc)+1,1)
        y = p(x)
        y = np.where(y >= bounds[3], bounds[3]-0.1, y)

    if arr_flag == 'vert':
        duplicates = []
        for ind,row in enumerate(ir):
            if np.count_nonzero(np.where(ir == ir[ind])) > 1 and row not in duplicates:
                duplicates.append(row)
                newr.append(ir[ind])
                newc.append(np.min(ic[np.where(ir == ir[ind])]))
            elif row in duplicates:
                continue
            else:
                newr.append(ir[ind])
                newc.append(ic[ind])
        snewr, snewc = (list(el) for el in zip(*sorted(zip(newr, newc))))
        z = np.polyfit(snewr,snewc,3)
        p = np.poly1d(z)
        y = np.arange(np.min(snewr),np.max(snewr)+1,1)
        y = np.where(y >= bounds[3], bounds[3]-0.1, y)
        x = p(y)

    y_vals = np.copy(y)
    y_pixel_km = (1./2.)*(111.2) # Approx. pixel extent in km
    piecewise_length = []

    for i in xrange(0,len(x)-1,1):
        # Visiting Pythagoras to estimate length of skeleton in km
        y_vals[i]=int(round(y_vals[i]))
        if y_vals[i] < 108. :
            #print 'y_vals=', y_vals[i]
            x_pixel_km = (5./8.)*(np.pi/180.0)*6378.137*abs(np.cos((np.pi/180.0)*sub_la
ts[int(y_vals[i])]))
            len_km = np.sqrt((abs(y_vals[i+1]-y_vals[i])*x_pixel_km)**2+(abs(x[i+1]-x[i
])*y_pixel_km)**2)
            piecewise_length.append(len_km)
        else:
            print 'wrong size',arr_flag

    return x,y,int(np.sum(piecewise_length))

# ------------------------ Function: read_data_anoIVT -------------------------------
def read_data_anoIVT(nx,ny,tstp):
    pathying='/home/ying/Analysis/Removal_first_two_harmonics/'
    filename='IVT.6HR.ANOS1.GDAT'
    # Reference code of calculating anomalous IVT field: June-Yi Lee's website
    # http://iprc.soest.hawaii.edu/users/jylee/bsiso/data.htm
    filenameying=pathying+filename
```


doi:10.6342/NTU201701272

```
    f = open(filenameying,'rb')
    f.seek(4*tstp*nx*ny)
    field = np.fromfile(f,dtype='float32',count=nx*ny)
    field = np.reshape(field,(ny,nx))
    # Transforming the array's grid
    data_array = np.empty([361,576])
    data_array[:,0:240] = field[:,336:577]
    data_array[:,240:577] = field[:,0:336]
    return data_array

# ------------------------ Function: read_data_totalIVT ------------------------------
-
def read_data_totalIVT(yr,mo,date_str,nx,ny,tstp):
    pathying='/home/ying/DATA/MERRA2/IVT_DATA_interp/'
    filename='IVT_'+date_str+'.bin'
    filenameying=pathying+yr+'/'+mo+'/'+filename
    f = open(filenameying,'rb')
    f.seek(4*tstp*nx*ny)
    field = np.fromfile(f,dtype='float32',count=nx*ny)
    field = np.reshape(field,(ny,nx))
    data_array = np.empty([361,576])
    data_array[:,0:240] = field[:,336:577]
    data_array[:,240:577] = field[:,0:336]
    return data_array

# ------------------------ Begin Main Program -----------------------------------
starttime = time.time() # Setting variable to calculate execution time

# Establishing grid variables
lats = np.arange(-90, 90.5, 0.5)
lons = np.arange(30, 390, 5./8)
ur_lat_ind,ur_lat = min(enumerate(lats), key=lambda i: abs(i[1]-bounds[0]))
ur_lon_ind,ur_lon = min(enumerate(lons), key=lambda i: abs(i[1]-bounds[2]))
ll_lat_ind,ll_lat = min(enumerate(lats), key=lambda i: abs(i[1]-bounds[1]))
ll_lon_ind,ll_lon = min(enumerate(lons), key=lambda i: abs(i[1]-bounds[3]))
sub_lats = lats[ll_lat_ind:ur_lat_ind]
sub_lons = lons[ll_lon_ind:ur_lon_ind]
nrows = len(sub_lats)
ncols = len(sub_lons)

if save_csv:
    # Preparing CSV file in which to save AR characteristics
    csvfname = 'AR_'+targetmonth_str+'ano'+str(int(min_IVT))+'_features_'+region_str+'_
'+str(datetime.date.today().toordinal())+'.csv'
    fullcsvfile = open(csvfname, 'wb')
    cw_full = csv.writer(fullcsvfile, delimiter=',')
    header = ['yr','mo','dy','hr','id','com_lat','com_lon','n_ext','s_ext','e_ext',\
              'w_ext','extent_rat','len_km','len_epix','width_epix','orient_deg',\
              'aspect_elw','area_pix','max_intensity','mean_intensity','total_ivta',\
              'qc_flag','TC_AR_distance','medianIVTa']
    cw_full.writerow(header)

# Loading array with TC date lat lon (i.e., 1980032118 101 1308)
#                                    (    = yyyymmddhh 10.1N 130.8E)
TC_da=np.genfromtxt('total1980-2015-Asia-TC.txt',delimiter=' ')

# Initializing counters
asplen_cnt = 0
orint_cnt = 0
fila_cnt = 0
tcish_cnt = 0
tchole_cnt = 0
tropics_cnt = 0
```


doi:10.6342/NTU201701272

```
solid_cnt = 0
TCinside_cnt = 0
mphole_cnt = 0
mp1a_cnt = 0
mp1b_cnt = 0
mp1c_cnt = 0
mpdeg_cnt = 0
mp4_cnt = 0
blob_cnt = 0
all_retained_cnt = 0

for yr in target_years:
    if operator.mod(int(yr),4) == 0:
        is_leap_year = True
    else:
        is_leap_year = False

    for mo in target_months:
        numdays = days_in_month(yr, mo)
        print 'Working on:', yr, mo
        outpath = './output/ano'+str(int(min_IVT))+'.modified2.'+region_str+'_TC/'+str(
yr)+'/'+str(mo)+'/'

        for dy in xrange(1, numdays + 1, 1):
            d_str = str(dy).rjust(2,'0')
            date_str = yr+mo+d_str
            day_index = (datetime.datetime(int(yr),int(mo),dy) - datetime.datetime(1980
,1,1)).days

            if operator.mod(day_index,1461) > 59:
                day_index = day_index - (np.float((int(yr)-1980)-operator.mod((int(yr)-
1980),4))/4+1.0)

            for hr_ind,hr in enumerate(['00','06','12','18']):
                if hr in target_hours: # Allows for the processing of subset of 6-hly p
eriods
                    dtg_str = date_str+hr
                    dtg_ind = (day_index*4)+hr_ind

                    #read ano ivt
                    ivt_anom = read_data_anoIVT(nx,ny,dtg_ind)\
                                            [ll_lat_ind:ur_lat_ind,ll_lon_ind:ur_lon_in
d]
                    nan_threshold = np.where(ivt_anom>=1e14, np.nan, 1)
                    ivt_anom = ivt_anom*nan_threshold

                    #read total ivt
                    #ivt_total = read_data_totalIVT(yr,mo,date_str,nx,ny,hr_ind)\
                    #           [ll_lat_ind:ur_lat_ind,ll_lon_ind:ur_lon_ind]
                    #nan_threshold_ivt = np.where(ivt_total>=1e14, np.nan, 1)

                    #ivt_total = ivt_total*nan_threshold_ivt

                    # get TC centers
                    TC_threshold = np.where(TC_da[:,0]==int(dtg_str),1,0)
                    TC_q=np.where(TC_threshold)
                    grid_TC_lats = []
                    grid_TC_lons = []
                    lats_TC = np.arange(ll_lat, ur_lat+0.5, 0.5)
                    lons_TC = np.arange(ll_lon, ur_lon, 5./8)
                    for tc_ind, TC_lat in enumerate(TC_da[TC_q][:,1]):
                        TC_lon = TC_da[TC_q][tc_ind,2]
                        TC_lon1 = TC_lon/10.
```


doi:10.6342/NTU201701272

```
                        TC_lat1 = TC_lat/10.
                        g_TC_lats = min(enumerate(lats_TC), key=lambda i: abs(i[1]-TC_l
at1))[0]
                        grid_TC_lats = np.append(grid_TC_lats[:], g_TC_lats)
                        g_TC_lons = min(enumerate(lons_TC), key=lambda i: abs(i[1]-TC_l
on1))[0]
                        grid_TC_lons = np.append(grid_TC_lons[:], g_TC_lons)

                    # Removing all IVT values less than defined "min_IVT"
                    threshold_array = np.where(ivt_anom > min_IVT, 1, 0)
                    label_array, num_labels = ndimage.measurements.label(threshold_arra
y)

                    # Removing small blobs (aka features of interest) from remaining IV
T anomaly field
                    sizes = ndimage.sum(threshold_array, label_array, range(num_labels
+ 1))
                    mask_size = sizes < size_mask # Applying a defined minimum "size_ma
sk"
                    remove_blob = mask_size[label_array]
                    label_array[remove_blob] = 0
                    labels = np.unique(label_array) # Relabeling the blobs after small
ones removed
                    label_array = np.searchsorted(labels, label_array)
                    # Counting the total number of blobs interrogated (after min IVT an
d size applied)
                    blob_cnt += np.count_nonzero(labels)

                    # Using skimage to calculate blob characteristics
                    blob_props = regionprops(label_array, intensity_image=ivt_anom)

                    retained_cnt = 0 # Will use to renumber retained blobs
                    # Initializing lists of CoM locations and blob labels for plotting
                    clats,clons,blabels = [],[],[]

                    # Testing each blob to determine if it may be an AR
                    for i,blob in enumerate(blob_props):
                        logic_flag = 'na'
                        qc_flag = 'na'
                        true_orient = 'na'
                        orientation = blob.orientation
                        length = blob.major_axis_length
                        width = blob.minor_axis_length
                        area = blob.area
                        if width > 0.:
                            aspect = length/np.float(width)
                        else:
                            aspect = 0
                        meanint = blob.mean_intensity
                        y0, x0 = blob.weighted_centroid
                        y0=int(round(y0))
                        x0=int(round(x0))

                        if (aspect < min_aspect or length < min_length):
                            # Clearing the blobs that do not meet the aspect ratio or m
in length
                            label_array[label_array == blob.label] = 0
                            logic_flag = 'asp-len'
                            asplen_cnt += 1

                        elif (abs(sub_lats[y0]) < lat_forceorient and \
                              abs(orientation) < min_orientation) or \
                             (abs(sub_lats[y0]) < lat_forceorient and \
```


doi:10.6342/NTU201701272

```
                                abs(orientation) < (1.0-min_orientation)) or \
                               meanint < min_meanintensity:
                            # Clearing the blobs that do not meet the orientation or me
an intensity
                            label_array[label_array == blob.label] = 0
                            logic_flag = 'or-int'
                            orint_cnt += 1

                        elif (abs(sub_lats[y0]) < lat_forceorient and \
                              blob.eccentricity < min_eccentricity) or \
                              (abs(sub_lats[y0]) >= lat_forceorient and \
                              blob.eccentricity < min_eccentricity - 0.1):
                            # Attempting to filter out blobs that lack "filament-like"
character
                            label_array[label_array == blob.label] = 0
                            logic_flag = 'filament'
                            fila_cnt += 1

                        elif abs(sub_lats[y0]) < (lat_forceorient + 0.) and \
                             blob.eccentricity > min_eccentricity and \
                             blob.mean_intensity > 375 and blob.extent > .50:
                            # Attempting to remove solid, round, intense blobs
                            # that may be TCs or similar storms
                            label_array[label_array == blob.label] = 0
                            logic_flag = 'tc-like'
                            tcish_cnt += 1

                        elif abs(sub_lats[y0]) < lat_forceorient and \
                             (int(blob.area) - blob.filled_area) <= -5:
                            # Removing blobs with sizeable holes (mostly TCs "eyes")
                            label_array[label_array == blob.label] = 0
                            logic_flag = 'tc-hole'
                            tchole_cnt += 1

                        elif abs(sub_lats[y0]) <= lat_cutoff or \
                             (abs(sub_lats[y0]) <= lat_forceorient and \
                             abs(orientation) <= min_forceorient):
                            # Further scrutinizing blobs in the tropics to remove
                            # west-east features along ITCZ
                            label_array[label_array == blob.label] = 0
                            logic_flag = 'tropics'
                            tropics_cnt += 1

                        elif aspect < 1.90 and blob.solidity > 0.90 and blob.extent > 0
.40:
                            # Attempting to allow for curvature of AR, but removing
                            # "solid" eliptical blobs
                            label_array[label_array == blob.label] = 0
                            logic_flag = 'solid'
                            solid_cnt += 1
                        elif blob.extent > 0.40: # check_TC   # ying 2017May
                            for tc_ind, TC_lon in enumerate(grid_TC_lons):
                                testTC = label_array[int(grid_TC_lats[tc_ind]),int(grid
_TC_lons[tc_ind])]
                                if (testTC == blob.label):
                                    label_array[label_array == blob.label] = 0
                                    logic_flag = 'TC_inside'
                                    TCinside_cnt += 1

                        else:
                            # Performing additional tests on a blob that would otherwis
e be retained
                            temp_mask = np.zeros([nrows,ncols])
```


doi:10.6342/NTU201701272

```
                            temp_mask[label_array == blob.label] = 1
                            peaks = peak_local_max(ivt_anom*temp_mask, min_distance=14,
 num_peaks=4)

                            if len(peaks) > 1:
                                blob_image_array = ivt_anom * (label_array == blob.labe
l)
                                bigblob_mask = np.ones([nrows,ncols]) * -1
                                bigblob_mask[label_array == blob.label] = 0

                                for peak_ind, peak_coords in enumerate(peaks):
                                    bigblob_mask[peak_coords[0],peak_coords[1]] = peak_
ind+1

                                segmented_blob = random_walker(blob_image_array, bigblo
b_mask, beta=75)

                                for sub_label in np.unique(segmented_blob):
                                    if sub_label == -1:
                                        continue
                                        # -1 is the background; negative values are ign
ored
                                    else:
                                        segmented_blob_mask = np.zeros([nrows,ncols],dt
ype='int')
                                        segmented_blob_mask[segmented_blob == sub_label
] = sub_label
                                        segment_props = regionprops(segmented_blob_mask
,\
                                                                    intensity_image=ivt
_anom)
                                        sy0, sx0 = segment_props[0].weighted_centroid
                                        sy0=int(round(sy0))
                                        sx0=int(round(sx0))

                                        if abs(sub_lats[sy0]) < (lat_forceorient + 7.5)
 and \
                                           int(segment_props[0].area) != segment_props[
0].filled_area:
                                            # Removing segments with noticeable holes (
i.e., mostly TCs)
                                            segmented_blob_mask[segmented_blob == sub_l
abel] = 0
                                            label_array[segmented_blob == sub_label] =
0
                                            qc_flag = 'segment'
                                            logic_flag = 'multi-peak-hole'
                                            mphole_cnt += 1

                                        elif segment_props[0].eccentricity <= min_eccen
tricity - 0.1:
                                            # Removing segments that don't seem filamen
t-like
                                            segmented_blob_mask[segmented_blob == sub_l
abel] = 0
                                            label_array[segmented_blob == sub_label] =
0
                                            qc_flag = 'segment'
                                            logic_flag = 'multi-peak-1a'
                                            mpla_cnt += 1

                                        elif segment_props[0].mean_intensity < min_mean
intensity:
```


doi:10.6342/NTU201701272

```
                                        # Removing segments that appears as weak co
nnectors
                                        # between two IVT peaks
                                        segmented_blob_mask[segmented_blob == sub_l
abel] = 0
                                        label_array[segmented_blob == sub_label] =
0
                                        qc_flag = 'segment'
                                        logic_flag = 'multi-peak-1b'
                                        mp1b_cnt += 1

                                    elif abs(sub_lats[sy0]) <= lat_cutoff or \
                                         ((abs(sub_lats[sy0]) <= lat_forceorient -
7.5) and \
                                          abs(segment_props[0].orientation) <= min_f
orceorient):
                                        # Removing segments with a west-east orient
ation
                                        # along the ITCZ
                                        segmented_blob_mask[segmented_blob == sub_l
abel] = 0
                                        label_array[segmented_blob == sub_label] =
0
                                        qc_flag = 'segment'
                                        logic_flag = 'multi-peak-1c'
                                        mp1c_cnt += 1
                                    elif (sub_lats[sy0] > 0. \
                                         and sub_lats[sy0] < lat_forceorient \
                                         and abs(-1*np.rad2deg(segment_props[0].ori
entation))<10)\
                                          or (sub_lats[sy0] < 0. \
                                              and sub_lats[sy0] > -1*lat_forceorient
 \
                                              and abs(-1*np.rad2deg(segment_props[0]
.orientation))\
                                              < 10):
                                        # Scrutinizing the orientation of
                                        # tropical/subtropical segments
                                        segmented_blob_mask[segmented_blob == sub_l
abel] = 0
                                        label_array[segmented_blob == sub_label] =
0
                                        qc_flag = 'segment'
                                        logic_flag = 'multi-peak-deg'
                                        mpdeg_cnt += 1
                                    else:
                                        segmented_blob_mask[segmented_blob == sub_l
abel] = 1

                                # Recalculating CoM based on remaining blob segments
                                label_array[label_array*segmented_blob_mask == blob.lab
el] = blob.label
                                temp_props = regionprops((label_array == blob.label).as
type(int), \
                                                         intensity_image=ivt_anom)
                                if len(temp_props) > 0:
                                    y0, x0 = temp_props[0].weighted_centroid
                                    y0=int(round(y0))
                                    x0=int(round(x0))
                                else:
                                    continue

                            # Testing the portion of the blob greater than its own aver
```


doi:10.6342/NTU201701272

```
age intensity
                            interior_array = np.where(ivt_anom*temp_mask > meanint, 1,
0)
                            interior_mass = regionprops(interior_array, intensity_image
=ivt_anom)
                            if len(interior_mass) > 0. and \
                               interior_mass[0].eccentricity < min_eccentricity - 0.075
:
                                # Finally, removing blobs the interior of which
                                # aren't sufficiently filament-like
                                label_array[label_array == blob.label] = 0
                                qc_flag = 'segment'
                                logic_flag = 'multi-peak-4'
                                mp4_cnt += 1
                            else:
                                retained_cnt += 1
                                all_retained_cnt += 1
                                clats.append(sub_lats[y0])
                                clons.append(sub_lons[x0])
                                label_array[label_array == blob.label] = retained_cnt #
 Renumbering
                                blabels.append(retained_cnt)
                                # (Re)Calculating characteristics of retained features
                                if qc_flag == 'segment':
                                    orient_deg = int(-1*np.rad2deg(temp_props[0].orient
ation))
                                    if blob.bbox[2] >= nrows:
                                        n_ext = bounds[0]
                                    else:
                                        n_ext = sub_lats[temp_props[0].bbox[2]]
                                    if blob.bbox[3] >= ncols:
                                        e_ext = bounds[2]
                                    else:
                                        e_ext = np.around(sub_lons[temp_props[0].bbox[3
]], decimals=1)
                                    s_ext = sub_lats[temp_props[0].bbox[0]]
                                    w_ext = np.around(sub_lons[temp_props[0].bbox[1]],
decimals=1)
                                    length = temp_props[0].major_axis_length
                                    width = temp_props[0].minor_axis_length
                                    if width > 0.:
                                        aspect = length/width
                                    else:
                                        aspect = 0
                                else:
                                    orient_deg = int(-1*np.rad2deg(orientation))
                                    # -1 since the array is actually flipped
                                    if blob.bbox[2] >= nrows:
                                        n_ext = bounds[0]
                                    else:
                                        n_ext = sub_lats[blob.bbox[2]]
                                    if blob.bbox[3] >= ncols:
                                        e_ext = bounds[2]
                                    else:
                                        e_ext = np.around(sub_lons[blob.bbox[3]], decim
als=1)
                                    s_ext = sub_lats[blob.bbox[0]]
                                    w_ext = np.around(sub_lons[blob.bbox[1]], decimals=
1)

                                x,y,slength = skeleton_length(np.where(\
                                    label_array == retained_cnt, 1, 0))
                                total_IVTa = int(np.sum(ivt_anom * np.where(\
```


doi:10.6342/NTU201701272

```
                                    label_array == retained_cnt, 1, 0)))
                                median_IVT = np.nanpercentile(ivt_anom * np.where(\
                                    label_array == retained_cnt, 1, np.nan),50)

                                # ying TC, 2017May
                                TC_threshold = np.where(TC_da[:,0]==int(dtg_str),1,0)
                                TC_q=np.where(TC_threshold)
                                TC_AR_distance = 0.0
                                TC_AR_distance_re = 1e20
                                TC_lon1 = []
                                TC_lat1 = []
                                for tc_ind, TC_lat in enumerate(TC_da[TC_q][:,1]):
                                    TC_lon = TC_da[TC_q][tc_ind,2]
                                    TC_lon1 = TC_lon/10.
                                    TC_lat1 = TC_lat/10.
                                    TC_AR_distance = distance_2points(\
                                        sub_lons[x0],sub_lats[y0],TC_lon1,TC_lat1)
                                    #print TC_AR_distance
                                    if (TC_AR_distance < TC_AR_distance_re):
                                        TC_AR_distance_re = TC_AR_distance


                                if qc_flag == 'segment':
                                    datarow_all = [yr,mo,d_str,hr,retained_cnt,sub_lats
[y0],\
                                                   sub_lons[x0],n_ext,s_ext,e_ext,w_ext
,\
                                                   np.around(temp_props[0].extent,decim
als=2),\
                                                   slength,np.around(length,decimals=2)
,\
                                                   np.around(width,decimals=2),true_ori
ent,\
                                                   np.around(aspect,decimals=1),\
                                                   int(temp_props[0].area),\
                                                   np.around(temp_props[0].max_intensit
y,decimals=2),\
                                                   np.around(temp_props[0].mean_intensi
ty,decimals=2),\
                                                   total_IVTa,qc_flag,TC_AR_distance_re
,median_IVT]
                                else:
                                    datarow_all = [yr,mo,d_str,hr,retained_cnt,sub_lats
[y0],\
                                                   sub_lons[x0],n_ext,s_ext,e_ext,w_ext
,\
                                                   np.around(blob.extent,decimals=2),sl
ength,\
                                                   np.around(length,decimals=2),\
                                                   np.around(width,decimals=2),true_ori
ent,\
                                                   np.around(aspect,decimals=1),int(are
a),\
                                                   np.around(blob.max_intensity,decimal
s=2),\
                                                   np.around(blob.mean_intensity,decima
ls=2),\
                                                   total_IVTa,qc_flag,TC_AR_distance_re
,median_IVT]

                                if save_csv:
                                    cw_full.writerow(datarow_all)
```


doi:10.6342/NTU201701272

```
if save_csv:
    fullcsvfile.close()
# ------------------------ End of Program ----------------------------------------
print '\nNumber of Total Features:', blob_cnt
print 'Number Retained:', all_retained_cnt, 'or', 100.*all_retained_cnt/blob_cnt, '%'
print 'Number Cut By: (* will not sum to total cut due to segmented logic)'
print ' asplen_cnt\t', asplen_cnt
print ' orint_cnt\t', orint_cnt
print ' fila_cnt\t', fila_cnt
print ' tcish_cnt\t', tcish_cnt
print ' tchole_cnt\t', tchole_cnt
print ' tropics_cnt\t', tropics_cnt
print ' solid_cnt\t', solid_cnt
print ' TCinside_cnt\t', TCinside_cnt
print ' mphole_cnt\t', mphole_cnt
print ' mp1a_cnt\t', mp1a_cnt
print ' mp1b_cnt\t', mp1b_cnt
print ' mp1c_cnt\t', mp1c_cnt
print ' mpdeg_cnt\t', mpdeg_cnt
print ' mp4_cnt\t', mp4_cnt

endtime = time.time()
elapsedtime_min = (endtime - starttime) / 60

print '\nEnd of Program'
print 'Total Execution Time =', str(elapsedtime_min), 'mins'
```

Fig. A The code of the modified AR detection algorithm.

doi:10.6342/NTU201701272

Appendix B. AR Without Further TC Criteria

As shown in the Method in Chapter 2.2.2, step [9] was added additionally to remove the TC features misidentified by the algorithm. If this criterion is removed, the results are more similar to those in Mundhenk et al. (2016). There are still some mild differences probably because we asked for longer features (roughly over 2000 km) than Mundhenk et al. (2016) did.

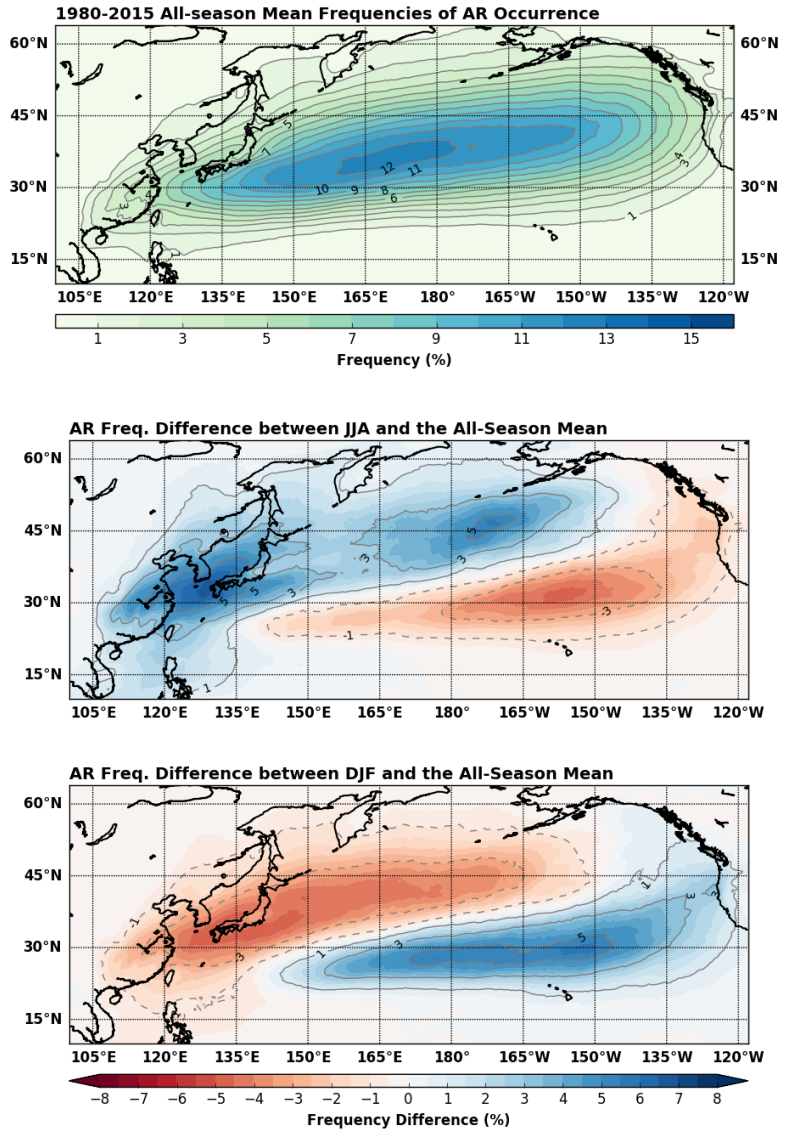

Fig. B Same as Fig. 3.1 but for removing the criteria of excluding the round TC-included features.

doi:10.6342/NTU201701272

Appendix C. Details of the Boxplots

Details of the boxplots in Fig. 3.9 are listed as following: each of the box represents the interquartile range (IQR) from 25 percentile (Q1) to 75 percentile (Q3) and includes the middle 50% of the data points. The upper (lower) whisker are 1.5 times the IQR above (below) the Q3 (Q1). The line in the box shows the median and the diamond shows the mean of the data points. The notches are set to check whether the medians of the two data points are difference: if the two notches don't overlap, there is 'strong evidence' – at a 95% confidence level – that the medians of the two data points differ (Chambers 1983). All these four boxplots in Fig. 3.9 have long tail of outliers above the top whisker, which means that the distribution of these data points are not normal distribution but logarithmic distribution.

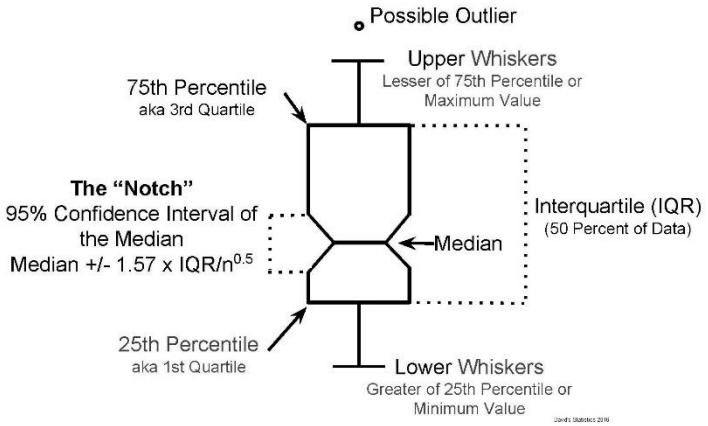

Fig. C The schematic of notched box plot. Adapted from David's Statistics website (https://sites.google.com/site/davidsstatistics/home/notched-box-plots).

doi:10.6342/NTU201701272

Appendix D. Prefigurance and Postagreement Based on anomalous IVT fields

In this paper, we apply total IVT fields to the AR detection algorithm with a criterion of IVT ≥ 450 kg m^{-1} s^{-1} to discuss the relation between ARs and the heavy rainfall in Taiwan. This criterion is somewhat looser than the 250 kg m^{-1} s^{-1} on the anomalous IVT fields. For example, as shown in Fig. 2.4, one standard deviation of the summer total IVT in the low latitude WNP is about 50 kg m^{-1} s^{-1}, and the anomalous IVT with the 250 kg m^{-1} s^{-1} threshold is equal to 5 times the standard deviation. The mean total IVT in summer in this region is about 400 kg m^{-1} s^{-1}. If 5 standard deviations are added to the mean, the threshold is equal to 650 kg m^{-1} s^{-1}. That is, in the low latitude in WNP, anomalous IVT with the 250 kg m^{-1} s^{-1} threshold is roughly equal to 650 kg m^{-1} s^{-1} threshold on the total IVT fields in summer. However, the mean total IVT and the standard deviation changes with the locations, so the estimations above might not apply to the whole low latitude WNP.

The results of the number, the prefigurance and the postagreement with the anomalous IVT fields applied to the AR detection algorithm in the warm season (MJJA) are shown in Fig. D.

doi:10.6342/NTU201701272

(a)

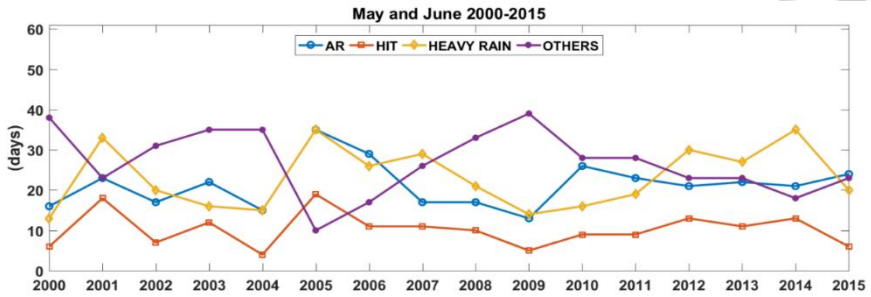

(b)

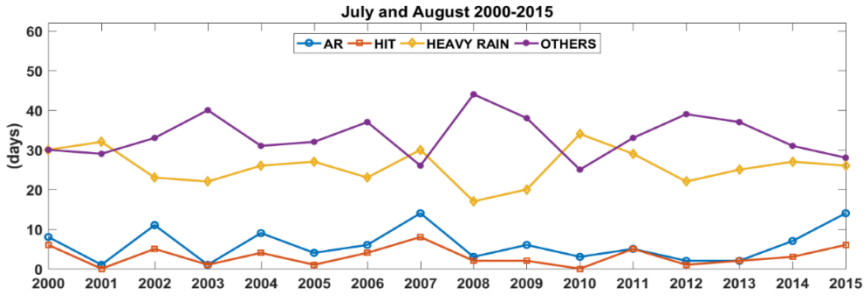

(c)

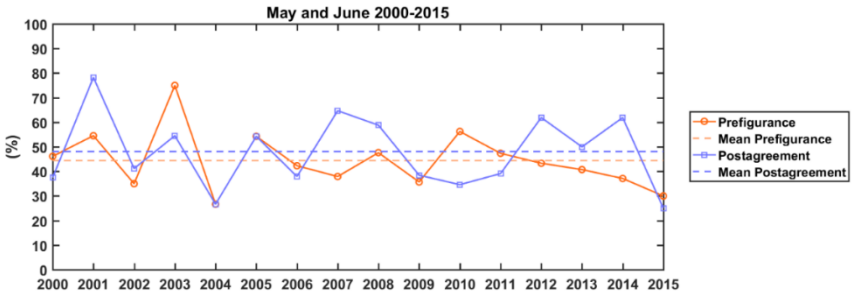

(d)

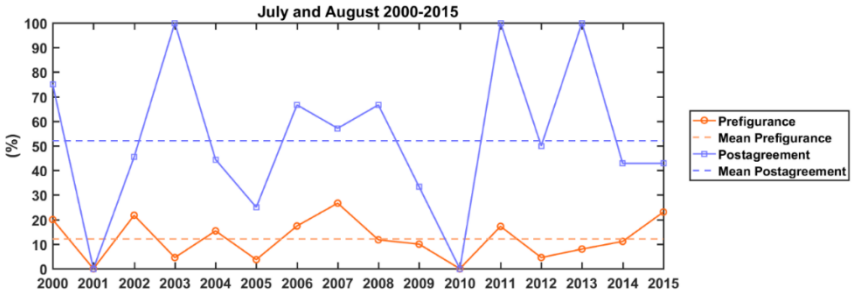

Fig. D The number of days that Taiwan are influenced by ARs in (a) May and June or in (b) July and August during 2000-2015. The definition of the four groups can be find in Chapter 2.2.3. The prefigurance and the postagreement in (c) May and June or (d) July and August are denoted in solid line. The mean values of them are in dash line. The fields applied to the AR detection algorithm are the anomalous IVT fields.

doi:10.6342/NTU201701272

Appendix E. Sensitivity Test of the Prefigurance and the Postagreement on the Smaller Domain of Taiwan

The date influenced by "AR" is defined as the date when the box of Taiwan ($[118^0\mathrm{E}, 124^o\mathrm{E}] \times [20^o\mathrm{N}, 27^o\mathrm{N}]$) is partially covered by the contour of any detected AR in Chapter 2.2.2. If the box of Taiwan is one degree smaller at each sides ($[119^0\mathrm{E}, 123^o\mathrm{E}] \times [21^o\mathrm{N}, 26^o\mathrm{N}]$), the prefigurance and the postagreement are slightly smaller but the patterns are still similar (Fig. E).

doi:10.6342/NTU201701272

(a)

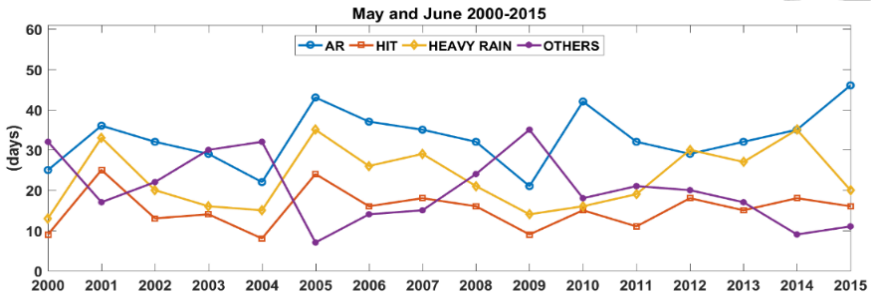

(b)

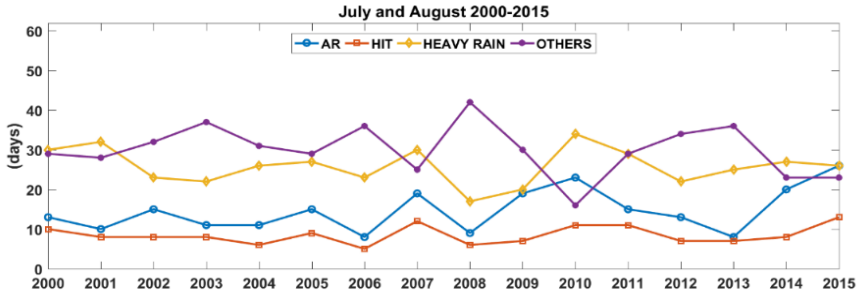

(c)

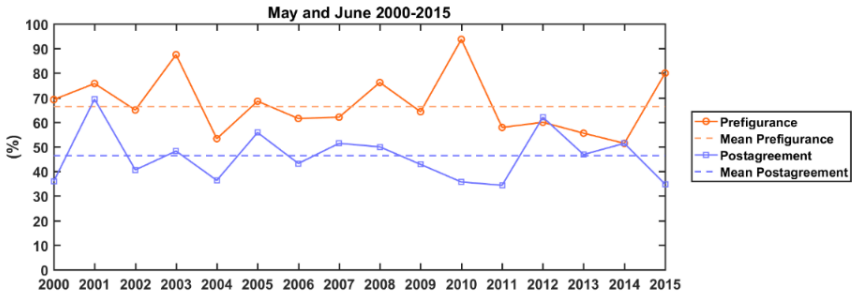

(d)

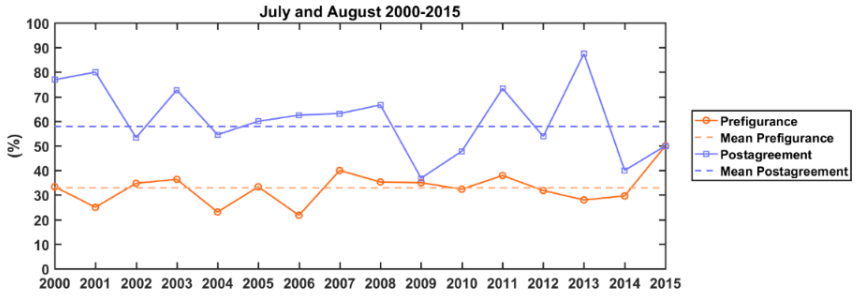

Fig. E The days that Taiwan are influenced by ARs in (a) May and June or in (b) July and August during 2000-2015. The definition of the four groups is defined in Chapter 2.2.3. The prefigurance and the postagreement in (c) May and June or (d) July and August during 2000-2015 are denoted in solid line. The mean values of them are in dash line. The fields applied to the AR detection algorithm are the total IVT fields.

doi:10.6342/NTU201701272

Appendix F. AR evolution in the Mei-Yu Season and in the Typhoon Season of Taiwan

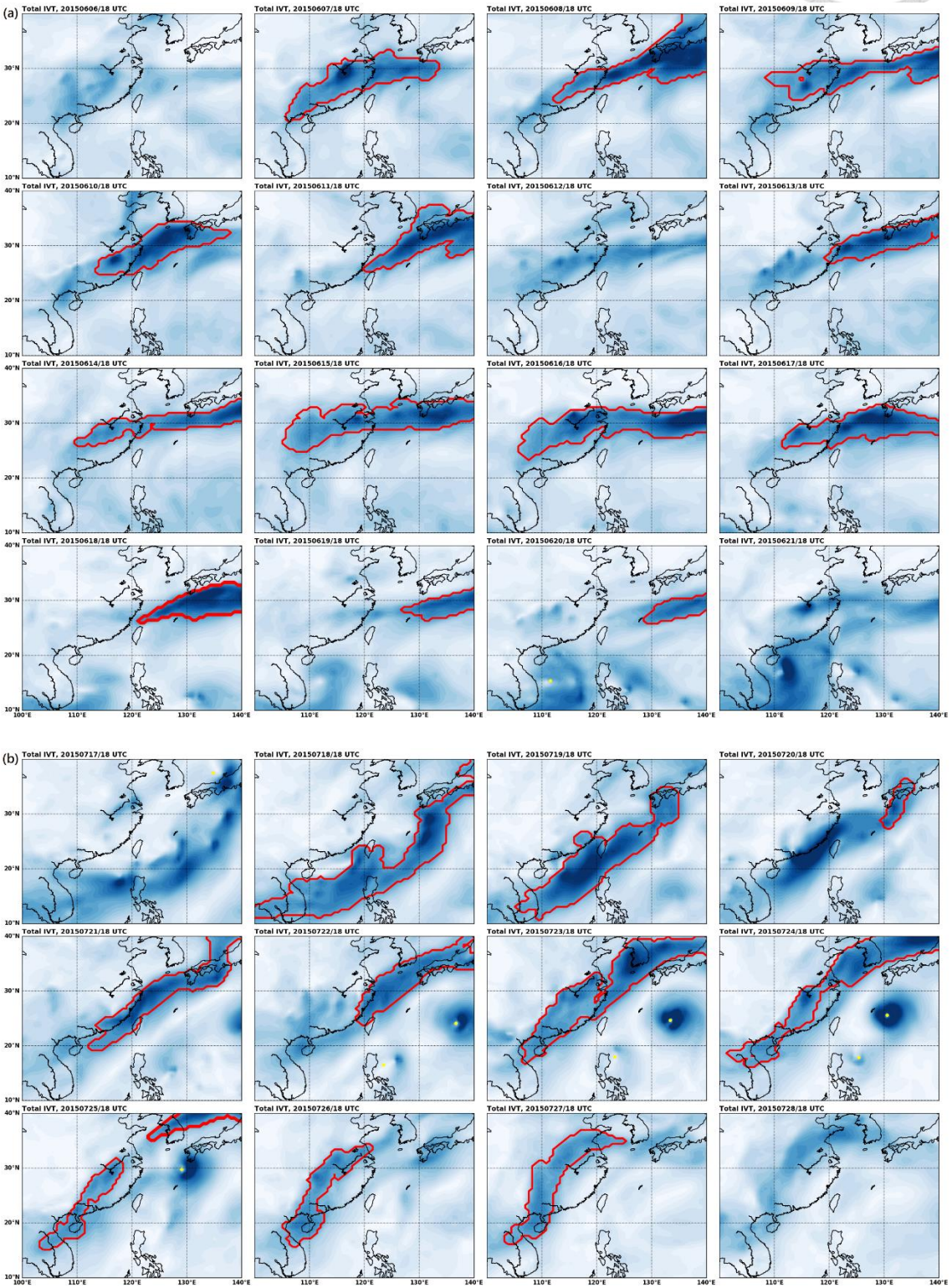

doi:10.6342/NTU201701272

Fig. F The AR evolution (a) in the “Mei-Yu Season” during 06-21 June 2015 and (b) in the “Typhoon Season” during 17-28 July 2015. The integrated water vapor transport ($kg\ m^{-1}\ s^{-1}$) is shaded and the features detected as ARs (using the algorithm with anomalous IVT fields) are contoured in red.

doi:10.6342/NTU201701272